CHARACTERIZATION OF THE MICRO-WELDING PROCESS FOR COMMON GAS TURBINE ENGINE ALLOYS

BY

JONATHAN DUROCHER

A Thesis submitted to
the Faculty of Graduate Studies
in partial fulfilment of the requirements for the Degree of

MASTER OF SCIENCE

Department of Mechanical and Manufacturing Engineering
University of Manitoba
Winnipeg, Manitoba

THE UNIVERSITY OF MANITOBA

FACULTY OF GRADUATE STUDIES

*****

COPYRIGHT PERMISSION

"Characterization of the Micro-Welding Process for Common Gas Turbine Engine Alloys"

BY

Jonathan Durocher

A Thesis/Practicum submitted to the Faculty of Graduate Studies of The University of Manitoba in partial fulfillment of the requirement of the degree

Of

MASTER OF SCIENCE

ACKNOWLEDGEMENTS

I wish to take the opportunity to thank Dr. Norman Richards for his valuable advice and guidance over the course of this project. I would also like to thank Dr. John Kelley of Advanced Surfaces And Processes for his expert advice on micro-weld processing and supplying weld deposits to support this research project.

Additional thanks are due to John Van Dorp and Mike Boskwick in the Department of Mechanical and Manufacturing Engineering at the University of Manitoba for their continued assistance.

I extend great gratitude to my family and friends for their support and encouragement.

ABSTRACT

Micro-welding is a low heat input process whereby a metal or cermet is deposited by the generation of a low power arc between a consumable electrode and a substrate. Micro-weld deposits are metallurgically bonded to the substrates and a localized re-alloying process takes place. The low heat input of this process offers unique advantages over more common welding processes such as gas tungsten arc, plasma arc, laser and electron beam welding. Since the late 1980's, micro-welding has seen increased use for the application of coatings to gas turbine engine components. At present, the repair of turbine blades and vanes commonly involves gas tungsten arc welding. Modern turbine blades and vanes alloys are made from gamma prime $Ni_3(Al, Ti)$ strengthened nickel based superalloys and are susceptible to heat affected zone cracking during the weld repair process. The low heat input characteristic of micro-welding has been utilized to apply various filler alloys to a cast Inconel 738 substrate. Micro-weld fillers were selected based on their range of aluminum and titanium content.

This thesis reports on a two-level three-factor design of experiments conducted in order to develop a mathematical model of the micro-welding process. The effects of process parameters on the deposition rate, porosity content, crack density and coating hardness were investigated using statistical analysis software. Oxidation tests were conducted to study the effect of aluminum + chromium concentration on the oxidation resistance of micro-welded nickel based coatings. Parabolic oxidation rate constants were obtained and energy dispersive spectroscopy was used to provide semi-quantitative results on the composition of protective oxide scales and internal precipitates. A residual stress experiment was also conducted to determine the nature and provide an approximation of magnitude for residual stresses in micro-weld deposits.

Micro-welding has been found to be a suitable process for the application of high aluminum + titanium content filler alloys to Inconel 738. High deposition rates were obtained with high pulse power parameters but produced higher amounts of porosity and cracking. High quality deposits required low pulse powers which led to low deposition rates. The oxidation rates of micro-welded Inconel 738 and uncoated cast Inconel 738 were practically identical. Although there was no significant change in scale thickness or oxide penetration, the micro-welding process was shown to be a suitable method for applying coatings of high aluminum, chromium and titanium to protect a less resistant substrate. The internal stresses generated in micro-welded coating were tensile in nature and appear to be significant in magnitude.

Recommendations for future projects are presented in the conclusions.

TABLE OF CONTENTS

LIST OF FIGURES

LIST OF TABLES

1. INTRODUCTION

Since the successful application to aircraft jet propulsion in the 1940's, gas turbines have revolutionized the transportation world. Turbine engines have allowed aircraft to reach higher speeds, higher altitudes and fly further than what was possible with traditional reciprocating engines. Other applications in transportation include the propulsion of rotary wing aircraft and ships. Land based or otherwise referred to as industrial turbines, are currently used for electrical power generation and as booster pumps in the petroleum industry. With a continuous requirement for improved efficiency, turbine designs have evolved to increase their operating temperatures. The gas temperature in a modern gas turbine can reach upwards of 1650°C in the combustor section and 1500°C as it enters the first turbine stage. The interaction of high temperature gases with combustor and turbine components must be controlled by innovative means. For example, effusion cooling holes in combustor liners and turbine blades introduce cooler air to form a protective boundary layer between hot gases and component surfaces. Working in conjunction with air cooling films, advanced thermal barrier ceramic coatings are applied to turbine components to further reduce their exposure to high temperature gases.

In today's competitive markets, maintenance of turbines is an important economic consideration for operators. Original equipment manufacturers (OEM's) offer competitive pricing for their products provided that clients enter a long term maintenance contract with that OEM. Although the OEM's profits may be reduced on initial sale of turbines, their maintenance programs generate significant revenues over periods up to twenty years. In addition to OEM's, certified independent maintenance centers are also available for operators that are not bound to an OEM maintenance contract.

Based on a pre-determined schedule, turbines are sent to repair centers for inspection, repair and overhaul. Upon partial or complete tear-down of the engine, components are subject to non-destructive inspection and assessment of required work needed to return the engine to its engineering drawing and performance requirements. When possible, components will be repaired provided that the costs do not exceed 40 to 60% of the replacement value. Of the components requiring replacement and repair, turbine blades and nozzle guide vanes deserve the most attention due to their high cost and frequency of replacement relative to other turbine components. For a modern turbine, the complete replacement of a set of first stage turbine blades is in the range of $400K to $500K USD while a set of vanes is in the $250K to $350K USD range (2001 values).

Life limiting factors contributing to the degradation and eventual failure of blades and vanes are fuel, operating temperature, water ingestion and cycling. The resulting failure modes of components are rupture, creep, high cycle fatigue, oxidation, erosion, corrosion, wear and foreign object damage. Blades are considered to be critical components because in addition to being subjected to thermal and aerodynamic stresses, are subjected to rotational stresses. The combination of high stress and thermal loading drastically decreases their service life over that of vanes. The criticality of blades also imposes heavy restrictions on the extent of repairs that can be made. Repairs must be devised such that the original engineering drawing requirements are met. In general, repairs tend to have reduced properties as compared to the base material and are limited to the upper 10 to 20% portion of blades where they experience the least amount of loading. Today's welding processes fail to produce a repaired blade where the original properties have been fully restored. Therefore, where unacceptable damage is found outside the permitted repair area, blades must be replaced. This restriction

brings great potential to the development of innovative repair techniques, processes and use of materials to increase the fraction of blades that can be repaired.

Inconel 738 is a common nickel based superalloy found in gas turbine blades and vanes. Being precipitation hardened by the γ' phase $Ni_3(Al, Ti)$ and MC type carbides the alloy suffers from micro-cracking in the weld heat affected zone as a result of precipitation and grain boundary liquation during the weld cycle. This problems also affects other γ' alloys where the aluminum + titanium content is greater than 3 wt.%. To minimize cracking in blade alloys, a softer solid solution strengthened alloy such as Inconel 625 is commonly used as weld filler. The resulting repair is inferior to the parent material for wear, corrosion resistance, hardness, tensile strength and creep resistance.

Current repair processes include gas tungsten arc welding (GTAW), plasma transferred arc welding (PTAW), micro-plasma transferred arc welding, laser beam welding (LBW), diffusion brazing, wide gap diffusion brazing and transient liquid phase bonding. Of these processes, manual GTAW is by far the most common due to its relative low cost, simplicity and versatility. The disadvantages of using GTAW are that the process is relatively slow, and that solid solution strengthened alloy fillers are required when welding high strength γ' precipitation hardenable alloys. The use of high strength fillers leads to severe heat affected zone micro-cracking.

PTAW and micro-PTAW differ from GTAW in that they provide a concentrated high heat density with less heat input to the base metal. Micro-PTAW uses much smaller currents than PTAW and consequently results in further reduction of heat input to the base metal. The advantages are reduced penetration, less incipient melting, a smaller heat affected zone and

less distortion of the base metal. With the reduced heat input of micro-PTAW, successful repairs of high strength γ' alloys have been possible. The disadvantages of PTAW and micro-PTAW are that equipment costs range from 2 to 5 times more than GTAW and greater welder knowledge and skill are required.

Over the past ten years, laser beam welding (LBW) has seen increased use in the field of blade and vane repair. LBW has a significant advantage over electron beam welding (EBW) because the beam can be transmitted in air. This eliminates costly vacuum chambers and pumps required for EB processing. In LBW, heating is very localized with lower heat input providing narrow welds and heat affected zone similar to but with less penetration than EBW. The LBW process is usually automated and filler materials are applied as wire or powder form. The process is faster than GTAW and PTAW with less post-weld machining and re-working being required. Fillers can be solid solution or γ' strengthened alloys but the welds can suffer from heat affected zone cracking. Crack free LBW has been possible with a blown powder filler application. The main disadvantages are high set-up costs of up to $1M USD, high level operator training requirements, extensive and complex machine maintenance, safety and inefficient use of power. These factors account for the relatively slow introduction of the process for repair applications.

Brazing processes are not permitted on highly stressed components such as blades. Diffusion brazing is permitted for small crack repairs limited non-critical stationary components. The process relies heavily on cleaning and removal of oxides for proper wetting and flow of the braze alloy. Since melting point depression elements such as boron are present in the braze alloy, the use of brazing processes limits future repairs by welding since the braze alloy would breakdown in the weld pool. Wide gap brazing is a process used to re-build missing

sections of airfoils, crack repair and restoration of eroded wall thickness. As with diffusion brazing the presence of boron also limits future repairs by welding and reduces the oxidation resistance of the repair. Transient liquid phase bonding is also similar to brazing as it restores good properties to the repaired areas. The isothermal solidification process provides a homogenized bond free of elemental segregation. However, since boron is used as a melting point depressant, the process suffers from the same drawbacks as diffusion and wide gap brazing.

In light of the shortcomings of current processes, the future of repairs to high strength nickel based γ' turbine superalloys relies on the development of low heat input filler deposition processes. One such process seeing increased use in the aerospace industry is micro-welding. With micro-welding, a consumable electrode is held in contact and sparked with a conductive substrate using low pulse powers. Vaporized and molten electrode material is deposited on the substrate's surface and subjected to very high cooling rates. The resulting deposit is metallurgically bonded and re-alloyed with the substrate.

The process was accidentally discovered some 80 years ago when steel was observed to harden when sparked with a low heat input. The low heat input to the substrate caused extremely rapid cooling and re-solidification rates to occur for martensite to form on the steel's surface. Some of the first significant industrial applications of the process were in the former Soviet Union where it was used to apply wear resistant coatings to machine tools during the 1970's. The next apparent significant application of micro-welding was to apply low friction wear resistant coatings to nuclear reactor cooling tubes and core components. In these applications, chromium carbide based coatings were successfully qualified and used to prevent component wear and corrosion in severe operating conditions.

Micro-welding has seen increased use in gas turbine engine applications and Rolls Royce (UK) reportedly has some forty approved repairs involving micro-welded deposits. A drawback from GTAW, PTAW, micro-PTAW and LBW, is that micro-welding suffers from very low deposition rates. In general, high quality coatings require low power parameters which correspond to low deposition rates. Therefore, the low heat input and ability to apply a variety of materials makes micro-welding an ideal candidate for the repair of high strength γ' alloys used in gas turbine components.

2. SCOPE OF STUDY

In this study, the effect of micro-welding process parameters on the deposition rate, coating quality and substrate has been investigated. The alloys applied as consumable electrodes were selected based on their relative aluminum + titanium concentrations. Analyses were carried on the micro-weld result to assess whether micro-welding is susceptible to heat affected zone cracking with common high strength γ' gas turbine alloys to a cast Inconel 738 substrate. Using a design of experiments, the establishment of process models for the effect of pulse parameter selection on deposition rate, void content and crack density has been investigated.

With oxidation being a significant life limiting factor for gas turbine blades and vanes, elevated oxidation tests were conducted on micro-weld coated and bare γ' alloys. Turbine alloys generally contain sufficient concentrations of aluminium and chromium to ensure the formation of protective scales. Therefore, the micro-welded coating alloys were selected based on their relative aluminium and chromium concentrations.

Common welding processes induce significant internal stresses in the base material and can be detrimental to component life. Components welded with high heat input processes such as GTAW, require a thermal treatment to relieve stresses. As is the case for welding, stresses in micro-weld deposits are expected to be tensile in nature. Using a beam deflection analysis method, the nature and approximate magnitude of residual stresses in micro-welded deposits were obtained.

3. LITERATURE SURVEY

3.1 HISTORY AND APPLICATION OF MICRO-WELDING

Johnson [1] gives an excellent historical overview of the electro-spark deposition process followed by descriptions of the performance and applications of the process in nuclear and fossil energy environments. The first reference to the effects of spark treatment on surface properties dates back to 1924 by H.S. Rawdon. It was discovered that when iron was sparked with an iron electrode, its surface became very hard as compared to the bulk material. The increase in hardness was due to the formation of martensite at the surface where sparking had occurred and the material cooled very rapidly.

N.C. Welch also obtained the same results as H.S. Rawdon but also went on to show that the surface hardness could be influenced by the choice of medium in which the sparking occurred. For example, the presence of oxygen and nitrogen each influenced the hardness, while sparking of titanium in oil produced high surface concentration of titanium carbide.

The process appears to have been heavily researched in the USSR and many published works on application of the micro-welding process to prolong cutting tool life are available.

The micro-welding process is very similar to arc-welding. However, the most noteworthy difference is the reduced heat input to the substrate. The heat generated is less than 1% that of arc welding and allows for extreme rapid solidification of the weld pool. Under normal processing conditions, the substrate remains at ambient temperature and is virtually free from a heat affected zone and residual stresses that would be present by arc-welding. The resulting coating is very fine grained and approaches an amorphous or glassy structure. Further,

micro-welded coatings are usually harder, stronger and have a better corrosion resistance than the same material with normal microstructures and grain sizes.

Micro-welding equipment consists of a resistance-capacitance circuit where the electrode is in contact with the substrate. To prevent fusion of the electrode to the substrate, it is rotated or vibrated during the welding process. As is common with other welding processes, automation is required in order to achieve reproducible coatings. However, where high deposition rates are required, manual application is used but the quality of applied coatings depends greatly on the skill of the operator.

The micro-welding process is carried out in air or with inert assist gases such as Ar, N_2, He, CO_2. Argon accounts for 90% of inert gas usage in processing and promotes a fine spray transfer mechanism and produces better coatings. Air and nitrogen are not as commonly used but promote a globular transfer of electrode material and result in higher deposition rates.

Nearly any conductive material or cermet capable of being melted in an electric arc can be micro-welded. Chromium silicide and carbon graphite, which don't have a molten phase at atmospheric pressures, don't transfer to any significant extent. Electrodes are normally cylindrical in shape and 3 to 6 mm in diameter. Substrates must also be electrically conductive and capable of being melted. As molten electrode material is transferred to the substrate, mixing occurs with the molten pool of substrate material. This dilutes the composition of the coating for the initial 12 to 20 μm of material being deposited. Beyond this thickness, the coating assumes the composition of the electrode. The mixing process produces a transition in properties of the coating and a true metallurgical bond to the substrate

which explains why micro-welded coatings are far more resistant to spalling than D-gun coatings.

Deposition rates are limited by the total heat input that can be tolerated to retain the unique properties and advantages of the process. At high energy levels, rapid solidification ceases to occur and a heat affected zone is formed. At this point, the process essentially becomes arc-welding. To achieve the full benefit of the micro-welding process, heat input is kept to a minimum and yields low deposition rates. The coating hardness can also vary with deposition rate as it relates to the cooling rate of deposited material. Low deposition rates lead to rapid solidification of the coating and produces harder coatings.

The applied coating thickness can range from 3 to 250 μm or more with thinner coatings being better. Internal residual stresses in the coating are a function of process parameters and thickness.

The majority of micro-welding applications have been for wear protection of cutting tools and machine components using WC or TiC electrodes. The nuclear industry has seen recent uses of this technology for reactor core components. A more recent application has been to aircraft gas turbine engine components. Applications include coating of z-notch surfaces of turbine blades, corrosion resistance to blade tips, first step in platinum-modified coatings on turbine blades, repair of damaged diffusion coatings and build-up of nickel-base alloys to reclaim close tolerance parts.

3.2 STRUCTURE OF MICRO-WELD DEPOSITS

By use of electron fractography, Korobeinik et al [3] studied the microtopography, microstructure and substructure of iron-carbon alloys. During the micro-welding process, the electrode is in vibration and transverse motion of the substrate. This causes a range of microtopographies that can be classified into three groups: plasma, droplet and contact transport mechanism.

The plasma transport topography is generally featureless while droplets can be readily seen with the droplet transport mechanism. The zone of contact transport comprises of droplets destroyed during the electrode contact and is seen as bridging within the coating. The zone of plasma transport has the best service properties of the three types. It has maximum hardness and highest protection against wear and corrosion. It is also relatively high in chemical homogeneity. The zone of contact transport has the worst properties of the three possible transport mechanisms.

The mode of transport has been shown to depend on processing parameters such as voltage, current, capacitance and on substrate and electrode materials. An increase in voltage increases the fraction of plasma transport while decreasing the capacitance increases contact transport.

The authors proposed that during the micro-welding process, the substrate surface is subjected to high temperature and pressure and that approximately 25% of the crater volume reaches its boiling point and the surface pressure of the electrode reaches hundreds of atmospheres. Consequently, an austenite-martensite mixture forms in the surface layers of

steel. A three-dimensional network (Frank Network) has been described to form on the surface. The sub-boundaries are a combination of simple hexagonal networks of screw dislocations low energy, high stability and ability to hinder dislocations. These sub-boundaries localize the deformation in the volume of the sub-grain. When heat is applied, dislocations can slip through the structure. This relaxes internal stresses and reduces the occurrence of brittle cracking.

The observed sub-structure explains the occurrence of the boundary layer effect. The boundary layer effect is described as cracking of the micro-welding surface layer when a critical misorientation between adjacent sub-grains is achieved. The increase in misorientation is driven by the increase in density of dislocations in the cell walls during the micro-welding coating build-up process.

Paustovskii et al [2] measured the internal stresses of micro-welded coatings and laser treated surfaces. The Davidenkov Method for determination of internal stresses in coatings is described and compared to x-ray diffraction analysis. The Davidenkov Method is based on a deflection measurement of the coating as it is chemically etched from the substrate. Internal stresses are calculated using the formula:

$$\sigma = \frac{Ed^2}{3l(1-\mu)} \quad \frac{\Delta f_k}{\Delta h}$$

where E is the modulus of elasticity, μ is Poisson's coefficient, d is the specimen thickness, l is the specimen length, f is the sag and h is the thickness of the removed layer.

However, this method is limited to providing an averaged internal residual stress value. In reality, as the coating is built-up on a substrate the temperature decreases with increased thickness. The structure becomes inhomogeneous and leads to non-uniform stresses in the thickness. A better suited method for the determination of internal stresses is by using x-ray diffraction to measure the variation in lattice constant within the coating which is directly tied to local internal stresses. Using the following formula, the authors compared the residual stresses of tungsten, chromium, zirconium and molybdenum on steel alloy no. 45:

$$\varepsilon = \frac{\Delta d}{d} = \frac{1+\mu}{E}\sigma \sin^2 \psi$$

where ε is the elastic deformation, σ is the residual stress, d is the interplanar distance, Δd is the interplanar distance variation, μ is Poisson's coefficient, E is the modulus of elasticity and ψ is the slope angle of the x-ray beam toward the specimen surface.

According to the authors, residual stresses in the coating depend on the nature of the alloying metal. In the alloyed layer, cracks are formed due to residual tensile stresses on the boundary surface micro-weld layer. Lower residual stresses (180 – 450 MPa) were obtained with vanadium and chromium, metals that form unlimited solid solutions with iron. Higher residual stresses (600 – 1000 MPa) were obtained with titanium and zirconium and were explained by the micro-welded surface heating up to polymorphic transition temperatures of these metals.

Although the Davidenkov Method of calculating residual is not recommended, an expression based on the deflection of the etch-removed coating was used in the current study to approximate the magnitude of internal stresses in the micro-welded coatings.

3.3 PERFORMANCE OF MICRO-WELDED COATINGS

The spalling, friction and wear performance of micro-welded WC-TiC and Cr_3C_2 coatings to type 316 stainless steel have been compared by Sheldon et al [4]. Comparative wear tests using a WC sphere were also performed on micro-welded and detonation-gun deposited Cr_3C_2 coatings.

Spalling Test Results

Using a friction-wear spalling test device, the Cr_3C_2 coating showed slight smoothing after 1000 cycles of oscillation under the loaded WC sphere. There was a small amount of surface wear and considerable flattening of the WC sphere was observed with no evidence of coating failure. Some signs of wear were evident on the WC-TiC coating tested under the same conditions. There was no evidence of spalling or shattering of the surface layer of either coating.

Friction Test Results

Similar results were obtained for both coatings; a 15% increase in friction was obtained in going from 10 to 1000 using the friction-wear spalling test device.

Wear Test Results

An improvement of two orders of magnitude was achieved in wear of a micro-welded WC-TiC coating over the uncoated steel and a one order of magnitude improvement over full hard 1090 steel.

Cr_3C_2 was applied by micro-welding and detonation gun for comparative testing. At low contact stresses, both coatings had similar wear rates. As contact stresses increased, the wear rate of the D-gun deposited coating increased exponentially while the rate of wear of the micro-welded coating remained virtually unchanged.

The reason for this drastic difference in wear rates is related to the structure and bonding of the coatings. The micro-welded coating is significantly finer grained, more homogenous and about 50% harder than the D-gun coating. Also, the micro-welded coating is fused to the substrate by metallurgical bonding while the D-gun coating is primarily a mechanical bond.

It has been shown by Sheldon et al [5] that the formation of a series of alloys form when pure nickel is micro-welded to titanium alloy 6Al-4V. In an attempt to obtain an amorphous structure, the discharge pulse capacitor was adjusted until the maximum deposit was achieved while maintaining minimum pulse energies.

Electron microprobe analysis showed that titanium fused into approximately 50% on the coating over a distance of 5 μm. The structure of micro-welded coatings on 600 grit finish versus grit blast with 320 mesh silica sand were studied with x-ray diffraction (XRD) on the top-most surface of each micro-welded coating for as-deposited, 30%, 60% and 95% polished conditions. This provided structure compositions over the depth of the coatings.

The micro-welded coating over the 600 grit ground surface was predominantly of the disordered Ni-Ti structure. There was an increase in lattice parameter of Ni-Ti from as deposited to 60% polished, which indicates a wide compositional ranges formed by rapid solidification from the liquid state.

The grit-blasted surface micro-welded coating consisted of a mixture of Ti, Ni-Ti and $Ni\text{-}Ti_2$ phases. The presence of Ti over a broad range of thicknesses suggests that the coating is very thin or perhaps even unalloyed at the interface. The roughness of the surface prevented the formation of a thick Ni-Ti coating.

It has been shown by Zhengwei et al [6] that the elevated temperature oxidation resistance of a Ti_3Al-Nb alloy (65Ti-24Al-11Nb) substrate is improved by producing micro-welded aluminide coatings. Ti_3Al intermetallic compounds have high temperature strength and low density which makes them attractive for aerospace applications.

A > 99% pure aluminum electrode was micro-welded to Ti_3Al-Nb alloy test specimens. Using energy dispersive spectroscopy line scanning, the aluminum concentration was measured to be greatest in the outer layer of the 10 μm thick coating and to gradually decrease to its average value present in the Ti_3Al-Nb alloy substrate. At the interface, $TiAl_3$ was formed by the mixing of molten aluminum electrode material and the substrate. The coated specimens were exposed tested in air at 800 and 900°C. The change in mass versus time was measured for a total exposure of 168 hours (7 days).

After 168 hours, the coated specimens experienced a mass gain one quarter that of the uncoated specimens at both temperatures. The mass gains of coated specimens were very

similar with the 900°C exposed specimen being slightly higher. The mass gain of the uncoated specimen exposed at 900°C was approximately 35% greater than that of the uncoated specimen exposed to 800°C.

The oxides formed on the uncoated Ti_3Al-Nb specimens exposed to 800 and 900°C were mainly TiO_2, with a small amount of α-Al_2O_3. Using x-ray diffraction, the oxide structures from surface to interior were determined to be:

- Uncoated specimens (800 and 900°C): rutile, alumina, thick rutile with small amounts of alumina with Nb, titanium nitride at the interface
- Coated specimen (800°C test): continuous (not uniform) scale layer of approximately 3 μm with two sublayers of Al_2O_3 (outer) and Al_2O_3 with TiO_2 (inner)
- Coated specimen (900°C test): dense α-Al_2O_3 layer of approximately 5 μm.

The otherwise thermal mismatch that would exits if $TiAl_3$ were deposited directly over Ti_3Al was eliminated due to a gradual transition and metallurgical bonding of Ti_3Al at the interface to $TiAl_3$. Consequently, the coating remained free of cracks. Being an excellent alumina former, $TiAl_3$ present in the outer portion of the coating produced an effective Al_2O_3 protective scale layer. It has been proposed by the authors that in a micro-welding coating, the grain size is in the order of a few hundred nanometres. The oxide grains that form during oxidation would be of similar size and provide the observed improved spallation resistance by resisting thermal stresses.

Brown et al [7] have shown that the life of high speed steel (HSS) alloy M2 machine cutting tools is improved by the application of micro-welded coatings to the flank and face to reduce

wear and cutting forces. The advantages of using HSS for cutting tools are its toughness, ease of sharpening and lower cost. The disadvantage when compared to TiC, WC and TiN is a lower hot hardness. Therefore, in order to keep the tool below its softening point, cutting speeds must be kept lower.

The traditional failure mode for HSS tools has been crater wear of the tool face where the chip flows across the face. Coating of cutting tools has been used since the 1960's to increase tool life, improve surface quality of the product and increase production rate (cutting speed). The prevalent commercially available phase vapour deposition coatings on HSS tools are TiC, TiN, Al_2O_3, TaC, WC and TiB_2 due to their good hot hardness and chemical stability. Since the micro-welding process is well suited for applying any electrically conductive material that can be melted in an electric arc, the process has the ability to apply materials that could not otherwise be applied by PVD.

Preliminary screening tests were carried out and tested for cross cylinder wear in accordance with ASTM G83 for the following alloys:

- A: 71.5%WC, 12% TiC, 10.5% TaC, 6.5% Co
- B: 69% WC, 20% TiC, 6% Ni, 4% TiC
- C: TiB_2 with unknown binder
- D: 64% WC, 26% TiC, 4.5% TaC, 6% Co
- E: 70% TiC, 18% Mo, 12% Ni
- F: TiC, unknown % Co
- G: 78% WC, 12% TiC, 5% TaC, 5% Ni

The capacitance, voltage, current and frequency were adjusted to optimise the coating for minimum wear. Actual parameters were not reported. Using CO_2 shield gas was slightly better than argon and nitrogen. Coatings A, B, and C were superior to D, E, F and G and were comparable to the control TiN PVD coated cylinder.

Cutting tool wear tests were run with coatings A, B, and C applied by micro-welding with a side-to-side motion to the face and flank surfaces of HSS cutting tools. Tests were also run with uncoated HSS and TiN PVD coated HSS tools for comparison to micro-weld coated HSS tools. All except the TiN PVD coated HSS tool failed after 60 metres of cutting distance. The application of a micro-weld coating to both surfaces did not significantly improve the tool life over uncoated HSS. The TiN PVD coated HSS tool was superior to the micro-weld coated tools. The power consumption (cutting force) was significantly lower for the C alloy micro-weld coated tool over all other tools.

In the next series of tests coatings A, B and C were only applied to the face of HSS cutting tools with a side-to-side electrode motion. The micro-weld coated tools showed an increase in tool life over the uncoated HSS tool. Coating B and the TiN PVD coated tools both failed after some 240 m of cutting distance and had the least amount of face wear. The power required for cutting increased for all except for the C coated tool.

The failure in the B micro-weld coated tool was determined to be by local breaks through the coating. Therefore, by micro-welding in a front-to-back motion over the tool face, a more uniform coating thickness will result and the cutting edge will be subject to less heating by sparks. Tests were repeated with alloy B only. The coated tool had no indication of breakthrough after 440 m of cutting. A minimum of 200% increase in tool life was achieved

over the side-to-side alloy B micro-weld coated tool and the commercially available TiN PVD coated HSS tool. Additionally, the cutting force required for the alloy B micro-weld coated tool decreased with cutting distance.

3.4 REPAIR OF TURBINE BLADES AND VANES

Antony et al [8] and Gandy et al [9] discussed extensively the past, present and future trends in gas turbine blade and vane repair. The high replacement cost of blades and vanes has made it cost effective for engine repair and overhaul facilities and OEM's to develop processes to recover these parts. In service, blades and vanes suffer from dimensional changes caused by wear, nicks, dents, hot corrosion and stripping of protective coatings. They also suffer from metallurgical degradation caused by fatigue and hot corrosion.

Blade repairs are mainly to restore their tips to maintain close tolerance against abradable seals. GTAW is the most common method of repair but plasma, laser and electron beam welding are used increasingly. Nearly all turbine blade are cast (SX or DS) from nickel base superalloys with concentrations of aluminum + titanium $\geq$ 3%. Consequently, the alloys are only moderately weldable and some degree of microcracking cannot be avoided. To reduce the amount of microcracking, filler alloys are selected accordingly with relatively lower concentrations on aluminum and titanium. As a result of using more weldable filler alloys, the strength of the repaired area/volume is significantly less than that of the parent blade material. For example, Inconel 625 is a solid solution strengthened alloy commonly used filler for GTAW to repair nickel base alloy blades.

Turbine vanes are often cast out of cobalt base alloys and are more readily repaired by manual GTAW using cobalt based alloy fillers. They do not suffer from microcracking as nickel base alloy components. Vane repair involves bending to restore their geometric shapes or by welding in replacement vane sections. Welding of cobalt based vane alloys must be carried out in the annealed condition in order to avoid cracking.

Brazing and braze-welding are processes used to repair cracks in nickel base alloy components. The preparation of cracked surfaces is extensive as it requires the removal of surface oxides and scale to ensure wetting of the filler material. True crack repair is seldom achieved since it is nearly impossible for the molten filler metal to completely wet the crack surfaces up to the crack tip. Although non-destructive surface inspection reveal no defects, cracks remain in the component and can reduce component strength.

Ceramic coatings such as yttrium-stabilized zirconia are applied by thermal spray processing. Ceramic coatings are applied to a "bond-coat" made up to NiCrAlY initially applied to the substrate. Yttrium is an inert element added to coatings to reduce oxide scale spallation.

Future trends in repair of vanes and blades is towards automation of the weld overlay process. At time of writing, the majority of weld overlays are applied manually on a part-by-part basis and is labour intensive. The development of automated equipment will require that it be capable of adapting to the variations in shape and wear of each blade and apply the weld overlay where it is required only.

Banerjee et al [10] have shown that the susceptibility of Inconel 738LC to cracking in the GTAW heat affected zone can be reduced by using filler alloys with a slower aging response,

have less lattice mismatch between the precipitating phase and the matrix and are softer. Being a microstructurally stable alloy at high temperature, it is commonly used on hot-end components of aircraft gas turbines. Inconel 738 is a precipitation hardenable alloy strengthened by the γ' phase Ni_3,(Al, Ti) and MC-type carbides. $M_{23}C_6$ provide high temperature grain boundary strength.

Weld trials were conducted on as-cast Inconel 738LC with Nimonic 263, Rene 41, FM-92 and Inconel 718 filler alloys. Tests were duplicated to study the effect of a standard pre-weld heat treatment at 1120°C for 2 hours followed by air cooling to a new heat treatment developed by Thakur et al [11]. The filler alloys were selected based on their relative content of aluminum + titanium content. The average total crack length and weld hardness were found to be the greatest for Nimonic 263 and Rene 41 filler alloys, both of which are γ' strengthened alloys. Reduced cracking and softer welds were measured for FM-92 and Inconel 718. Inconel 718, being mainly strengthened by the γ'' phase which precipitates much slower than γ' did not precipitate during the weld cooling cycle. Therefore, the softer more ductile welds were able to withstand more welding stresses induced by welding and led to reduced micro-cracking.

Thakur et al [11] studied the effects of pre-weld heat treatments on the cracking tendency of cast Inconel 738. After repeated exposure to elevated temperatures, components are repaired by manual GTAW and are susceptible to microcracking in the weld and heat affected zone. Cracking is caused by (1) strain age cracking which depends on the size and shape of γ' precipitates and the nature of secondary precipitation of coherent γ' precipitates during the welding process and (2) the structure of grain boundaries and precipitates on them which influences the deformation of grain boundaries by sliding and liquation of precipitates on the

grain boundary. As discussed earlier, the traditional method of reducing the extent of cracking is to use a softer, solid solution strengthened weld filler alloy such as Inconel 625. However, when using Inconel 625 the repaired component has reduced tensile, corrosion and creep properties.

To reduce the susceptibility to microcracking, a pre-weld heat treatment was developed such that the volume fraction of γ' in the material is reduced, the volume fraction of $M_{23}C_6$ precipitates at the grain boundaries are reduced to discrete particles surrounded by γ'and the morphology of grain boundaries is changes from linear to serrated. The resulting weld and heat affected zone were nearly free of microcracking by solutioning at 1120°C, air cooling followed by aging at 1025°C for 16 hours and water quenched.

3.5 ELEVATED TEMPERATURE OXIDATION

It has been shown by Zhengwei et al [13] that micro-welded coatings can dramatically improve the oxidation resistance of stainless steels and nickel alloys. The spallation of oxide scales has been eliminated by micro-welding alumina and chromia forming coatings.

Aluminum and FeCrAl coatings were deposited to AISI 304, 310 and 430 stainless steels and Inconel 600 (Ni-15Cr-8Fe). Electrode materials were pure aluminum (>99.9%) and Fe-25Cr-5Al wire. Oxide dispersed FeCrAl coatings were also produced by using a fine Y_2O_3 powder during the micro-welding process. Y_2O_3 is a common additive to thermal coatings for reducing spallation of protective oxide scales.

Coatings were applied to oxidation test specimens in two steps. The first consisted of a higher pulse power (0.13 Joules per discharge) in order to deposit a thick base. The second step consisted of a reduced pulse power application (0.067 Joules per discharge) in order to deposit a low porosity and smooth outer coating. Prior work by the authors had shown that oxidation resistance of micro-welded coatings increased as the amount of micro-porosity, cracks and roughness of coatings are reduced. Therefore, the selection of micro-welding process parameters can have an effect on the oxidation resistance of applied coatings.

The oxidation resistance of AISI 304 stainless steel at 1000°C was dramatically increased by coating with aluminum, FeCrAl or FeCrAl+ Y_2O_3. The coated specimens were also free from spallation and followed parabolic oxidation rates. The uncoated specimen suffered from severe spallation and followed a negative linear oxidation rate indicative of scale spallation. The mass gain of uncoated 304 stainless steel was approximately two orders of magnitude greater than coated specimens (100 mg/cm^2 versus 1.5 mg/cm^2 after 100 hours). Of the coated specimens, the FeCrAl+ Y_2O_3 coating provided the best oxidation resistance (0.85 mg/cm^2), followed by aluminum (1.3 mg/cm^2) and FeCrAl (1.5 mg/cm^2).

AISI 430 stainless steel coated with aluminum was tested at 900°C for 100 hours. The oxidation behaviour of uncoated 430 stainless steel was initially parabolic in nature and changed to a linear rate after approximately 20 hours. After 100 hours, the mass gained by the uncoated specimen was 8 mg/cm^2. The oxidation behaviour of the coated specimen followed a parabolic oxidation rate and had a mass gain of 1.2 mg/cm^2 after 100 hours.

AISI 310 stainless steel specimen was coated with FeCrAl+ Y_2O_3 and tested at 1100°C for 100 hours. The coated specimen followed a parabolic oxidation rate over the duration of the

test and had a mass gain of 1.4 mg/cm^2. The uncoated specimen initially followed a parabolic rate but rapidly decreased after 20 hours and followed a negative linear rate. As was the case for 304 stainless steel, the negative linear rate corresponded to scale spallation.

Inconel 600 was coated with aluminum and tested at 1000°C for 200 hours. The coated specimen had an initial steep linear oxidation rate until approximately 10 hours and changed to a parabolic rate. The coated specimen had a mass gain of 0.8 mg/cm^2 compared to 1.5 mg/cm^2 for the uncoated specimen.

X-ray diffraction showed that Al_2O_3, Cr_2O_3 and a small amount of spinel oxide $FeCr_2O_4$ formed on the surface of aluminum and FeCrAl micro-welded coatings. These oxides scales provided better oxidation and spallation resistance to all stainless steels. The authors suggest that the high dispersion of Y_2O_3 particles in the FeCrAl+ Y_2O_3 coating act as diffusion barriers to aluminum. This would promote the growth of Cr_2O_3 scale and limit the growth of Al_2O_3. This would account for the reduced oxidation rate (mass gain) observed with the FeCrAl+ Y_2O_3 coating. The X-ray diffraction of the scale formed on the Inconel 600 specimen coated with aluminum showed strong NiAl peaks. Correspondingly, of the possible Ni-Al alloy phases, NiAl has the highest oxidation resistance. Aluminum, being a slower diffuser than chromium and iron in nickel would promote the growth of Al_2O_3 by remaining on the surface of Inconel 600.

Great improvements were made on the spallation resistance by formation of thinner oxide scales on micro-weld coated specimens. Uncoated stainless steel specimens tend to form thicker oxides of Fe_3O_4 and $FeCr_2O_3$ which are less protective than Al_2O_3 and Cr_2O_3. Oxides have lower coefficients of thermal expansion and are subject to growth stresses when they

reach relatively high thicknesses. Thermal cycling during the oxidation tests can also induce significant stresses in the scales. Therefore, the weakly adhering thicker scales formed on uncoated stainless steels spalls rather easily, exposes the bare material and leads to the observed linear oxidation rate. The fine grain structure of oxide scales formed on micro-welded coatings was finer grained and contained micro-cracks. The combined effect of these features could allow stress relief in the coatings during growth and thermal cycling. The authors also propose that during the micro-welding process, the impact applied by the rotating electrode induces compressive stresses and defects in the coatings which could improve scale adherence by balancing internal tensile stresses.

Wei et al [12] studied the effect of a 1 wt.% addition of aluminum to a Cr-28% nickel base alloy. Oxidation tests were carried out on Ni-28Cr and Ni-28Cr-1Al alloys in air at 800 and 1000°C. The formation of oxides was studied at intervals over the duration of the tests using scanning electron microscopy, X-ray diffraction and electron probe micro-analysis.

At 800°C, the Ni-28Cr alloy had a granular topography with the granules aligned with abrasion marks. After 1000 hours, nickel-rich oxide protrusions were observed and their locations correlated to grain boundaries in the base material. An irregular scale thickness was determined to be as a result of blister development, scale spallation and nodule formation process. The scale to alloy interface was also irregular. The external oxide layer was determined to consist predominantly of Cr_2O_3 with significant amounts of nickel-rich oxide on its outer surfaces. Only a small amount of internal oxide precipitation (Cr_2O_3) was observed.

At 1000°C, the Ni-28Cr alloy had oxide grains similar to those observed in the 800°C tests. Spallation increased and nickel rich oxide granules became more pronounced on the scale surface. Discrete internal oxide precipitates were observed along with local penetrations of internal oxides along grain boundaries beneath the oxide scale. Voids and metallic particles were observed within the oxide stringers along with voids in the alloy. The external oxide scale was analysed to be Cr_2O_3 with a layer of NiO on the external surface while the internal precipitates were Cr_2O_3 rich.

At 800°C the Ni-28Cr-1Al alloy's external oxide was granular and consisted of Cr_2O_3 with no nickel present. Internal oxidation formed to a uniform depth but was deeper along grain boundaries. The internal precipitates were Al_2O_3.

At 1000°C, the Ni-28Cr-1Al alloy showed significant amount of spalling. The surface scale was Cr_2O_3 with small amounts of nickel. The Cr_2O_3 scale grew inward with fingers of oxide penetrating the alloy. Along grain boundaries, extensive voids were also observed. Internal oxide and inter-granular precipitates were Al_2O_3.

In the early stages of oxide formation, NiO and Cr_2O_3 external oxides developed until a complete healing layer of Cr_2O_3 was formed. In the binary alloy, the oxide scales were irregular with large nodules. This is explained by local failure of the Cr_2O_3 scale, followed by the formation of a nickel rich oxide in the now chromium depleted zone. In the ternary alloy, a more rapid formation of a Cr_2O_3 healing layer occurred at 1000°C with less nickel rich oxide being formed as a result of a reactive element effect. Aluminum is more reactive than chromium and acts as a getter of oxygen to reduce the ingress of oxygen in the alloy. This allowed the healing layer to form more rapidly.

In the binary alloy, Cr_2O_3 oxides were observed at discrete particle below the scale and along grain boundaries. The voids formed are likely to be a result of a Kirkendall effect where vacancies are generated by unequal fluxes of chromium from the bulk material to the surface and of nickel in the opposite direction. The formation of voids in the chromium depleted zone supports this hypothesis. Internal and inter-granular oxides were Cr_2O_3.

The ternary alloy's internal oxides were Al_2O_3 while the deep inter-granular oxides were Al_2O_3 and Cr_2O_3. The addition of 1 wt.% aluminum did not help prevent intergranular oxidation as it actually increased it but helped to increase the rate of formation of the Cr_2O_3 healing layer.

4. EXPERIMENTAL PROCEDURES

4.1 MATERIALS

The principal goal of this study was to investigate the effects of process parameters on micro-welded coating deposition rate and quality in order to optimize a simulated repair to a cast Inconel 738 substrate. Inconel alloy 738 is a γ' strengthened nickel based superalloy commonly used in aircraft gas turbine components such as turbine blades, frames and stator vanes due to its excellent high temperature creep-rupture strength and hot corrosion resistance. However, cast Inconel 738 is very susceptible to heat affected zone cracking during welding. The use of softer solid solution strengthened filler alloys or an optimized over-aging pre-weld treatment are required in order to minimize the extent of cracking.

The micro-welding electrode alloys were selected based on their current use in commonly repaired components and range of aluminum + titanium concentrations. Refer to Table 1 for chemical compositions of materials used in this study.

Table 1: Chemical composition of materials (wt.%)

	iN738 (Notes 1 & 2)	iN625 (Note 3)	iN722 (Note 3)	IN718 (Note 3)	N-105 (Note 3)	R41 (Note 3)
C	0.17	0.1 max	0.08	0.08 max	0.12 max	0.12 max
Co	8.5	1.0 max	0.0	1.0 max	20.0	11.0
Cr	16.0	21.5	15.5	19.0	14.8	20.0
Mo	1.7	9.0	0.0	3.0	5.0	9.75
W	2.6	0.0	0.0	0.0	0.0	0.0
Ta	1.7	-	0.0	-	0.0	0.0
Nb	0.9	3.65 (w/ Ta)	0.0	5.0 (w/ Ta)	0.0	0.0
Al	3.4	0.4 max	0.7	0.5	4.7	1.6
Ti	3.4	0.4 max	2.4	0.9	1.2	3.1
Al+Ti	**6.8**	**0.8 max**	**3.1**	**1.4**	**5.9**	**4.7**
B	0.01	0.0	0.0	0.006 max	0.006	0.007
Zr	0.05	0.0	0.0	0.0	0.15	0.0
Fe	0.5 max	5.0 max	7.0	Balance	1.0 max	5.0 max
Mn	0.2 max	0.5 max	1.0 max	0.35 max	1.0 max	0.0
Si	0.3 max	0.5 max	0.07 max	0.35 max	1.0 max	0.0
S	0.015 max	0.015 max	0.01 max	0.015 max	0.01 max	0.0
Ni	Balance	Balance	Balance	52.5 (w/ Co)	Balance	Balance
Cu	0.0	0.0	0.5 max	0.3	0.2 max	0.0
P	0.0	0.015 max	0.0	0.015	0.0	0.0
Pb	0.0	0.0	0.0	0.0	0.0015max	0.0

Notes:

1. **As-received composition**
2. **Composition of substrate and electrode material**
3. **Nominal compositions of electrode material**

4.2 SPECIMEN PREPARATION

4.2.1 WELD SPECIMENS

As-received cast Inconel 738 bars 6 mm thick by 25 mm wide by 175 mm long were abrasive blasted with 180 grit aluminum oxide to remove the non-conductive surface scale. Using a rounded graphite electrode with a radius of 16 mm, spherical divots 0.6 mm deep by 9 mm in diameter were electrical-discharge machined in the bars with a Charmilles Technologies Roboform die sinker machine. The electrical-discharge machined surfaces were subsequently removed by mechanical grinding with a carbide ball tool. The bars were sectioned to make individual specimens that were identified and weighed to the nearest 0.0001 gram.

4.2.2 OXIDATION TEST SPECIMENS

Five specimens approximately 15 mm square by 6 mm thick were sectioned from the as-received Inconel 738 cast bars using a friction cut-off wheel. The surfaces were abraded sequentially with 120, 220, 320, 400 and 600 grit silicon carbide abrasive paper to remove surface scale from the casting process and heat affected surfaces from friction cutting and provide a smooth surface for micro-welding. The specimens were identified and weighed to the nearest 0.0001 gram.

4.2.3 RESIDUAL STRESS SPECIMEN

A 1.0 mm thick mild steel sheet was used as a substrate that could be removed by acid dissolution. Inconel 625 was micro-welded over an area approximately 15 mm by 40 mm using the following parameters:

- Frequency: 450 Hertz
- Capacitance: 30 micro Faradays
- Current: 2.8 Amperes
- Voltage: 110 Volts

4.3 ELECTRODES

The electrode materials were obtained from various sources as listed below:

- Inconel 625 – supplied by Advanced Surfaces And Processes
- Inconel 718 – casting, electrical discharge machined and swaged
- Inconel 722 – sheet, swaged
- Inconel 738 – casting, electrical discharge machined and swaged
- Rene 41 – weld wire, welded as a bunch, cast and swaged
- Nimonic 105 – gas turbine vane, electrical discharge machined and swaged

Refer to Figure 1 for a photograph of a typical micro-welding electrode.

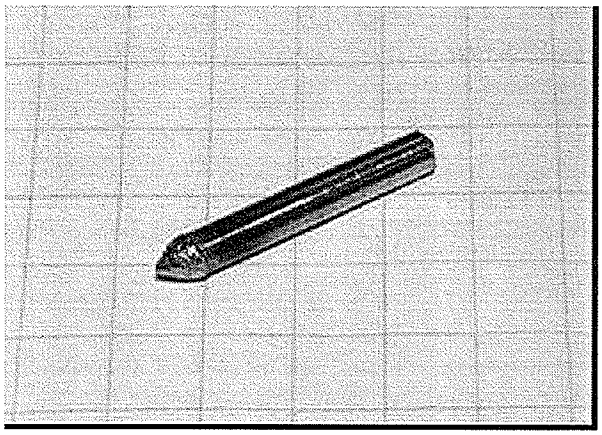

Figure 1: Micro-welding electrode shown with rounded contact point after use. Shown against 6 mm grid.

4.4 GAS TUNGSTEN ARC WELDING – BASELINE TESTING

A CANOX C-SW300 AD/DC gas tungsten arc welding power supply was used for gas tungsten arc welding baseline weld specimens. The welding process parameters were:

- Electrode: thoriated tungsten
- Filler: Inconel 625 wire
- Cover gas: argon
- Polarity: negative electrode
- Current pulse/wave: none, DC mode
- Voltage: 10±1 Volts
- Current: 20±2 Amperes

GTAW tests were conducted on cast Inconel 738 specimens in the following conditions:

- As cast
- Solution treated with pre-heat prior to welding

4.5 MICRO-WELDING

4.5.1 POWER SUPPLY

The micro-welding equipment used in this study was a Model PS98 MKII power supply with a manually operated AH98 - MKIDD torch. Refer to Figures 2 and 3 for photographs of the equipment. Process parameters that were controlled during this study were:

- Cover gas: argon
- Pulse duration: 25 to 50 micro seconds
- Rotational speed: 1100 to 1200 revolutions per minute
- Traverse speed: 6 to 12 mm per second
- Orientation: 30 to 45 degrees from coated surface
- Contact force: approximately 1.0 N

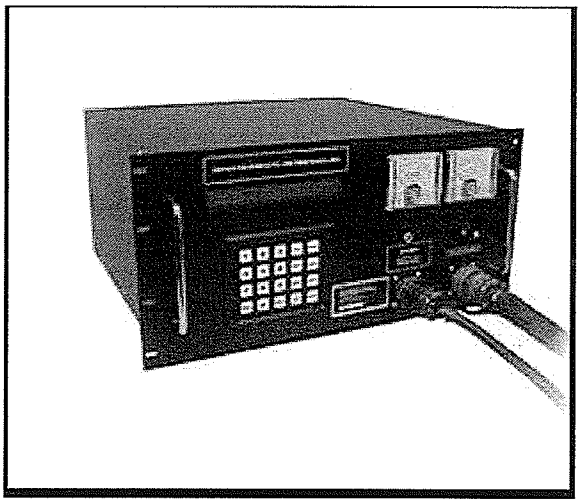

Figure 2: Micro-welding power supply

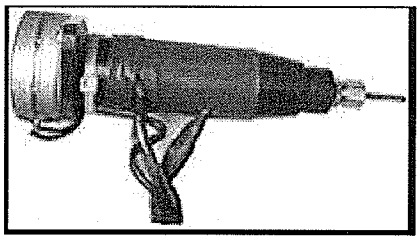

Figure 3: Hand-held torch

4.5.2 DESIGN OF EXPERIMENTS

To date, a parametric design of experiments that quantifies the main effects and interactions between the principal micro-welding process variables has never been published in the scientific literature. The three key pulse-arc variables under study are: voltage, current and capacitance. The pulse frequency depends on the selected parameters for voltage, current and capacitance and is a floating variable in industrial applications. Therefore, for the purpose of this study, the spark frequency was also allowed to be a floating variable.

Based on more than fifteen years of experience with the micro-welding process, Dr. John Kelley of Advanced Surfaces And Processing recommended a practical range of process parameters for a design of experiments. The recommended range was: 100 to 200 Volts, 3 to 5 Amperes and 20 to 50 micro-Faradays.

A 2-level, 3-factor with 3 center points design of experiments was devised for voltage, current and capacitance. Center points are included in designs of experiments in order to determine if curvature exists in the data and repeating the center point measurement three times is standard practice. Refer to Table 2 for the low (-1 in coded units), high (+1 in coded units) and center point values for the three variables (factors) under study.

The responses investigated in this study were:

1. Deposition rate
2. Void content (volume fraction)
3. Crack density (total length / unit area)
4. Coating hardness (on Inconel 738 only)

Table 2: Design of experiments

SPECIMEN NUMBER	CAPACITANCE (micro-Faradays)	VOLTAGE (Volts)	CURRENT (Amperes)
1	20	100	3
2	50	100	3
3	20	200	3
4	50	200	3
5	20	100	5
6	50	100	5
7	20	200	5
8	50	200	5
9	*30*	*150*	*4*
10	*30*	*150*	*4*
11	*30*	*150*	*4*

Minitab statistical analysis software was used to analyze the design of experiments for each response. The software is a powerful tool that can generate reports and several illustrative plots for analyses. The first of a series of plots generated by Minitab is the cube plot shown in Figure 4. The cube plot is a simple three dimensional summary of result for 2-level 3-factorial designs.

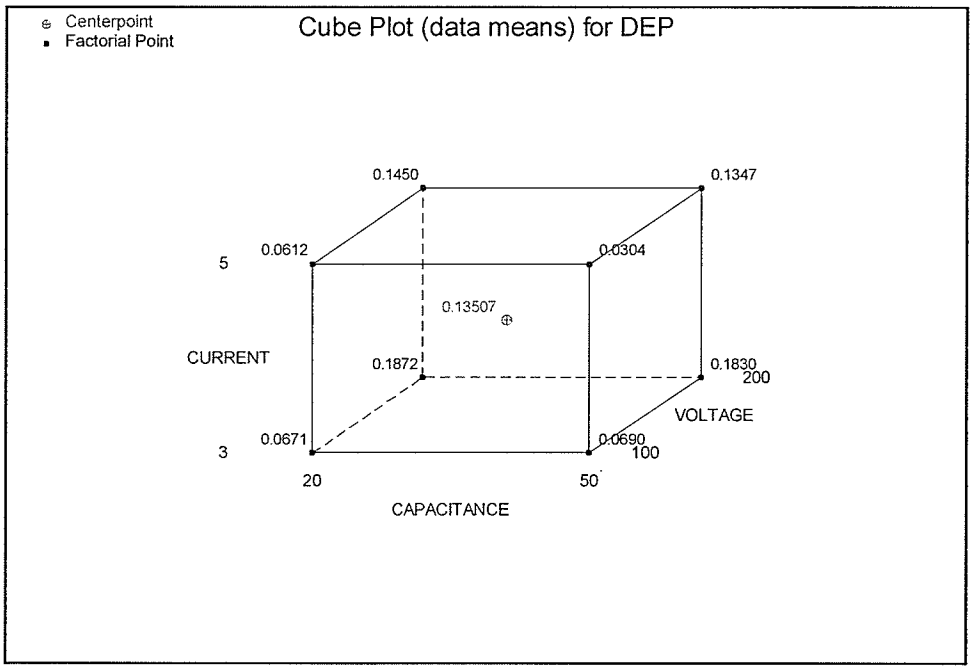

Figure 4: Cube plot for the deposition rate of Inconel 625

A sample Minitab report is shown below for the deposition rate of Inconel 625. All possible interactions have been considered in this report.

Fractional Factorial Fit: DEP versus CAPACITANCE, VOLTAGE, CURRENT

Estimated Effects and Coefficients for DEPOSITION RATE (coded units)

Term	Effect	Coef	SE Coef	T	P
Constant		0.10970	0.01453	7.55	0.017
CAPACITA	-0.01085	-0.00543	0.01453	-0.37	0.745
VOLTAGE	-0.03375	-0.01688	0.01453	-1.16	0.365
CURRENT	0.10555	0.05278	0.01453	3.63	**0.068**
CAPACITA*VOLTAGE	-0.00970	-0.00485	0.01453	-0.33	0.770
CAPACITA*CURRENT	0.00360	0.00180	0.01453	0.12	0.913
VOLTAGE*CURRENT	-0.01150	-0.00575	0.01453	-0.40	0.730
CAPACITA*VOLTAGE*CURRENT	0.00665	0.00332	0.01453	0.23	0.840
Ct Pt		0.02537	0.02781	0.91	0.458

Analysis of Variance for DEPOSITION RATE (coded units)

Source	DF	Seq SS	Adj SS	Adj MS	F	P
Main Effects	3	**0.0247952**	0.0247952	0.00826506	4.90	**0.174**
2-Way Interactions	3	0.0004786	0.0004786	0.00015953	0.09	0.956
3-Way Interactions	1	0.0000884	0.0000884	0.00008844	0.05	0.840
Curvature	1	**0.0014039**	0.0014039	0.00140393	0.83	**0.458**
Residual Error	2	0.0033757	0.0033757	0.00168785		
Pure Error	2	0.0033757	0.0033757	0.00168785		
Total	10	**0.0301419**				

An initial review of p-values provides information on the effect of terms in the DOE. The p-value is a calculated term ranging from 0 to 1 which describes the probability that two populations have the same mean value. Low p-values correspond to a high probability that the means are different and that a particular term has a significant effect on the response. It is common practice to use a threshold p-value of 0.05 for the results but this can be overly restrictive in some cases. Since the goal of this study is to establish a general understanding of the micro-welding process, a threshold p-value of 0.1 was used in order to expand the process modelling results.

Using the Minitab report, the variation contribution of sources is calculated manually. In the sum of squares (Seq SS) output table, individual values for effects, two-way interactions, three-way interaction and curvature are divided by the total variance and multiplied by 100. The calculated values provide a percentage of variance explained by individual sources that can be used in conjunction with p-values to analyze each response. In the sample report, it is concluded that only the CURRENT factor had a significant effect on the deposition rate of Inconel 625 (only factor with a p-value < 0.1).

The variance explained by the main effects is calculated as follows:

$$\frac{0.0248}{0.0301} \times 100 = 82.3\ \%$$

In this example, the p-value for the combined main effects (CURRENT, CAPACITANCE and VOLTAGE) is greater than 0.1 because only CURRENT had a significant effect on the deposition rate. A process model can still be generated provided that the curvature in the results is non-significant (p-value is < 0.1). If significant curvature is found, it indicates that the selected range of parameters is too broad for the process under study. The generation of process models in such cases will produce erroneous data.

Using the sum of squares (Seq SS) in the sample report the variance explained by curvature is:

$$\frac{0.00140}{0.0301} \times 100 = 4.7\ \%$$

With a p-value of 0.458, the curvature in the results is considered to be insignificant and allows the generation of a reduced model for CURRENT only. When running a reduced model, the non-significant factors are excluded from the statistical output to provide a more accurate model. Below is an example of the reduced model using the CURRENT factor for the deposition rate of Inconel 625.

Estimated Effects and Coefficients for DEPOSITION RATE (coded units)

Term	Effect	Coef	SE Coef	T	P
Constant		0.11662	0.008910	13.09	0.000
CURRENT	0.10555	0.05277	0.010448	5.05	**0.001**

Analysis of Variance for DEPOSITION RATE (coded units)

Source	DF	Seq SS	Adj SS	Adj MS	F	P
Main Effects	1	0.022282	0.022282	0.0222816	25.51	**0.001**
Residual Error	9	0.007860	0.007860	0.0008734		
Curvature	1	0.001404	0.001404	0.0014039	1.74	0.224
Pure Error	8	0.006456	0.006456	0.0008070		
Total	10	0.030142				

Estimated Coefficients for DEPOSITION RATE using data in uncoded units

Term	Coef
Constant	*-0.0944818*
CURRENT	*0.0527750*

P-values are now significantly less than the 0.1 threshold and the variance explained by the main effects and curvature are 73.9 and 4.7%, respectively. Therefore, a process model can be written as:

Deposition Rate of Inconel 625 (grams/hour) = -0.0945 + 0.0528 x I

where I is the process current (ranging from 3 to 5 Amperes).

Minitab also generates interactions and main effects plots as shown in Figures 5 and 6, respectively. In the interactions plots, parallel or near-parallel lines indicate that no interactions exist between the factors. A significant relationship would produce notable differences in the slopes of plotted lines. The main effects plot is a good visual aid to independently compare the effects of each factor on the response. The data means for each factor level are compared in the plots (i.e. mean of results for low current against the mean of result for high current).

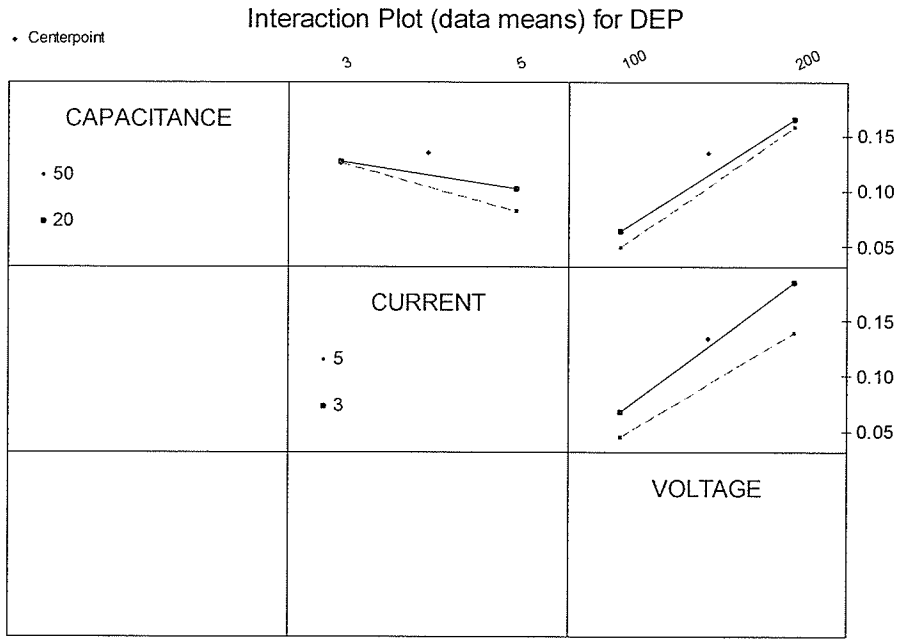

Figure 5: Interactions plot for the deposition rate of Inconel 625 (grams/hour)

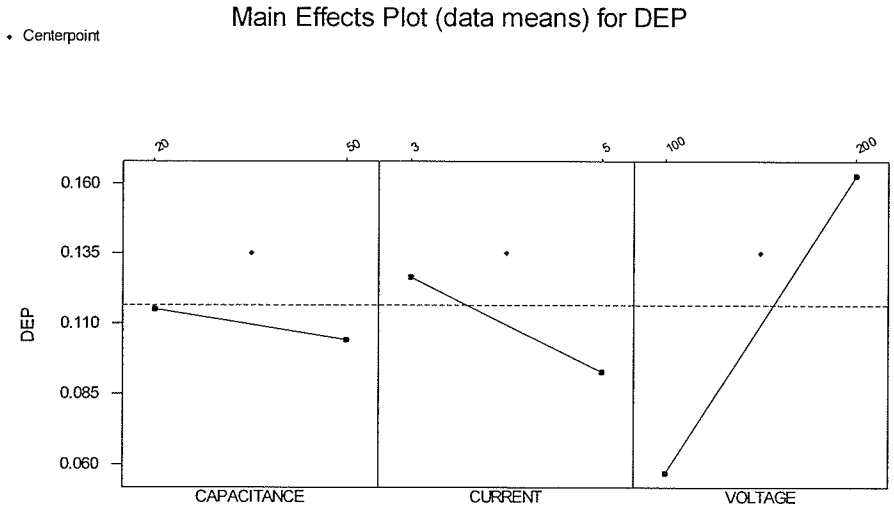

Figure 6: Main effects plot for the deposition rate of Inconel 625 (grams/hour)

The micro-welding machine was set-up for each combination of voltage, current and capacitance in accordance with the planned design of experiments listed in Table 2. The Inconel 738 specimens were micro-weld coated in the as-received condition. For each electrode material, the divots were filled with for a maximum period of 60 minutes or until a mound of approximately 0.5 mm protruded above the surrounding surface in instances of high deposition rates. Refer to Figure 7 to a photograph of Rene 41 micro-weld deposits.

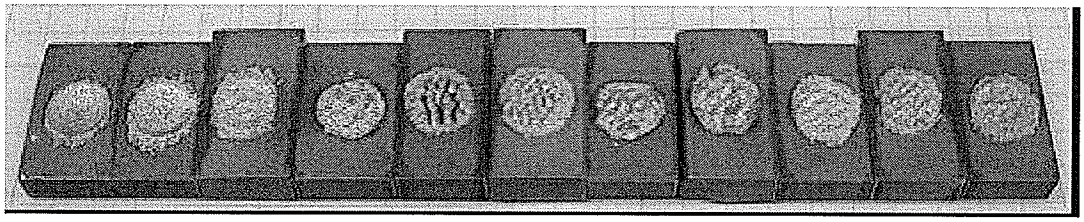

Figure 7: Rene 41 micro-welds. DOE specimen numbers 1 through 11 are in order from left to right

4.5.3 OXIDATION TESTS

Oxidation tests were conducted in accordance with the procedures outlined in ASTM G54 – Standard Practice for Simple Static Oxidation Testing.

One specimen (numbered 1) remained uncoated and served as a reference for comparison purposes. Specimen number 2, 3, 4 and 5 were coated with Inconel 738, Inconel 718, Inconel 722 and Nimonic 105, respectively. The coating alloys were selected based on their range of aluminum and titanium concentrations.

The process parameters used to apply the coatings for oxidation testing were:

- Inconel 738 coating – 460 Hz, 50 μF, 150 V, 4 A
- Inconel 718 coating – 400 Hz, 40 μF, 130 V, 4 A
- Inconel 722 coating – 380 Hz, 20 μF, 200 V, 3 A
- Nimonic 105 coating – 270 Hz, 50 μF, 200 V, 5 A

The mass of each specimen was measured to an accuracy of 0.0001 grams prior to and after applying micro-welded coatings to all surfaces. The oxidation test specimens were exposed to an air atmosphere at a temperature of 900°C for a total period of 168 hours. The specimens were removed from the furnace and allowed to cool for a period of 30 minutes prior to mass measurements at the following time intervals: 4, 8, 12, and every 24 hours thereafter.

Refer to Figure 8 for a photograph of oxidation test specimens prior to exposure and Figure 9 for a photograph of the air furnace.

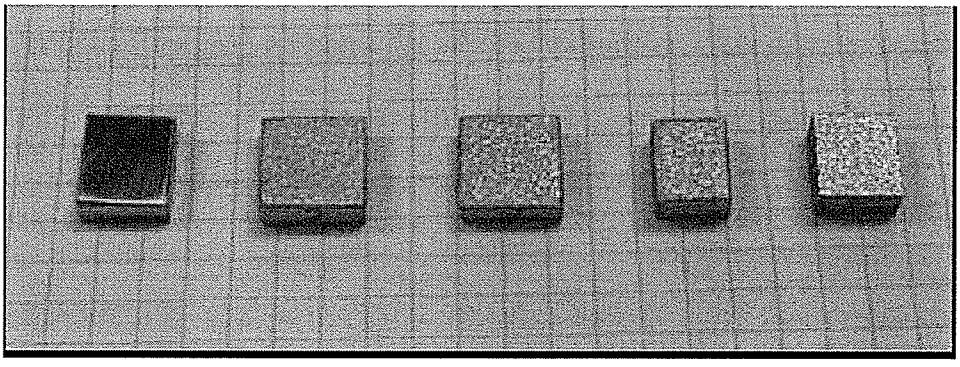

Figure 8: Oxidation test specimens. Left to right: uncoated Inconel 738, Inconel 738 coating, Inconel 718 coating, Inconel 722 coating and Nimonic 105 coating.

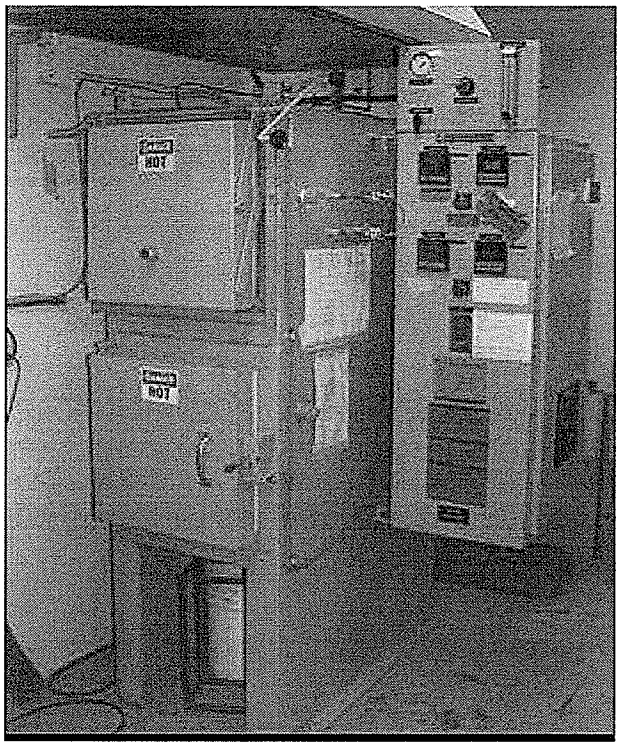

Figure 9: Oxidation test air furnace

4.5.4 RESIDUAL STRESS SPECIMEN

Using 450 Hz, 30 μF, 110 V and 2.8 A, Inconel 625 was micro-welded to a mild steel substrate. To avoid inducing stresses in the specimen, a 12.25 mm by 29.50 mm rectangular portion of the coated section was removed by electrical discharge machining. The mild steel backing material was then dissolved by immersing in 50% v/v nitric acid. The Inconel 625 micro-welded coating remained unaffected by the nitric acid.

Using a height gauge on a granite table, the coating's deflection at mid-span was measured at each end and at mid-length. Refer to Figure 10 for a photograph of the coating after the substrate was dissolved. The micro-weld coating was examined metallographically by optical microscopy and found to be relatively featureless with low porosity.

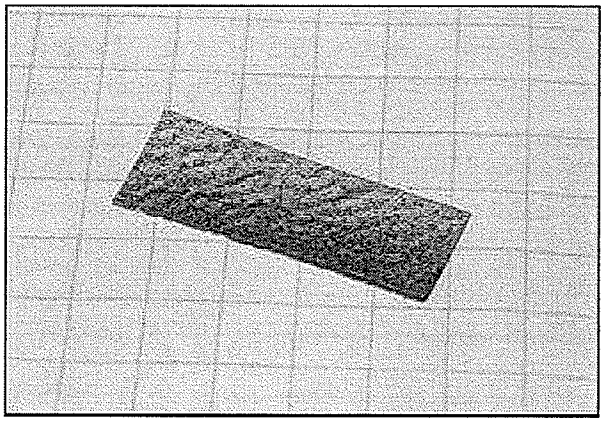

Figure 10: Inconel 625 micro-weld coating after dissolving the mild steel substrate

Since the applied coating was Inconel 625, a highly corrosion resistant alloy, it could not be progressively dissolved from the substrate according to the Davidenkov Method described in ref. [2]. Therefore, the mild steel substrate was dissolved away from the Inconel 625 micro-weld deposit and the approximate internal stresses were calculated from the deposit's curvature. From mechanics of materials [28], the stress distribution for a simply supported beam, is given by:

$$\sigma = \frac{Mc}{I} \qquad (1)$$

where σ = load over area

M = moment arm

I = moment of inertia

c = distance from the neutral axis to the top or bottom surface of the coating (location of maximum stress)

The formula for maximum deflection under a uniformly distributed load acting on a beam is:

$$y = -\frac{5\,w\,L^4}{384\,E\,I} \qquad (2)$$

where y is the measured deflection

w is the distributed load

L is the span over which curvature is measured

E is the modulus of elasticity (208 GPa for Inconel 625 at room temperature)

I is the moment of inertia of the beam

Re-arranging (2) gives:

$$w = -\frac{384\,y\,E\,I}{5\,L^4} \qquad (3)$$

The reaction force P shown in Figure 11 is calculated as follows:

$$P = \frac{w\,L}{2} \qquad (4)$$

From P, an equivalent bending moment M (counter clockwise) can be calculated at the location of maximum deflection (at the center of the etched removed coating).

$$M = \frac{P\,L}{2} - \frac{w\,L^2}{8} = \frac{w\,L^2}{4} - \frac{w\,L^2}{8} = \frac{w\,L^2}{8} \qquad (5)$$

Substituting (5) into (1) gives the internal stress in the beam.

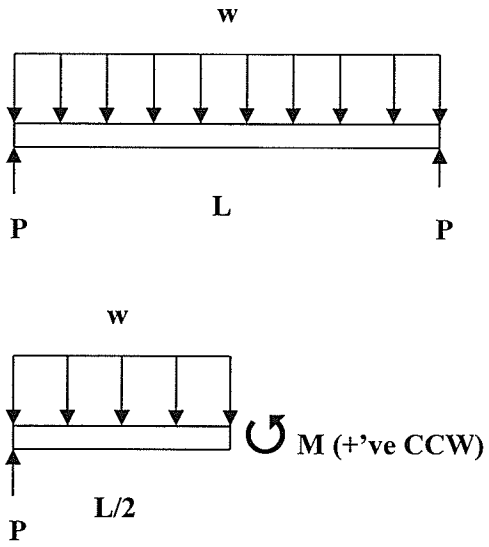

Figure 11: Determination of equivalent bending moment at mid-span for a simply supported beam under a uniform load

4.6 METALLOGRAPHIC EXAMINATIONS

Initial sectioning of uncoated specimens was carried out using a Buehler abrasive wheel cutter. Coated specimens were sectioned using a wire feed spark machine. Refer to Figure 12 for a diagram showing the location of sections taken from micro-welded coated specimens.

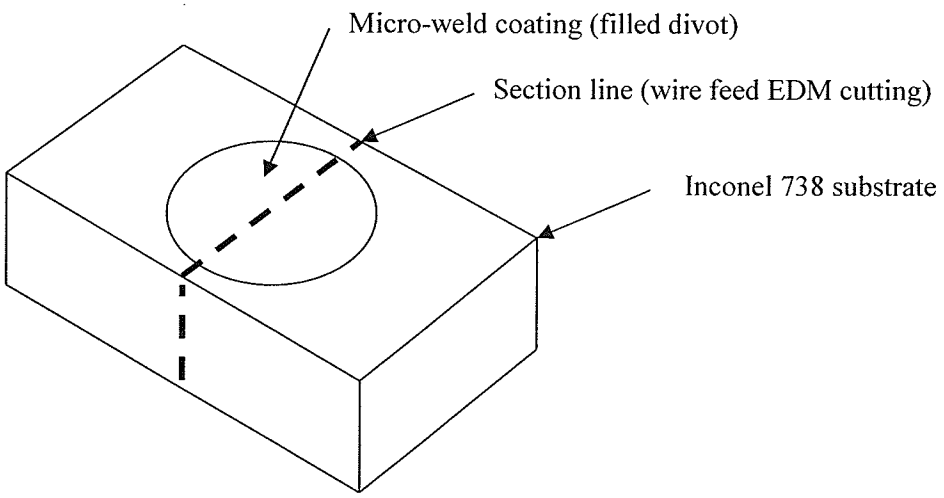

Figure 12: Sketch showing sectioning of micro-welded coated specimens

Design of experiment specimens were hot-mounted on the sectioned face in Bakelite resin using a Buehler Metaserv mounting press. A pressure of 50 psi with a heating time of 15 minutes and a cooling time of 5 minutes were used for all mounts. Oxidation test specimens were cold mounted on a randomly selected face using a two-part epoxy resin. This provided excellent edge retention for subsequent high magnification examinations.

Grinding was carried out with silicon carbide abrasive paper on a Buehler grinding table. The following silicon carbide abrasive grits were sequentially used: 120, 180, 240, 320, 400 and 600.

Polishing was carried out on nylon fabric covered rotating polishing wheels with 6 micron followed by 1 micron diamond abrasive pastes. Manual final polishing was on a cloth pad with alumina in suspension with water.

Between grinding and polishing steps, the specimens were cleaned with cold soapy water followed by drying using filtered compressed air. The final cleaning step consisted of immersion in distilled water with ultrasonic vibratory cleaning. The specimens were air dried prior to subsequent metallographic examinations or etch treatment.

To reveal the microstructure of the cast Inconel 738 base material and the micro-weld interface, Kalling's no.2 reagent was swabbed on the polished surface for 3 to 5 seconds followed by cold tap water and distilled water rinsing. This provided a clear view of the interface but exaggerated the relative size of voids and cracks by rounding off their edges. Therefore, quantitative measurements using a Zeiss microscope with Clemex image analysis software were conducted on specimens in the as-polished and unetched condition.

Since Kalling's no.2 reagent provided excellent results by swab etching, other etchants were not required.

4.7 INSTRUMENTATION

4.7.1 OPTICAL MICROSCOPY

A Zeiss optical microscope with Clemex image analysis software was used for low magnification metallographic examinations and measurements. The Zeiss microscope was equipped with a digital camera linked to Clemex image analysis software.

Using the Clemex software, measurement routines were written to measure the area fraction of voids and total crack length. In the field of view, the grey scale level in images was converted into distinct bitmap planes and assigned a color. The software then provided measurements for the features of interest differentiated by colors. Refer to Appendices A and B for Clemex routines.

Arial fraction void content measurements were taken at a magnification of 100X. This limited the maximum number of fields that could be measured on each specimen to six or seven, depending of the coating thickness. For each specimen, the measured area fractions of voids were added and the average was calculated.

The crack length measurements were taken at 200X magnification. The higher magnification permitted the detection of fine cracks in the coating. Up to ten random fields were taken on each specimen. The routine for these measurements was written such that long narrow cracks and voids were measured and the large, round voids considered to be porosity were excluded. Using the Clemex software, the total crack length for each field was measured and the

average crack density for each specimen was calculated in terms of total crack lentgth per area.

4.7.2 SCANNING ELECTRON MICROSCOPY

A JEOL JSM5900LV scanning electron microscope equipped with Oxford energy dispersive spectroscopy was used for high magnification metallographic examinations. The secondary electron imaging mode was used for all examinations. Specimens were viewed with an accelerating voltage ranging from 20 to 25kV while elemental line scans and maps were taken at 20 kV.

4.7.3 KNOOP HARDNESS TESTING

A Leitz Knoop hardness tester with a load of 300 poise was used for all hardness measurements. Prior to use, the hardness tester was verified for accuracy with N.I.S.T traceable reference blocks within the testing hardness range. Refer to Figure 13 for a photograph of the hardness testing machine. For each hardness determination, the average of three acceptable indentations was taken.

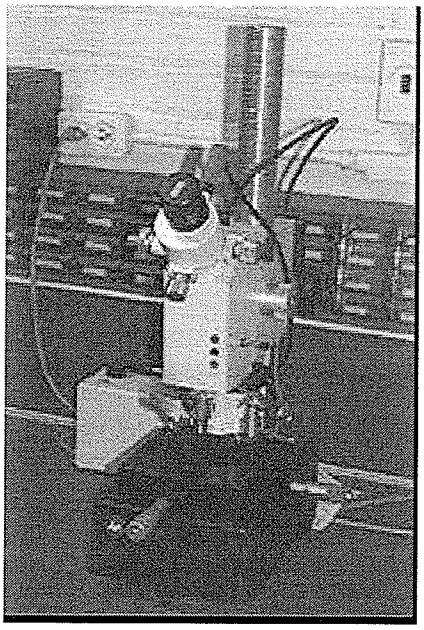

Figure 13: Leitz Knoop hardness tester

5. RESULTS AND DISCUSSIONS

5.1 MICROSTRUCTURE

Baseline Gas Tungsten Arc Welds

The baseline gas tungsten arc welded Inconel 738 in the as-cast form suffered from severe heat affected zone cracking. Cracks propagated along grain (dendrite) boundaries into the base material while the Inconel 625 filler remained crack free. Refer to Figure 14 for a scanning electron microscope image of weld cracks in the weld heat affected zone.

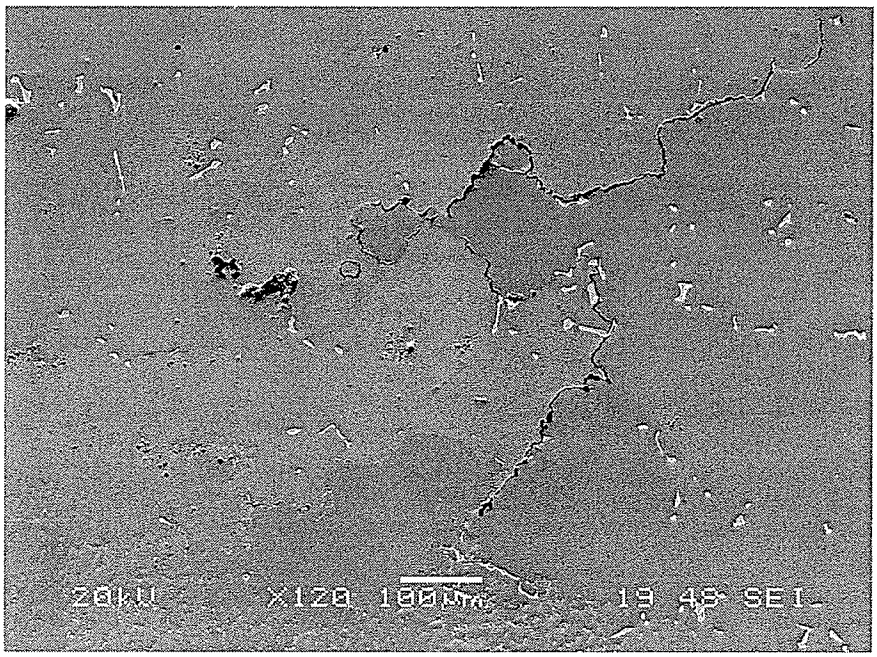

Figure 14: Cracks in the heat affected zone of as-cast Inconel 738 gas tungsten arc welded with Inconel 625 filler. Filler is visible at lower left edge of image.

In an attempt to minimize the extent of heat affected zone cracking, the Inconel 738 cast material was solution heat treated in a vacuum furnace (with vacuum better than 1×10^{-3} Torr) at 1120°C for 30 minutes followed by argon quenching. Prior to welding, the specimen was pre-heated for 10 to 20 seconds with the welding torch.

The weld zone of the solution treated + pre-heated specimen was free of cracks. As observed in the material welded in the as-cast condition, cracks were found to extend along grain boundaries in the weld heat affected zone. In general, the total length of cracks and depth of penetration were less than those observed in the as-cast specimen. The baseline trials were conducted to assess the susceptibility of Inconel 738 to heat affected zone cracking and actual crack lengths were not measured. Refer to Figure 15 for a scanning electron image of the solution treated + preheated specimen after welding. In this image, the severity of heat affected zone cracking appears to have decreased.

It is worth noting that liquid penetrant inspection, a common method of inspecting weld repairs would not detect the intergranular cracking beneath the filler alloy as it can only detect surface cracks. X-ray inspection would also fail to detect the cracks because of their predominant perpendicular orientation relative to the weld repair material's surface. For detection by x-ray inspection, cracks must traverse longitudinally in the material.

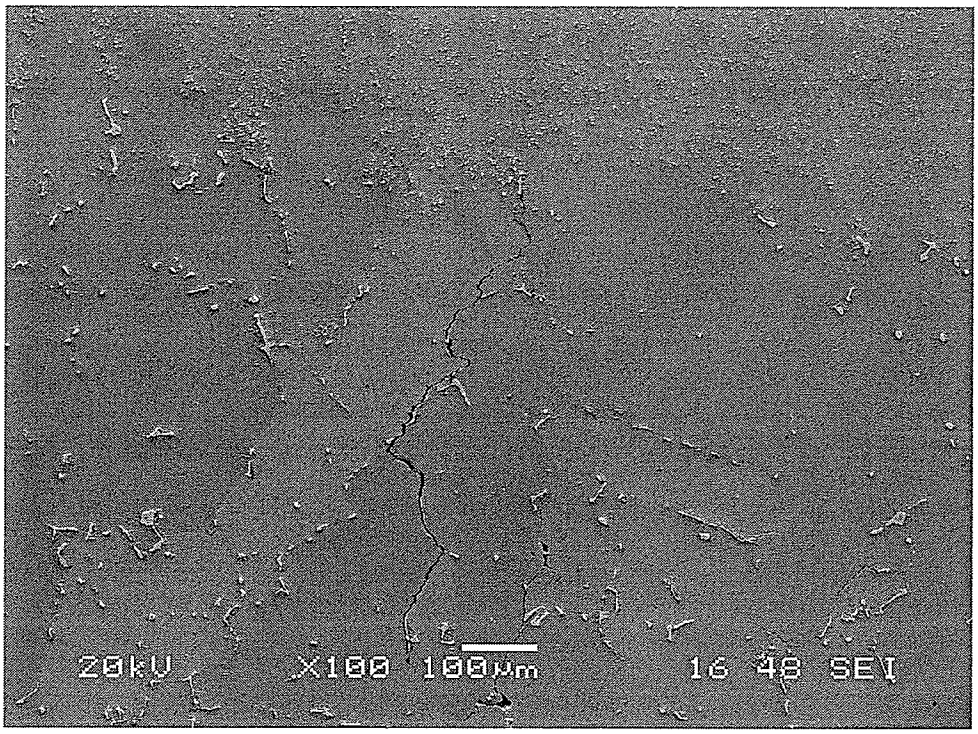

Figure 15: Gas tungsten arc weld of Inconel 738 in solution treated form with pre-heat using Inconel 625 filler. Filler is visible at top of image.

Metallography of Micro-Welds

When viewed with optical and scanning electron microscopy, the micro-welded coating microstructures were generally featureless. In the unetched condition, individual droplets, also referred to as splats when dealing with thermal spray coatings, were not visible in the majority of cases. A light swab etch of the polished surface with Kalling's no.2 reagent revealed some individual droplet deposits.

When examined in the etched condition, a preferred crystallographic orientation became apparent in the coatings. Fine columnar grains in the order of 3 to 5 μm in width were observed to be aligned perpendicular to the base material's surface. The predominant grain orientation is parallel to the axis of heat flow during the cooling phase of the micro-weld process and supports the findings of ref. [3]. In the coating microstructure, the individual grains appear to have been formed by several layers of deposits. Therefore, during the plasma transport mode, the deposited material would assume the crystallographic orientation of the base layer upon which solidification takes place. Refer to Figures 16 and 17 for photomicrographs showing the grain structure in the Inconel 625 micro-welded deposits.

As the process parameters were varied, the coatings showed varied amounts of porosity and cracking. Increasing the voltage and current increased the amount of porosity and cracks in the deposits. However, the cast Inconel 738 base material remained free of cracks and did not exhibit a heat affected zone for all parameters and alloy deposits examined in this study.

The deposit to base material interface generally exhibited good fusion and showed evidence of metallurgical bonding. Due to the high similarity in alloying constituents between the electrode alloys and the Inconel 738 substrate, EDS line scans could not accurately resolve re-alloying at the interface where metallurgical bonding and mixing occurred. As shown in Figure 18, the Inconel 738 deposit structure has interspersed micro-porosity with excellent fusion to the base material. Figure 19 is a photomicrograph of the typical Inconel 738 micro-welded microstructure using the highest power settings selected in this design of experiments. When compared to Figure 18, a drastic difference exists in the amount of porosity and cracking in the coatings. As the pulse arc power is increased, a gradual shift occurs from what was predominantly complete plasma transport mechanism to a combination of plasma,

droplet and contact transport mechanisms. A localized region with a lack of fusion was observed in one of the Inconel 738 center point specimens and is shown in Figure 20. This observation was anomalous but worth noting.

As current, voltage and capacitance were increased from their base values of 3A, 100V and 20μF, the amount of porosity and cracking were observed to increase for all alloys. In Figure 21, droplets in the coating are clearly visible and confirm the presence of this transport mechanism.

The Rene 41 deposit yielded interesting results. Specimens #5, 6, 7 and 8 had surface textures not yet seen on other specimens. Johnson describes in ref. [1] that at higher pulse energies, gross deposition begins to take place with the formation of a series of peaks on the surface. When subsequent passes are made, the electrode preferentially makes contact with the peaks and results in more material being deposited at these locations and results in a non-uniform deposit. Specimen #5 showed the worse coating produced as a series of parallel wavy ridges along the axis of electrode motion. Specimens #5, 6, 7 and 8 correspond to a pulse current of 5 Amps. As shown in Figures 22 and 23, the resulting coating structure is of low quality and shows high amounts of droplets along the edge of each ridge. In these specimens, the deposit microstructure ranged from excellent in the center of the ridges to very poor along the edges where droplet and contact transport mechanisms were predominant.

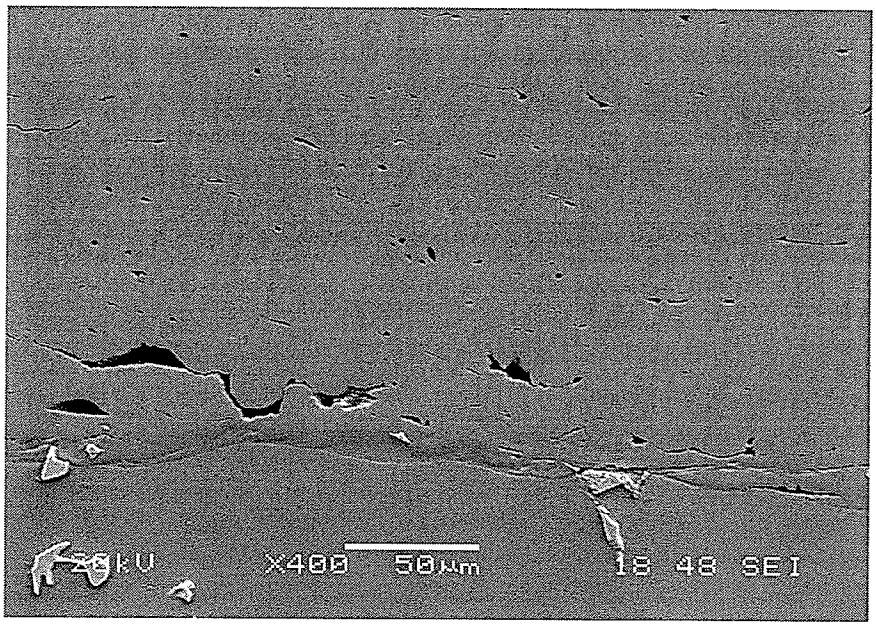

Figure 16: SEM image of Inconel 625 micro-welded deposit showing the fine and oriented grain structure (4A, 150V, 30µF), swab etched with Kalling's no.2 reagent.

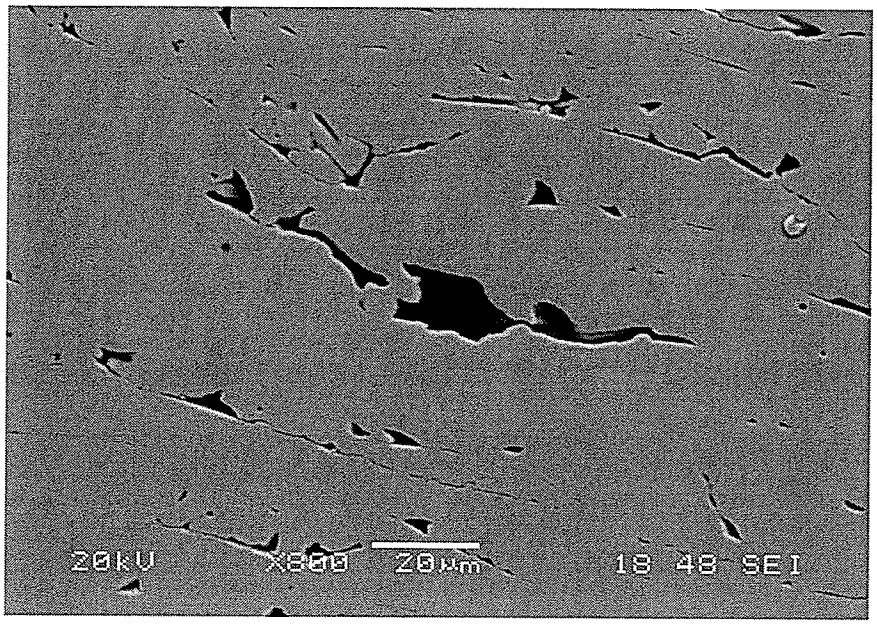

Figure 17: Higher magnification SEM image of Inconel 625 micro-welded deposit (4A, 150V, 30µF), swab etched with Kalling's no.2 reagent.

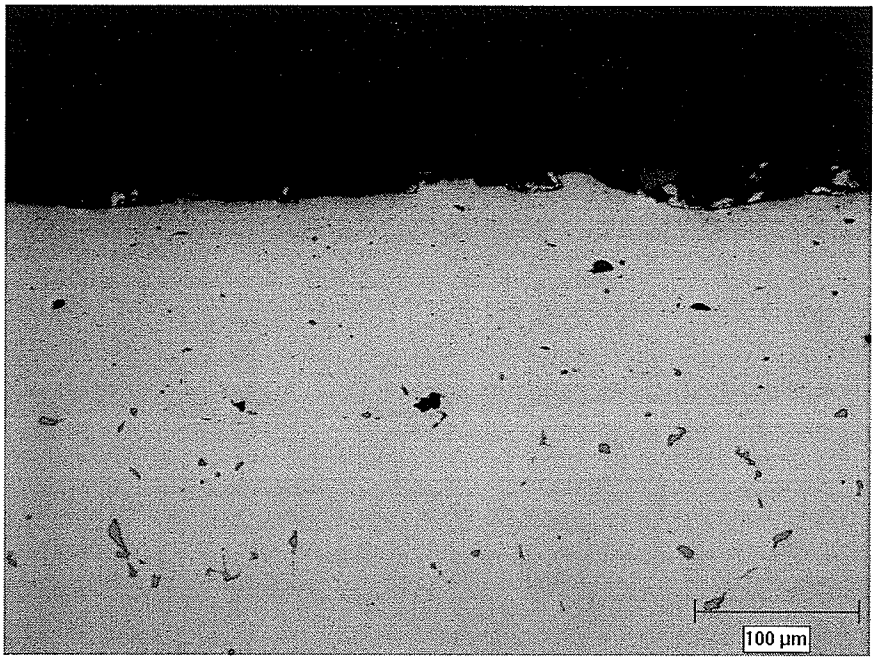

Figure 18: Inconel 738 micro-welded deposit microstructure exhibiting a plasma deposition mechanism (3A, 100V, 20µF), unetched condition.

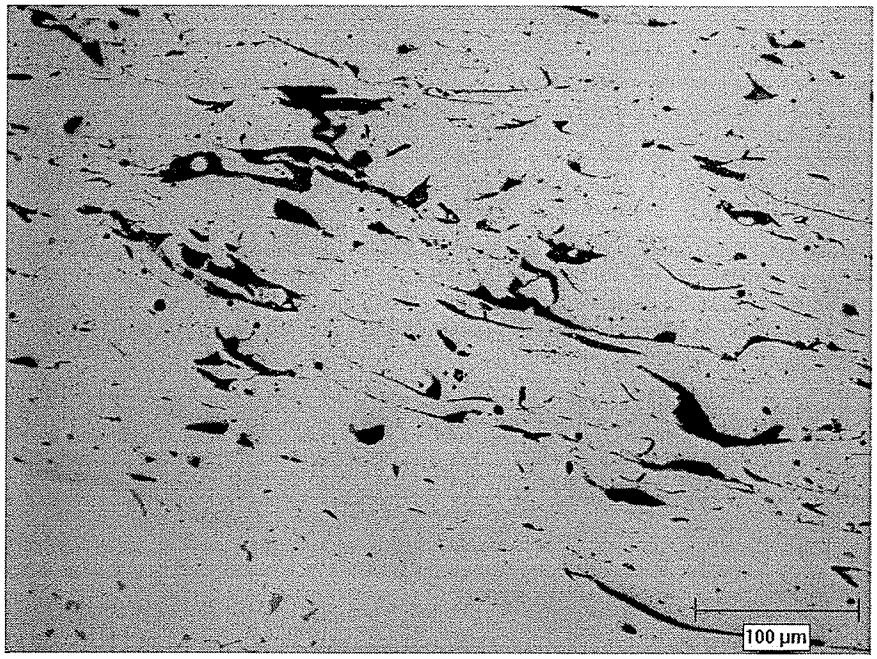

Figure 19: Inconel 738 micro-weld deposit microstructure displaying plasma, droplet and contact transfer mechanisms (5A, 200V, 50µF), unetched condition.

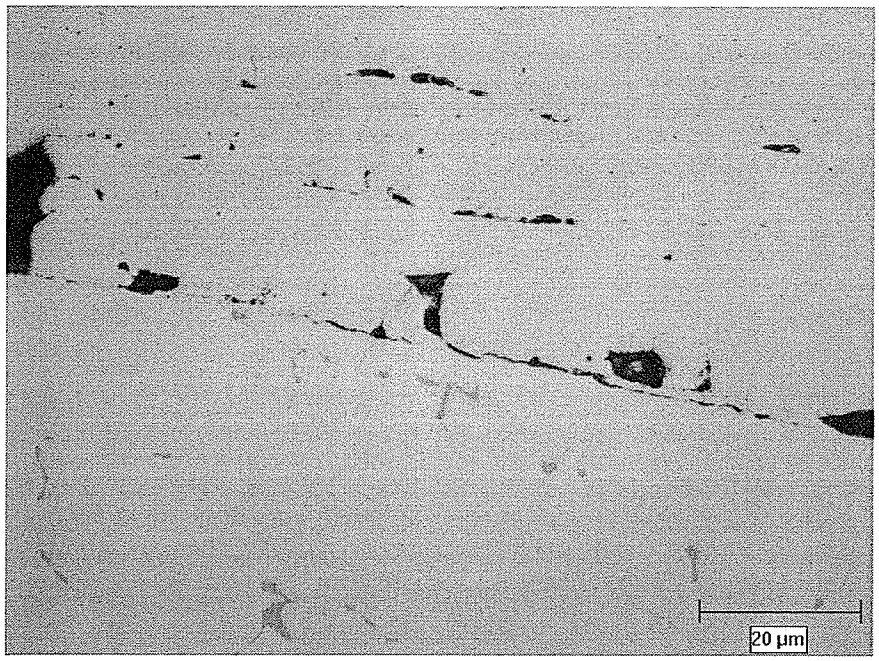

Figure 20: Interface lack of fusion in Inconel 738 micro-welded deposit (4A, 150V, 35µF), unetched condition.

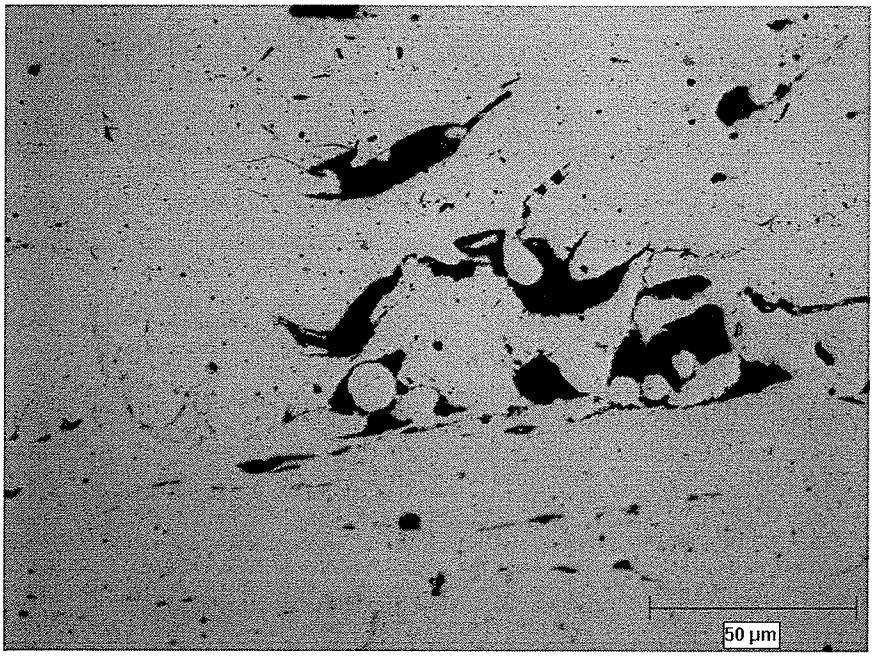

Figure 21: Cracks, porosity and droplets in Inconel 738 micro-welded deposit (20µF, 200V, 5A), unetched condition.

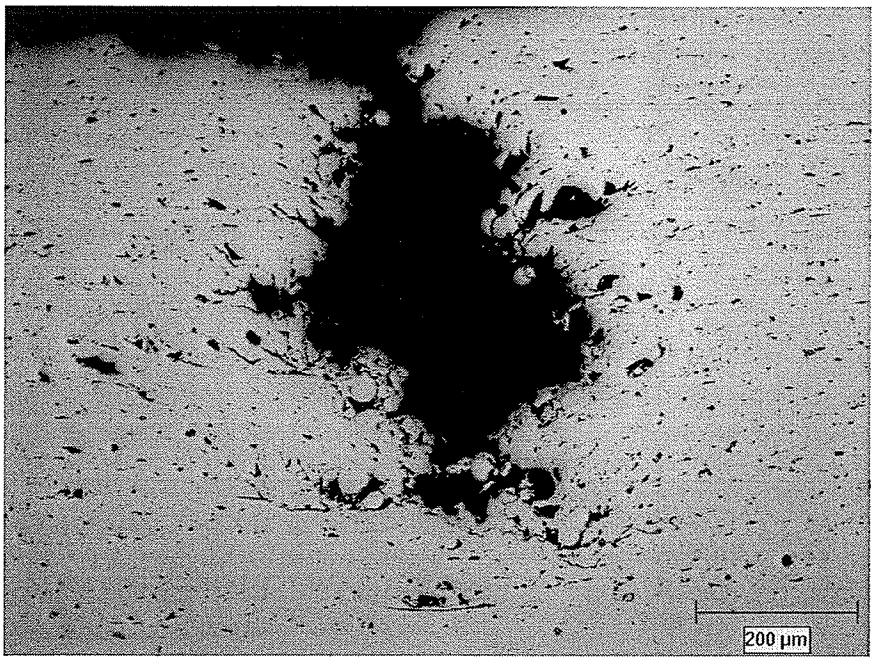

Figure 22: Rene 41 micro-welded deposit showing the structure of ridges and valleys (20µF, 100V, 5A), unetched condition.

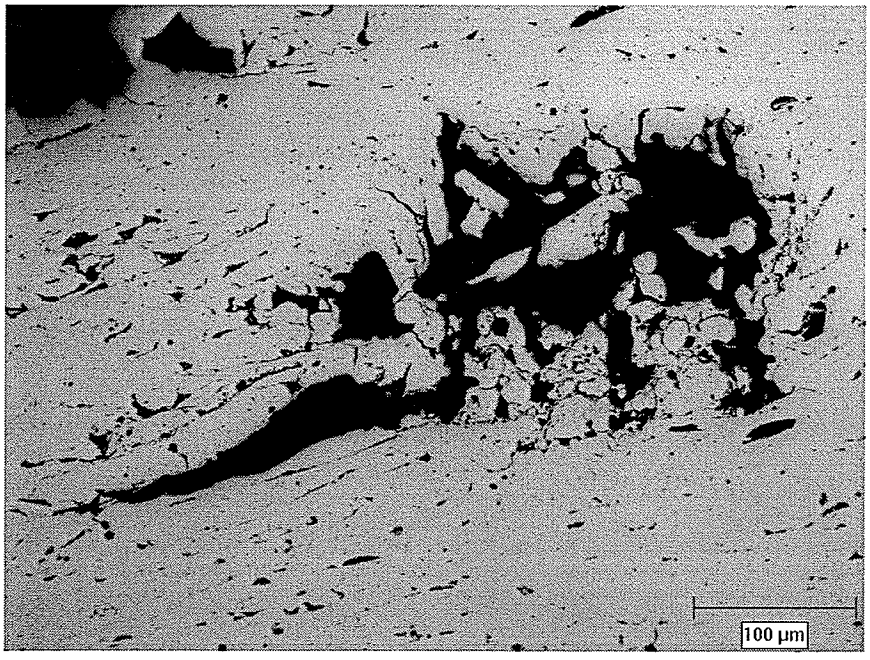

Figure 23: Droplets and internal void in Rene 41 micro-welded deposit (20µF, 100V, 5A), unetched condition.

5.2 DESIGN OF EXPERIMENTS

5.2.1 DOE RESULTS

Results for the design of experiments are listed in Tables 3, 4, 5, 6, 7 and 8 below.

Table 3: Inconel 625 Micro-Weld Deposit

Specimen Number	Capacitance (micro-Faradays)	Voltage (Volts)	Current (Amps)	Frequency (Hz) floating variable	Deposition Rate (grams/hr)	Void Content (Volume %)	Crack Density ($\mu m/\mu m^2$)
1	20	100	3	160	0.0671	1.7	0.00122
2	50	100	3	720	0.0690	2.3	0.00222
3	20	200	3	370	0.0612	2.1	0.00241
4	50	200	3	450	0.0304	2.1	0.00227
5	20	100	5	610	0.1872	1.9	0.00205
6	50	100	5	1100	0.1830	2.0	0.00287
7	20	200	5	450	0.1450	2.1	0.00265
8	50	200	5	310	0.1347	2.1	0.00314
9	*30*	*150*	*4*	610	0.0976	1.5	0.00342
10	*30*	*150*	*4*	260	0.1790	1.6	0.00314
11	*30*	*150*	*4*	450	0.1286	1.7	0.00364

Table 4: Inconel 718 Micro-Weld Deposit

Specimen Number	Capacitance (micro-Faradays)	Voltage (Volts)	Current (Amps)	Frequency (Hz) floating variable	Deposition Rate (grams/hr)	Void Content (Volume %)	Crack Density ($\mu m/\mu m^2$)
1	20	100	3	700	0.0563	6.0	0.00962
2	50	100	3	310	0.1346	2.6	0.00546
3	20	200	3	370	0.1700	2.4	0.00546
4	50	200	3	160	0.2595	2.3	0.00566
5	20	100	5	1120	0.1566	1.9	0.00658
6	50	100	5	500	0.4046	2.7	0.00696
7	20	200	5	610	0.5175	2.6	0.01287
8	50	200	5	260	0.5014	1.7	0.01057
9	*30*	*150*	*4*	460	0.3669	2.4	0.01408
10	*30*	*150*	*4*	460	0.3504	1.4	0.01419
11	*30*	*150*	*4*	460	0.3393	2.7	0.01305

Table 5: Inconel 722 Micro-Weld Deposit

Specimen Number	Capacitance (micro-Faradays)	Voltage (Volts)	Current (Amps)	Frequency (Hz) floating variable	Deposition Rate (grams/hr)	Void Content (Volume %)	Crack Density ($\mu m/\mu m^2$)
1	20	100	3	720	0.0942	3.1	0.00494
2	50	100	3	310	0.1706	3.9	0.00532
3	20	200	3	380	0.2811	5.0	0.00938
4	50	200	3	160	0.2548	3.8	0.00786
5	20	100	5	1120	0.1658	5.1	0.00824
6	50	100	5	510	0.2764	5.7	0.00253
7	20	200	5	590	0.6540	5.9	0.00219
8	50	200	5	270	0.6819	15.3	0.00958
9	*30*	*150*	*4*	450	0.3264	3.4	0.00538
10	*30*	*150*	*4*	450	0.2648	3.3	0.00675
11	*30*	*150*	*4*	450	0.2735	4.4	0.00843

Table 6: Inconel 738 Micro-Weld Deposit

Specimen Number	Capacitance (micro-Faradays)	Voltage (Volts)	Current (Amps)	Frequency (Hz) floating variable	Deposition Rate (grams/hr)	Void Content (Volume %)	Crack Density ($\mu m/\mu m^2$)	Knoop Micro-Hardness (300p)
1	20	100	3	740	0.0479	1.0	0.00189	436
2	50	100	3	320	0.1151	1.0	0.00195	455
3	20	200	3	390	0.2216	1.8	0.00494	451
4	50	200	3	160	0.3068	1.3	0.00329	407
5	20	100	5	1120	0.2529	4.7	0.00582	422
6	50	100	5	500	0.3457	4.8	0.00568	406
7	20	200	5	620	0.5231	4.0	0.00612	410
8	50	200	5	270	0.8554	4.0	0.01610	413
9	*30*	*150*	*4*	470	0.4462	3.8	0.00671	427
10	*30*	*150*	*4*	470	0.3254	6.0	0.00386	
11	*30*	*150*	*4*	470	0.3893	4.4	0.00639	

Table 7: Rene 41 Micro-Weld Deposit

Specimen Number	Capacitance (micro-Faradays)	Voltage (Volts)	Current (Amps)	Frequency (Hz) floating variable	Deposition Rate (grams/hr)	Void Content (Volume %)	Crack Density ($\mu m/\mu m^2$)
1	20	100	3	730	0.0063	0.0	0.00995
2	50	100	3	320	0.0450	1.0	0.00426
3	20	200	3	390	0.1452	1.8	0.00594
4	50	200	3	160	0.3931	1.3	0.00879
5	20	100	5	1130	0.2605	4.7	0.00716
6	50	100	5	500	0.2699	4.8	0.00758
7	20	200	5	610	0.4965	4.0	0.00832
8	50	200	5	260	0.4267	4.1	0.00795
9	*30*	*150*	*4*	460	0.1943	3.8	0.00665
10	*30*	*150*	*4*	460	0.3007	5.6	0.00896
11	*30*	*150*	*4*	460	0.0952	4.4	0.00770

Table 8: Nimonic 105 Micro-Weld Deposit

Specimen Number	Capacitance (micro-Faradays)	Voltage (Volts)	Current (Amps)	Frequency (Hz) floating variable	Deposition Rate (grams/hr)	Void Content (Volume %)	Crack Density ($\mu m/\mu m^2$)
1	20	100	3	730	0.0650	1.5	0.00402
2	50	100	3	320	0.1114	1.8	0.00408
3	20	200	3	380	0.2310	2.0	0.00653
4	50	200	3	160	0.2713	1.6	0.00492
5	20	100	5	1150	0.1688	1.3	0.00322
6	50	100	5	510	0.2488	1.6	0.00498
7	20	200	5	620	0.3936	2.8	0.00847
8	50	200	5	270	0.5271	4.4	0.00891
9	*30*	*150*	*4*	460	0.2491	2.5	0.00668
10	*30*	*150*	*4*	460	0.4125	3.3	0.00761
11	*30*	*150*	*4*	460	0.3872	2.7	0.00734

5.2.2 STATISTICAL ANALYSIS

Initially, the results for deposition rates, void content and crack density were analyzed to determine which terms had a significant effect on the response. Using a threshold p-value of 0.1, significant terms were identified. Similarly, the p-values for main effects, two-way interactions, three-way interactions and curvature were evaluated for their effect on each response. As a reference, the percentage of contribution to variation by the main effects, two-way interactions, three-way interactions and curvature was also calculated. Expressed as a percentage, the contribution to variation provided a practical value in addition to p-values calculated by the software.

The terms considered were capacitance, voltage, current, capacitance*voltage, capacitance*current, voltage*current and capacitance*voltage*current. In the analysis, terms were not considered to have a significant effect on the response if they had a p-value greater than 0.1. A p-value of 0.1 or less for the main effects, two-way interactions and three-way interactions was considered to indicate a significant effect on the response. A p-value less than 0.1 for the curvature was considered to have a significant contribution to variation and cannot provide an accurate process model. In such cases where the curvature p-value exceeds the selected threshold, it is an indication that the design of experiments must be repeated with a narrower range of parameters. The new range of parameters must be selected over an interval over which the process will behave in a near linear fashion, otherwise the p-value for curvature will remain above the threshold.

Refer to Appendices C, D, E and F for complete statistical results.

INCONEL 625 DEPOSITS

Deposition Rate

The analysis showed that the main effects accounted for 82.3% of the observed variation on deposition rate. The two-way and three-way interactions had no significant contributions to the variation but the curvature accounted for 4.7%. Of the main effects, only the current had a significant effect on deposition rate with a p-value of 0.068.

The general model for deposition rate was:

Deposition Rate (grams/hour) = -0.217 + 0.00279*CAPACITANCE + 0.000969*VOLTAGE + 0.0891*CURRENT -2.42E-5*CAPACITANCE*VOLTAGE – 0.000545*CAPACITANCE*CURRENT – 0.000270*VOLTAGE*CURRENT + 0.00000443*CAPACITANCE*VOLTAGE*CURRENT

with a reduced model for significant terms with p-values less than 0.1:

Deposition Rate (grams/hour) = -0.0945 + 0.0528*CURRENT

Void Content

The combination of main effects, two-way and three-way interactions only accounted for 33.0% while curvature accounted for 63.6% of the variation (with a p-value of 0.023 for curvature). Therefore, an accurate process model for the effect of process parameters on void content could not be generated.

Crack Density

Although the p-values for capacitance, voltage and current were 0.092, 0.097 and 0.067 respectively, the main effects only accounted for 40.5% of the measured variation on crack density. Curvature in the data accounted for 48.9% of the variation with a p-value of 0.025 and an accurate model for crack density could not be generated.

INCONEL 718 DEPOSITS

Deposition Rate

For this deposit, the main effects accounted for 84.0% of the observed variation while the two-way and three-way interactions accounted for 6.2 and 4.1% of the variation in the results. The voltage and current terms had significant effects on the deposition rate. An accurate model cannot be generated because the curvature in the results had a p-value of 0.015 and accounted for 5.6% of the variation.

Void Content

The main effects only accounted for 43.1% of the observed variation in void content. The two-way interactions, three-way interactions and curvature accounted for 23.4, 21.6 and 5.6% of the variation, respectively. None of the terms had a significant effect on void content as none of their p-values were below 0.10. Therefore, although curvature has a p-value of 0.318, a process model could not be generated due to the low effect of the terms on the void content.

Crack Density

The main effects accounted for 17.8% of the observed variation while the two-way and three-way interaction accounted for 19.1 and 4.8%, respectively. None of the terms had a significant effect on crack density as none of their p-values were below 0.10. With a p-value

of 0.005, the curvature in the results accounted for 57.7% of the variation. Therefore, an accurate model for crack density could not be generated.

INCONEL 722 DEPOSITS

Deposition Rate

The main effects accounted for 83.4% of the observed variation in results while the two-way and three-way interactions accounted for 15.3 and 0.014%, respectively. The voltage, current and voltage*current terms had significant effects on the deposition rate of this deposit. With a p-value of 0.270, the curvature only accounted for 0.7% of the variation in the results. The general process model for deposition rate is:

Deposition Rate (g/hour) = 0.147 + 0.00526*CAPACITANCE – 0.00177*VOLTAGE – 0.120*CURRENT – 4.42E-5*CAPACITANCE*VOLTAGE + 0.000237*CAPACITANCE*CURRENT + 0.00144*VOLTAGE*CURRRENT + 0.00000333*CAPACITANCE*VOLTAGE*CURRENT

with a reduced model for significant terms with p-values less than 0.1:

Deposition Rate (g/hour) = 0.321 - 0.00331*VOLTAGE – 0.111*CURRENT + 0.00156*VOLTAGE*CURRENT

Void Content

Main effects accounted for 53.3% of the observed variation in results for void content while the two-way and three-way interactions accounted for 24.2 and 12.3%, respectively. All terms (capacitance, voltage, current, capacitance*voltage, capacitance*current, voltage*current and capacitance*voltage*current) had significant effects on the void content in this deposit. With a p-value 0.031, the curvature accounted for 9.6% of the variation in the results and an accurate process model could not be generated.

Crack Density

Main effects accounted for 16.8% of the observed variation in results for crack density while the two-way and three-way interactions accounted for 32.1 and 42.8%, respectively. The curvature, with a p-value of 0.621 accounted for 1.2% of the variation in results. Of the terms, only capacitance*voltage*current had a significant effect on the crack density in this deposit and an accurate process model could not be generated.

INCONEL 738 DEPOSITS

Deposition Rate

The main effects accounted for 87.5% of the observed variation in deposition rate. The capacitance, voltage and current terms had significant effects with p-values below 0.10. With a p-value of 0.322, the curvature in the results accounted for 1.3% of the variation.

The general model for deposition rate is:

Deposition Rate (g/hour) = -0.517 + 0.0114*CAPACITANCE + 0.00238*VOLTAGE + 0.120*CURRENT – 0.000105*CAPACITANCE*VOLTAGE – 0.00326*CAPACITANCE*CURRENT – 0.000256*VOLTAGE*CURRRENT + 0.0000369*CAPACITANCE*VOLTAGE*CURRENT

with a reduced model for significant terms with p-values less than 0.1:

Deposition Rate (grams/hour) = -0.907 + 0.00481*CAPACITANCE + 0.00286*VOLTAGE + 0.161*CURRENT

Void Content

The main effects for void content accounted for 62.6% of the observed variation while the two-way interactions, three way interactions and curvature accounted for 3.0, 0.065 and 25.8%, respectively. With a p-value of 0.061, current was the only term with a value below 0.10. The general process model for void content is:

Void Content (Volume %) = -8.23 + 0.0317*CAPACITANCE + 0.0378*VOLTAGE + 2.7*CURRENT – 0.000367*CAPACITANCE*VOLTAGE – 0.00500*CAPACITANCE*CURRENT – 0.00883*VOLTAGE*CURRRENT + 0.0000667*CAPACITANCE*VOLTAGE*CURRENT

with a reduced model for significant terms with p-values less than 0.1:

Void Content (Volume %) = -2.85 + 1.55*CURRENT

Crack Density

The main effects for crack density accounted for 64.5% of the variation while the two-way interactions, three-way interaction and curvature accounted for 20.4, 11.8 and 0.007%, respectively. The voltage and current terms had, with p-values of 0.076 and 0.039, respectively had significant effects on the crack density. The general process model for crack density is:

Crack Density ($\mu m/\mu m^2$) = -0.0244 + 0.000660*CAPACITANCE + 0.000201*VOLTAGE + 0.00735*CURRENT – 6.48E-6*CAPACITANCE*VOLTAGE – 0.000200*CAPACITANCE*CURRENT – 5.32E-5*VOLTAGE*CURRRENT + 1.97E-6*CAPACITANCE*VOLTAGE*CURRENT

with a reduced model for significant terms with p-values less than 0.1:

Crack Density ($\mu m/\mu m^2$) = -0.0108 + 0.0000378*VOLTAGE + 0.00271*CURRENT

INCONEL 738 COATING MICROHARDNESS

The deposit hardness was measured and found to be dependent on process parameters. As the pulse power increased, the resulting deposit hardness decreased while the substrate hardness remained effectively unchanged. Although the deposit hardness was measured to decrease, no cracks were found in the base material microstructure. This confirms that the heat input to the base material is very small, even with high pulse powers. The moderately higher hardness values measured with low pulse energies were likely caused by the formation of a near-amorphous structure as a result of higher cooling rates achieved with less heat input. The electrode hardness was measured to be much higher than the base material, from which it was cast and subsequently swaged into a rod shape. The high cold-work that occurred in the swaging process was responsible for the increase in electrode hardness.

Using the Minitab software, a design of experiment analysis was carried out on the hardness results for the Inconel 738 micro-welded deposit. The main effects accounted for 56.4% of the measured variation on hardness, while two-way and three-way interactions accounted for 12.9 and 30.3%, respectively. The curvature accounted for only 0.3% of the observed variation. Therefore, since the main effects, two-way interactions and three way interaction all had p-values less than 0.1, a model can be written as follows:

HK = 230 + 8.58*CAPACITANCE + 1.80*VOLTAGE + 45.5*CURRENT – 0.0620*CAPACITANCE*VOLTAGE – 1.95*CAPACITANCE*CURRENT – 0.408*VOLTAGE*CURRENT + 0.0137*CAPACITANCE*VOLTAGE*CURRENT

As shown in the Main Effects plot in Appendix E, an increase in capacitance, voltage or current caused a decrease in coating hardness. Changing the current from the low value to the high value had the largest effect on reducing the coating hardness. Refer to Figures 24 and 25 for microhardness profiles on the lowest and highest pulse energy settings.

RENE 41 DEPOSITS

Deposition Rate

The main effects for the deposition rate accounted for 77.4% of the variation while the two-way interactions, three-way interactions and curvature accounted for 7.2, 4.1 and 3.0%, respectively. The voltage and current factors had significant effects on the deposition rate. The general model for deposition rate is:

Deposition Rate (grams/hour) = 0.00452 – 0.0186*CAPACITANCE – 0.00435*VOLTAGE – 0.00782*CURRENT + 0.000214*CAPACITANCE*VOLTAGE + 0.00432*CAPACITANCE*CURRENT + 0.00145*VOLTAGE*CURRRENT – 4.81E-5*CAPACITANCE*VOLTAGE*CURRENT

with a reduced model for significant terms with p-values less than 0.1:

Deposition Rate (g/hour) = -0.523 + 0.00220*VOLTAGE + 0.108*CURRENT

Void Content

Main effects for the void content accounted for 66.5% of the variation while the two-way and three-way interactions accounted for 5.3 and 0.8%, respectively. Current was the only term which had a significant effect on the void content in this deposit. With a p-value of 0.093, the curvature accounts for 21.6% of the variation in the results and an accurate process model for the void content could not be generated.

Crack Density

In this deposit, none of the terms had a significant effect (all p-values were greater than 0.10) on crack density. The main effects only accounted for 8.3% of the variation in results while the two-way and three-way interactions accounted for 35.5 and 44.5%, respectively. With a p-value of 0.758, the curvature only accounted for 0.7% of the variation. Since the most significant effect was obtained from the capacitance*voltage and capacitance*voltage*current terms, a process model could not be generated.

NIMONIC 105

Deposition Rate

The main effects for deposition rate accounted for 78.0% of the variation while the two-way and three-way interactions accounted for 3.2 and 0.2%, respectively. The curvature had a p-value of 0.243 and accounted for 10.7% of the variation. The voltage was the only terms that

had a significant effect on the deposition rate with a p-values of 0.079. The general model for deposition rate is:

Deposition Rate (grams/hour) = -0.230 + 0.00305*CAPACITANCE + 0.00141*VOLTAGE + 0.0312*CURRENT – 0.0000318*CAPACITANCE*VOLTAGE – 0.000433*CAPACITANCE*CURRENT + 0.0000953*VOLTAGE*CURRRENT + 0.00000993*CAPACITANCE*VOLTAGE*CURRENT

with a reduced model for significant terms with p-values less than 0.10:

Deposition Rate (grams/hour) = -0.0322 + 0.00207*VOLTAGE

Void Content

Main effects for void content accounted for 49.1% of the variation in results while the two-way and three-way interactions accounted for 28.9 and 5.7%, respectively. The curvature in the results, with a p-value of 0.129 accounted for 12.4% of the variation. Voltage had a p-value of 0.060 and was the only term to have a significant effect on the void content. A general process model for void content is:

Void Content (Volume %) = 0.133 + 0.133*CAPACITANCE + 0.0147*VOLTAGE + 0.0667*CURRENT – 0.00123*CAPACITANCE*VOLTAGE – 0.0333*CAPACITANCE*CURRENT – 0.00167*VOLTAGE*CURRRENT + 0.000333*CAPACITANCE*VOLTAGE*CURRENT

with a reduced model for significant terms with p-values less than 0.1:

Void Content (Volume %) = 0.593 + 0.0115*VOLTAGE

Crack Density

The main effects only accounted for 65.1% of the measured variation on crack density while two-way and three-way interactions accounted for 19.2 and 0.05%, respectively. The voltage, current and voltage*current terms had significant effects on the crack density in this deposit. Since curvature in the results accounted for 14.4% of the variation with a p-value of 0.040, an accurate model for crack density could not be generated.

Table 9: Process model coefficients for Deposition Rate

Model for deposition rate (grams/hour): $Y = A + B*CAPACITANCE + C*VOLTAGE + D*CURRENT - E*CAPACITANCE*VOLTAGE - F*CAPACITANCE*CURRENT - G*VOLTAGE*CURRRENT + H*CAPACITANCE*VOLTAGE*CURRENT$								
Alloy	**A**	**B**	**C**	**D**	**E**	**F**	**G**	**H**
IN625	-0.0945	-	-	0.0528	-	-	-	-
IN722	0.321	-	-0.00331	-0.111	-	-	0.00156	-
IN738	-0.907	0.00481	0.00286	0.161	-	-	-	-
R41	-0.523	-	0.00220	0.108	-	-	-	-
N105	-0.0322	-	0.00207	-	-	-	-	-
Process models could not be generated when p-values greater than 0.10 were obtained.								

Table 10: Process model coefficients for Void Content

Model for void content (% volume): **Y = A + B*CAPACITANCE + C*VOLTAGE + D*CURRENT – E*CAPACITANCE*VOLTAGE – F*CAPACITANCE*CURRENT – G*VOLTAGE*CURRRENT + H*CAPACITANCE*VOLTAGE*CURRENT**								
Alloy	**A**	**B**	**C**	**D**	**E**	**F**	**G**	**H**
IN738	-2.85	-	-	1.55	-	-	-	-
N105	0.593	-	0.0115	-	-	-	-	-
Process models could not be generated when p-values greater than 0.10 were obtained.								

Table 11: Process model for Crack Density

Model for crack density ($\mu m/\mu m^2$): **Y = A + B*CAPACITANCE + C*VOLTAGE + D*CURRENT – E*CAPACITANCE*VOLTAGE – F*CAPACITANCE*CURRENT – G*VOLTAGE*CURRRENT + H*CAPACITANCE*VOLTAGE*CURRENT**								
Alloy	**A**	**B**	**C**	**D**	**E**	**F**	**G**	**H**
IN738	-0.0108	-	3.78E-5	0.00271	-	-	-	-
Process models could not be generated when p-values greater than 0.10 were obtained.								

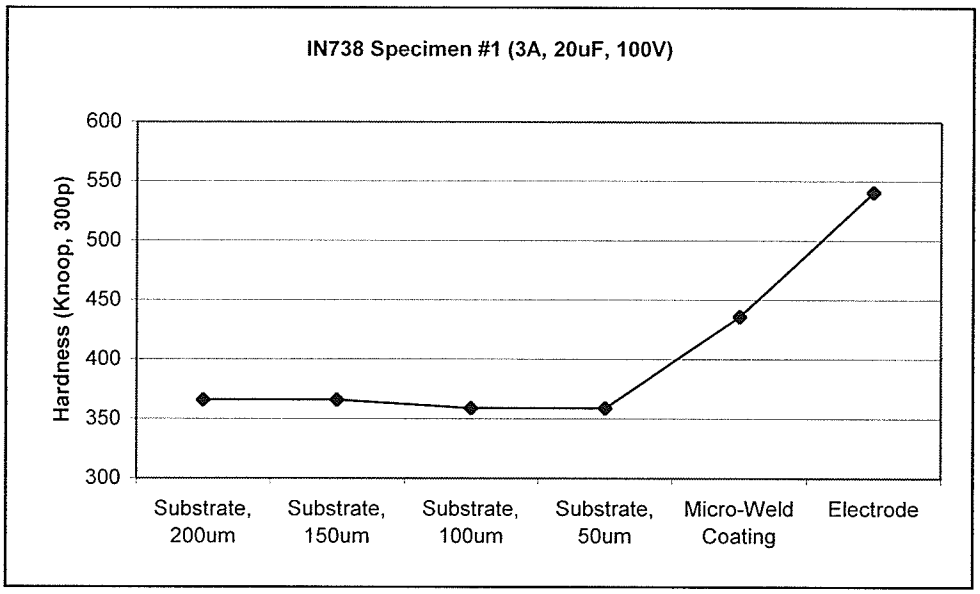

Figure 24: Knoop hardness measurements for the lowest pulse arc power setting (20 μF, 100 V, 3 A)

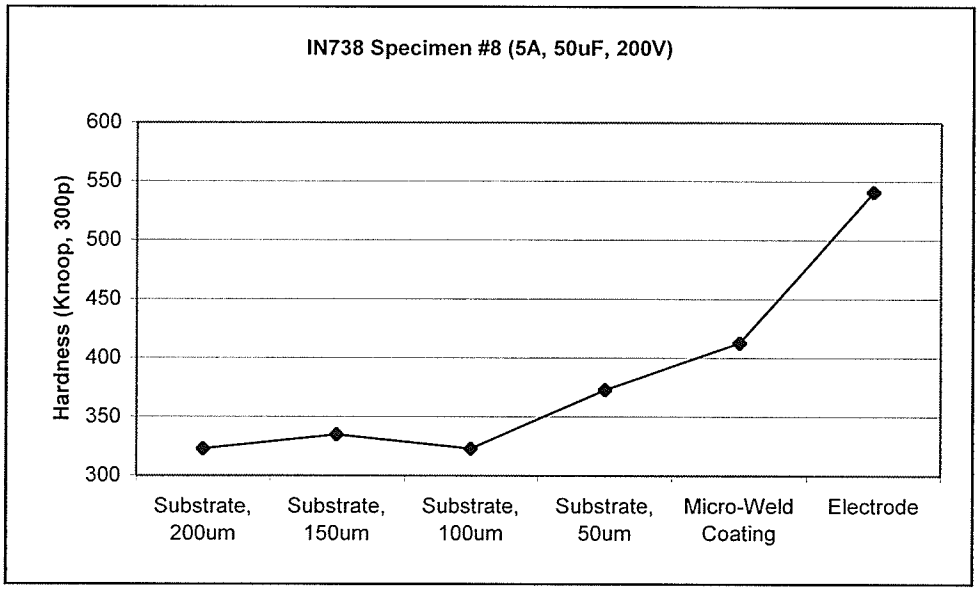

Figure 25: Knoop hardness measurements for the highest pulse arc power setting (50 μF, 200 V, 5 A)

5.2.3 DISCUSSION OF RESULTS FOR THE DESIGN OF EXPERIMENTS

As summarized in Tables 9, 10 and 11, the analysis for the factorial design of experiments showed that in general, voltage and current have the most significant effect on deposition rate, void content and crack density of micro-welded deposits. In nearly all cases, changing the capacitance did not have a significant effect on the response.

In several instances, the curvature in the result accounted for a significant portion of the variation as confirmed with p-values greater than 0.1. This indicates that the parameters selected in this design of experiments covered too broad of a range. For results free of curvature, a new design of experiments must be devised with a narrower range of parameters. A good approach would be to use a range half of that selected in this study. This would create eight designs of experiments (eight cubes) to fit inside the existing design. Although this would require a significant amount of effort, a more sophisticated statistical model could be established.

From the process models generated in this study, the following generalisations are made:

- For highest deposition rates, the voltage and current must be set to their maximum values (200V, 5A).
- For lowest void content and crack density, the voltage and current must be set to their minimum values (100V, 3A).
- Capacitance has little effect on the deposition rate, void content and crack density of micro-weld deposits.
- For harder coatings, the capacitance, voltage and current must be set to their minimum values (30μF, 100V, 3A).

Since the conditions for high deposition rate and low porosity and cracking cannot be satisfied simultaneously, the user must have a predetermined maximum amount of tolerable defects in the coating. Then, the process parameters that yield the highest deposition rate capable of maintaining the porosity and cracking within acceptable levels can be used. The process parameters were shown to have a significant effect on the microstructure of micro-welded deposits. With low voltage and current values, the deposits were relatively featureless and free of defects. This indicates that the plasma transport mechanism described in ref. [3] is predominant under these conditions. The absence of a distinct interface between the deposit and base material is confirmation that micro-weld deposits are metallurgically bonded to the base material. At high voltage and high current values, the deposits showed increased amounts of porosity, cracks and lack of fusion to the base material. In all but one model, capacitance was shown to have no significant effect on deposition rate, void content or crack density in the deposits.

Process parameters were also shown to have a significant effect on the deposit's hardness for Inconel 738. An increase in capacitance, voltage or current decreased the deposit's hardness. Low values for capacitance, voltage and current reduced the pulse power and heat input during the welding process. Therefore, with a reduced heat input, the solidification rate of the material being deposited increases. As described by R.N. Johnson in ref. [1], the high solidification rates associated with low pulse power settings can result in amorphous or near-amorphous deposits. In the present study, a fine columnar grain structure could be resolved for all deposits when viewed in the etched condition. Therefore, it is probable that only near-amorphous structures were obtained. Further studies must address the solidification rate of micro-weld deposits and quantify its effect on the resulting microstructure. Transmission electron microscopy and X-ray diffraction techniques could be used to study the presence of

crystalline and amorphous structures. A similar design of experiments could be conducted in order to establish a process model for the microstructural changes caused by process parameter selection.

An important observation in this study has been the absence of a heat affected zone and associated cracking in the cast Inconel 738 base material. As shown in references [10] and [11], gas tungsten arc welding of Inconel 738 results heat affected zone micro-fissuring caused by the high heat input during the welding process. However, micro-weld deposition rates are extremely low as compared to GTAW and may not be a cost effective alternative in certain applications. Future projects in this field should consider the modification of existing power supplies to increase the deposition rate with higher pulse energy settings. Other designs of experiments could be conducted to determine at which point, in terms of pulse energies, that micro-welding ceases to be a low heat input process and can be considered equivalent to arc welding. Being susceptible to heat affected zone cracking, Inconel 738 alloy would be an ideal candidate for such a project to develop the micro-welding process to repair gas turbine engine components.

Therefore, the micro-welding process is a viable alternative to GTAW processing for build-up of surfaces on cast Inconel 738. In instances where voids, cracks or lack-of-fusion must be kept to a minimum, the process voltage and current must be set to their low values of 100 Volts and 3 Amperes. Low values for capacitance, voltage and current are to be used to produce harder and wear resistant coatings.

5.3 OXIDATION

5.3.1 OXIDATION RATES

After the initial 4 hour exposure at 900°C (1650°F) in air, the specimens were removed from the furnace for visual examinations and mass gain measurements. The Inconel 722 specimen's surface was entirely covered by a dark grey scale and showed greater sign of oxidation than the other specimens. The bare Inconel 738 and coated Nimonic 105 specimens appeared to be least oxidized with slight green to grey discolorations. The mass gained per surface area was measured and correlated well with the visual assessment of relative oxidation rates.

A plot of mass gains per surface area for 168 hours exposure in air at 900°C is shown in Figure 26. A diffusion controlled parabolic oxidation rate was assumed and appears to be a good fit with the test data. Parabolic oxidation rate constants (K_p) were calculated using linear regression analysis. As shown in ref. [26], the expression for parabolic oxidation rates is:

$$(m/A)^2 = M^2 = K_p\, t$$

where m is the mass increase of the specimen (grams)

A is the area over which the oxidation reaction takes places (cm^2)

M is the mass gain per unit area ($grams/cm^2$)

K_p is the parabolic rate constant ($gram^2/cm^4 sec$)

t is the exposure time (seconds)

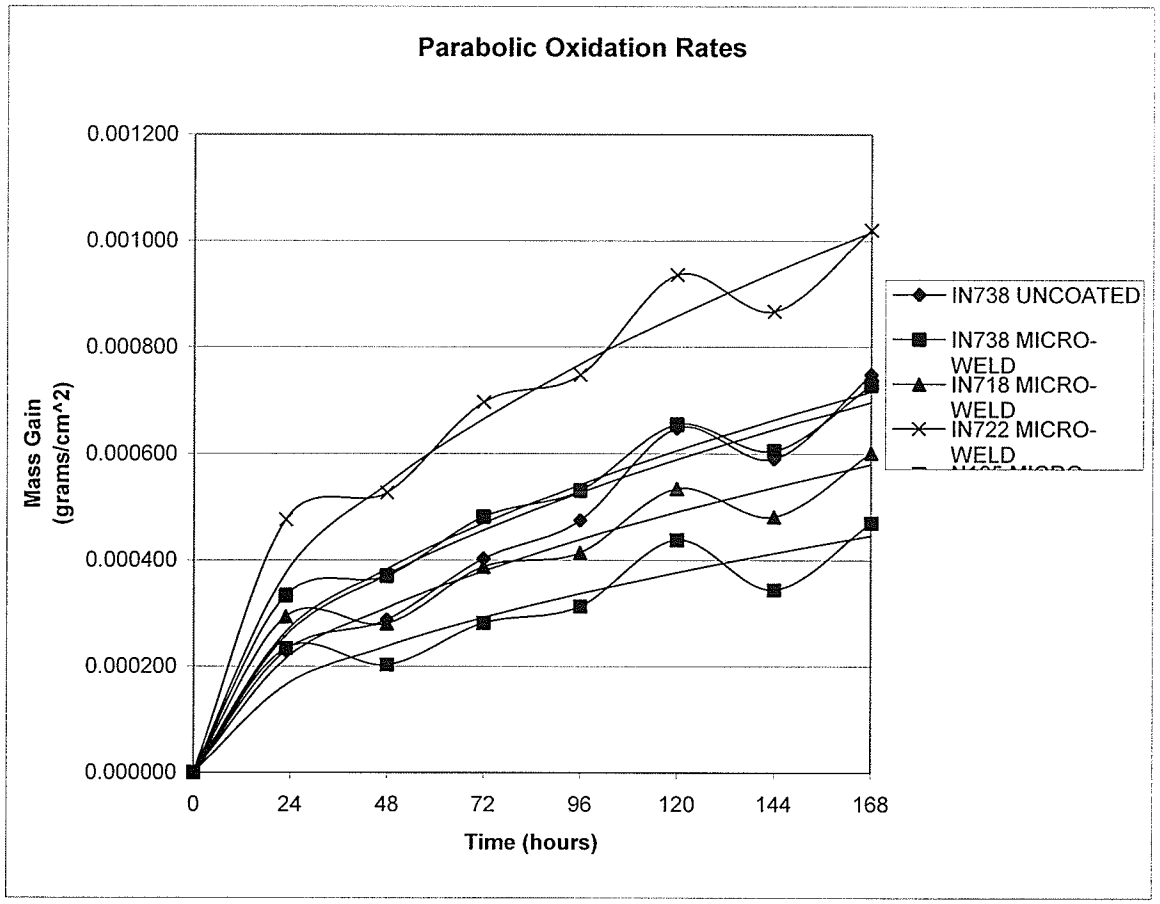

Figure 26: Oxidation rates of uncoated Inconel 738 and micro-welded Inconel 718, Inconel 722, Inconel 738 and Nimonic 105 deposits.

The calculated parabolic oxidation constants K_p, nominal aluminum + chromium concentrations and calculated mean coating thicknesses are listed in Table 12 below. Since the micro-weld coating thickness can only be measured in one plane after mounting for metallographic examination, an approximation of the mean coating thickness was obtained by taking the micro-weld coating mass, dividing it by the alloy's density and the specimen surface area.

The mean coating thickness was calculated as follows:

$$\text{Mean coating thickness} = m_2 - m_1 / (\rho_c A)$$

where m_2 is the specimen mass after coating

m_1 is the specimen mass prior to coating

ρ_c is the coating alloy's density

A is the coated specimen area (all surfaces)

Table 12: Parabolic Oxidation Rate Constants (K_p)

Specimen	K_p (g^2/cm^4sec)	$(K_p)^{1/2}$ ($g/cm^2sec^{1/2}$)	Aluminum + Chromium (nominal wt.%)	Calculated Mean Coating Thickness (μm)
IN722 micro-weld	1.71×10^{-12}	1.31×10^{-6}	16.2	3.7
IN738 micro-weld	8.51×10^{-13}	9.22×10^{-7}	19.4	6.4
IN738 uncoated	8.05×10^{-13}	8.97×10^{-7}	19.4	-
IN718 micro-weld	5.58×10^{-13}	7.45×10^{-7}	19.5	19.4
N105 micro-weld	3.30×10^{-13}	5.75×10^{-7}	19.5	10.5

As shown in Figure 27, the parabolic oxidation rate constant assumes an inversely proportional relationship with the nominal aluminum + chromium concentration. A regression analysis was carried out and the resulting significant relationship is:

$$K_p = -1.59 \times 10^{-7} \times (Al+Cr\%) + 3.88 \times 10^{-6} \qquad (R^2 = 0.734)$$

where R^2 is the percentage of variance explained by aluminium + chromium concentration (73.4%).

Figure 28 is a plot of K_p values as a function of mean coating thickness. A regression analysis was carried out and the relationship is:

$$K_p = -1.95 \times 10^{-8} \times (\text{thickness}) + 1.05 \times 10^{-6} \qquad (R^2 = 0.286)$$

In this case, the percentage of variance explained by the coating thickness is very low (28.6%) and is considered to have no significant effect on the parabolic rate constants K_p.

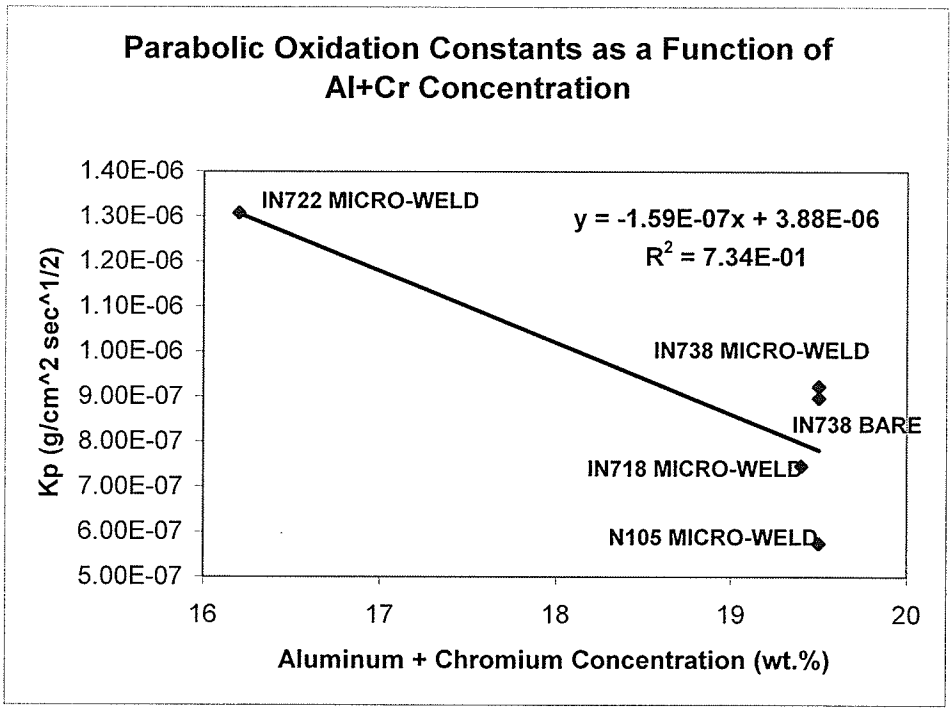

Figure 27: Parabolic oxidation constants as a function of aluminum + chromium concentration

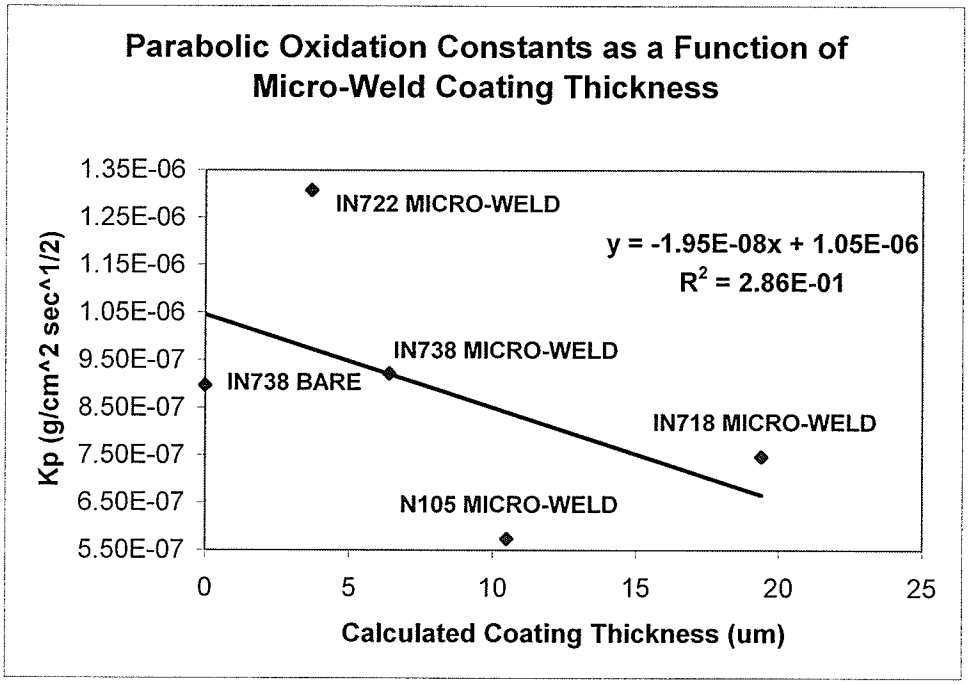

Figure 28: Parabolic oxidation constants as a function of coating thickness

5.3.2 OXIDE SCALE STRUCTURE

Using scanning electron microscopy with an accelerating voltage of 20kV, the oxide structures were observed to consist of a surface scale with internal precipitates extending in the base metal. Energy dispersive x-ray spectroscopy (EDS) in the elemental mapping and line scan modes was used to provide semi-quantitative analyses on the compositions of oxide scales, internal precipitates and the diffusion of alloying elements beneath the scale.

Oxygen was detected in high concentrations in the surface scales and internal precipitates. Aluminum, chromium, titanium and niobium were also found to be in significantly higher concentrations in the regions of high oxygen concentration. Therefore, assuming stochiometric compositions for the purpose of this discussion, it is concluded that Al_2O_3, Cr_2O_3, TiO_2 and Nb_2O_5 oxides were formed.

From the elemental map scan results, internal precipitates were determined to be Al_2O_3. Refer to Figure 29 for a typical elemental map scan showing the distribution of elements in the scales, the region below the scale and internal precipitates. The migration of aluminum, titanium and chromium is clearly visible along with a region of chromium and titanium depletion below the scale.

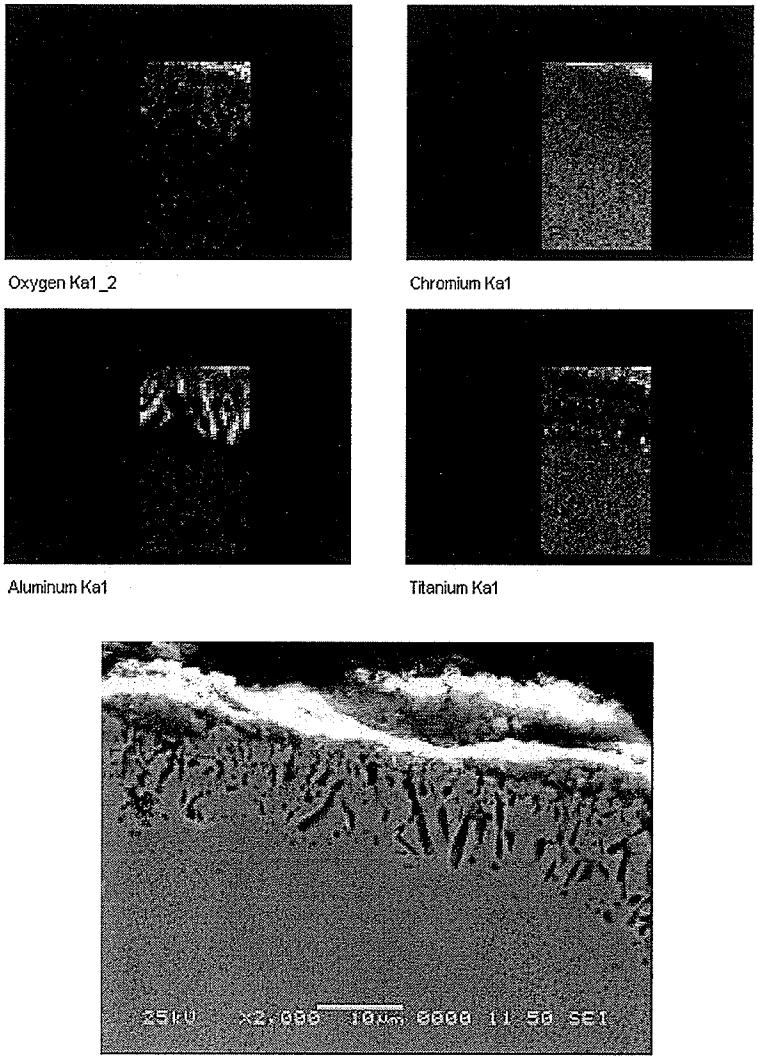

Figure 29: EDS elemental map scans for oxygen, chromium, aluminium and titanium in uncoated Inconel 738.

Other elements such as nickel, cobalt, iron, molybdenum, tungsten and niobium were not present in the surface scales. Refer to Figure 30, 31, 32, 33 and 34 for representative scanning electron microscope images and Appendix G for complete EDS elemental map and line scans.

Table 13 summarizes the thickness of surface oxide scales, depth of Al_2O_3 internal precipitates, the depth of chromium depletion measured from the metal/scale interface and structure of the scales that formed.

Table 13: Oxide scale thickness, penetration and depth of chromium depletion

	Inconel 738 Bare (μm)	Inconel 738 Deposit (μm)	Inconel 718 Deposit (μm)	Inconel 722 Deposit (μm)	Nimonic 105 Deposit (μm)
Scale Thickness	7	7	7	9	6
Depth of oxide penetration	11	9	9	11	7
Depth of chromium depletion	28	21	19	26	21
Scale Composition (from surface to metal)	Cr_2O_3, Al_2O_3 TiO_2	Cr_2O_3, Al_2O_3 TiO_2	Cr_2O_3 Nb_2O_5 Al_2O_3	Cr_2O_3, TiO_2 Al_2O_3	Cr_2O_3, TiO_2 Al_2O_3
Oxide Precipitates	Al_2O_3	Al_2O_3	Al_2O_3	Al_2O_3	Al_2O_3

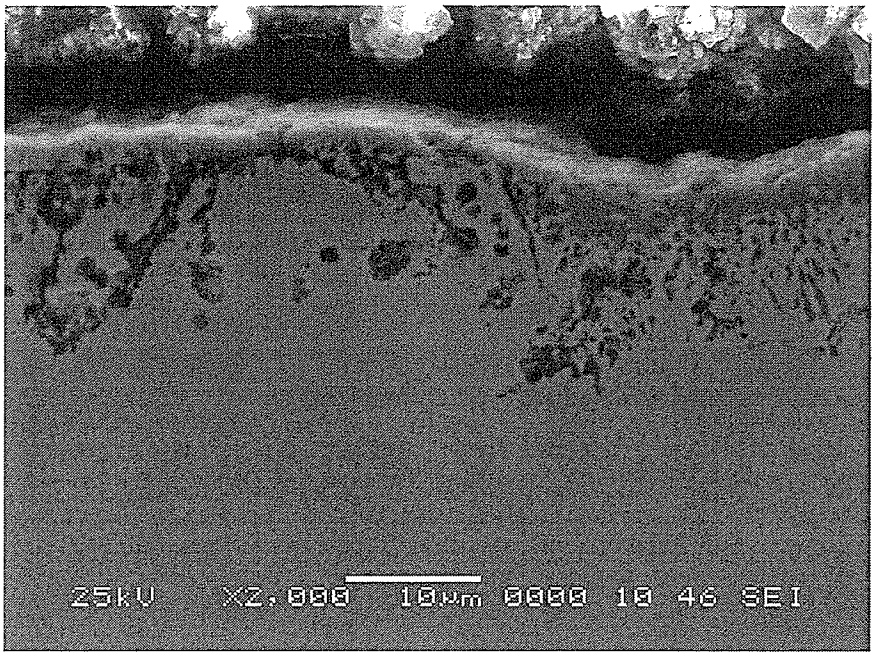

Figure 30: Oxidation of Inconel 722 micro-weld coating

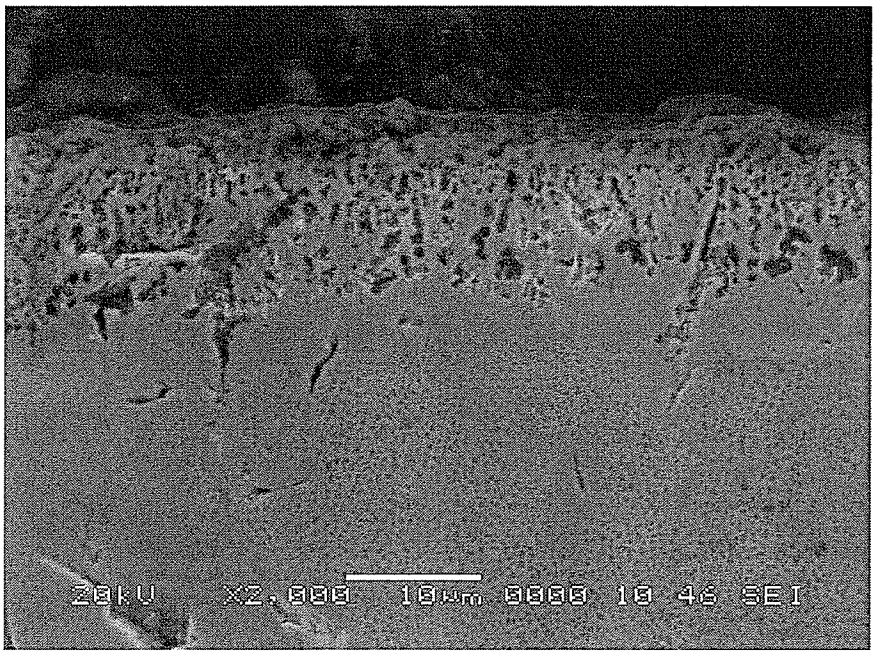

Figure 31: Oxidation of Inconel 738 micro-weld coating

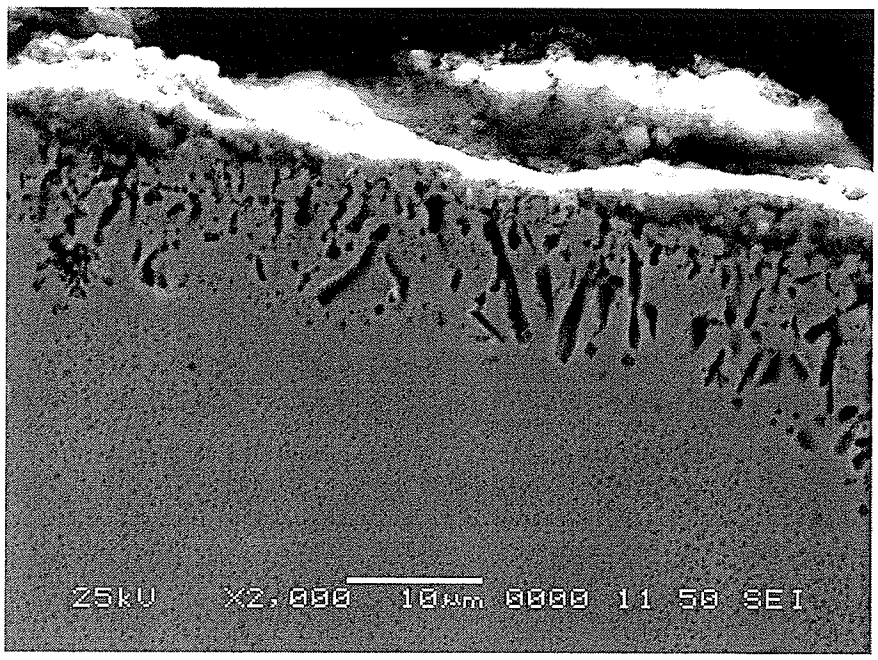

Figure 32: Oxidation of bare Inconel 738

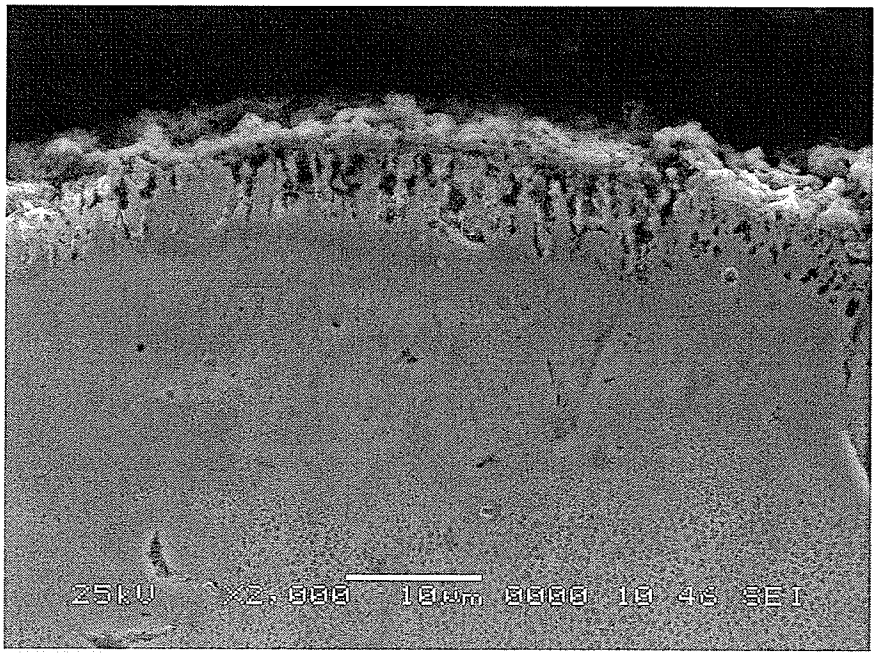

Figure 33: Oxidation of Inconel 718 micro-weld coating

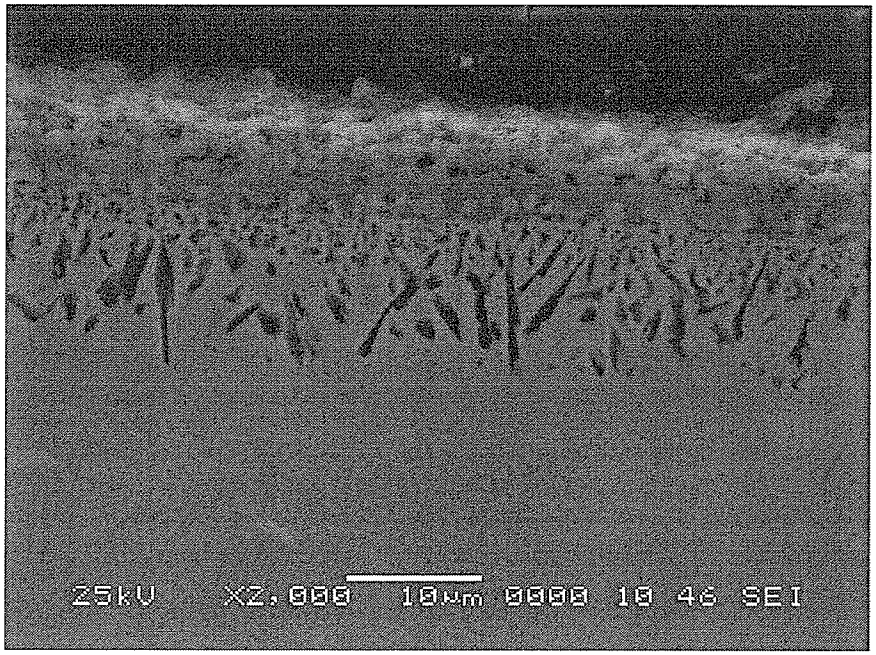

Figure 34: Oxidation of Nimonic 105 micro-weld coating

5.3.3 DISCUSSION ON OXIDATION RESULTS

OXIDATION RATES

As shown in Figure 26, the oxidation rates followed a parabolic relationship for all specimens. Initial oxidation rates were relatively high but gradually decreased to follows a parabolic rate. With this type of relationship, the growth of oxide scale is limited by the diffusion of cations (Ni, Al, Cr), anions (oxygen) and vacancies in the scale. As the scale thickness increases, the metal reactivity (at the metal scale interface) and ionic flux through the scale decrease and lead to a reduction in growth rate. Aluminium and chromium, being excellent protective scale formers are beneficial to oxidation resistance when present in sufficient amounts and have been shown to have an effect on scale thickness and growth rate.

In contrast to the results reported by Zhengwei et al [13], the oxidation rates of uncoated and micro-weld coated Inconel 738 were practically identical. The authors showed that the finer microstructure of micro-welded coatings led to the growth of thinner, finer grained, spallation resistant oxide scales and reduced the oxidation rate of Inconel 600 covered with pure aluminum. This indicates that at 900°C, the oxidation rate and spallation behaviour of Inconel 738 is not severe enough to provide insight on the performance of micro-weld coatings. Tests at 1000°C and 1100°C are required to draw further conclusions. It is also worth noting that Inconel 600 (Ni-15Cr-8Fe) is not as resistant to oxidation as Inconel 738 and may account to the marked improvement by coating with aluminum. The nominal aluminum content of 3.5 wt.% and 16 wt.% chromium in Inconel 738 account for the alloy's superior oxidation resistance over Inconel 600. Coating Inconel 600 with aluminum in ref. [13] formed an Al_2O_3 protective scale in addition to Cr_2O_3 and was similar to those found on uncoated and micro-welded Inconel 738 coatings in the present study. Therefore, it is anticipated that at higher oxidation temperatures, the self micro-welding of Inconel 738 will only lead to spallation resistance because the concentration of aluminum and chromium will remain unchanged.

As summarized in Table 12, Nimonic 105 with an aluminum + chromium concentration of 19.5 wt.% provided the best oxidation resistance with a K_p value of 3.30×10^{-13} g^2/cm^4sec. In contrast, the Inconel 722 coating with the lowest aluminum + chromium concentration (16.2 wt.%), had the lowest oxidation resistance with a K_p value of 1.71×10^{-12} g^2/cm^4sec.

In Figure 28, the R^2 value of 28.6% indicates that variations in coating thickness did not have a significant effect on oxidation rates. This further supports the prior assumption that the oxidation rate of micro-welded coatings is diffusion rate limited and parabolic in nature.

The oxidation rate of Inconel 718 was significantly lower than the values reported by Green et al in ref. [14]. The authors reported K_p values for Inconel 718 exposed to air at 900°C ranging from 2.67×10^{-12} to 6.29×10^{-12} mg^2/cm^4sec as compared to 5.58×10^{-13} mg^2/cm^4sec for the micro-welded Inconel 718 coating tested in this study. The difference in results may be due to factors such as air flow, oxygen replenishment in the furnace and specimen areas being different.

SCALE STRUCTURES

The alloys tested contained sufficient aluminum (0.5 to 4.7 wt.%) and chromium (14.8 to 19.0 wt.%) to form Al_2O_3 and Cr_2O_3 protective scales. As shown in Figure 27, the variations in aluminum + chromium concentration correlated with the change in parabolic oxidation constants between the alloys. Figure 35 is a plot showing the influence of composition on the oxidation behaviour in nickel-aluminum binary alloys. From this plot, it is shown that a minimum of 15 wt.% aluminum would be required to form an external Al_2O_3 oxide scale. A ternary alloy oxidation map shown in Figure 36 illustrates the combined effects of aluminum and chromium on the oxidation behaviour of Ni-Cr-Al ternary alloys for isothermal and cyclic environment. From this plot, it is shown that the alloys tested in this study fall in region II and possibly III for isothermal conditions and in regions I and T for cyclic conditions. Based on the semi-quantitative EDS results, the oxidation behaviour of alloys tested is in better agreement with isothermal conditions. This is reasonable since the specimens were only removed from the air furnace for mass measurements and were not subjected to repeated thermal shock.

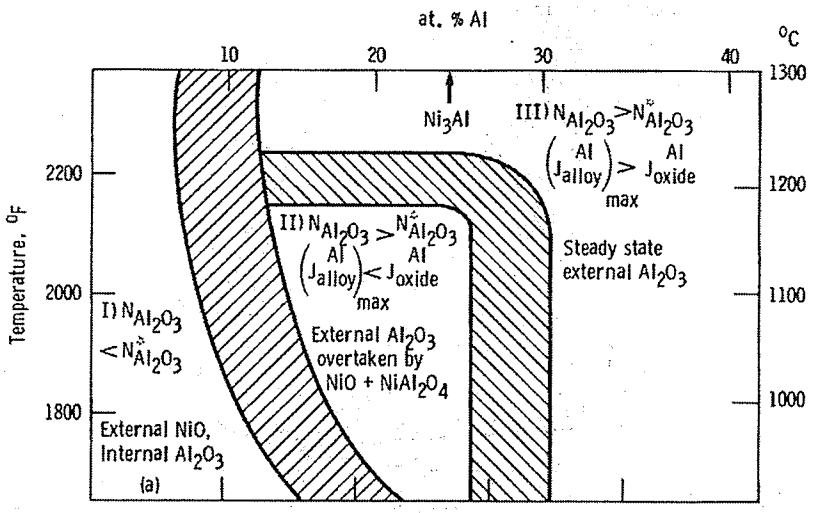

Figure 35: Effect of composition on the oxidation behaviour of binary Ni-Al alloys for 500 hours at 1100°C [27]

The diffusion controlled oxidation rate in Al_2O_3 is approximately two orders of magnitude less than Cr_2O_3 [27]. Therefore, the higher concentrations of aluminum + chromium in Inconel 738 (Al+Cr = 19.4 wt.%) and Nimonic 105 (Al+Cr = 19.5 wt.%) accounts for their lower oxidation rate than Inconel 722 (Al+Cr = 16.2 wt.%). Although Inconel 718 (Al+Cr = 19.5 wt.%) only contains a maximum of 0.4 wt.% aluminum, its oxidation resistance was superior to Inconel 738. This can be explained by the higher concentration of chromium in Inconel 718 (19 wt.%) along with small yet sufficient amounts of aluminum to form Al_2O_3 in the scale.

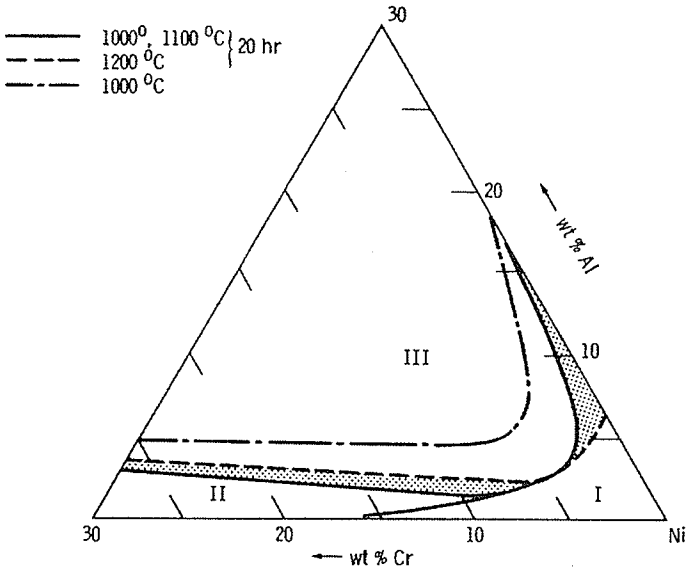

I External NiO, Internal $Cr_2O_3/Al_2O_3/Ni(Al, Cr)_2O_4$
II External Cr_2O_3, Internal Al_2O_3
III External Al_2O_3

(a) **Isothermal map.**

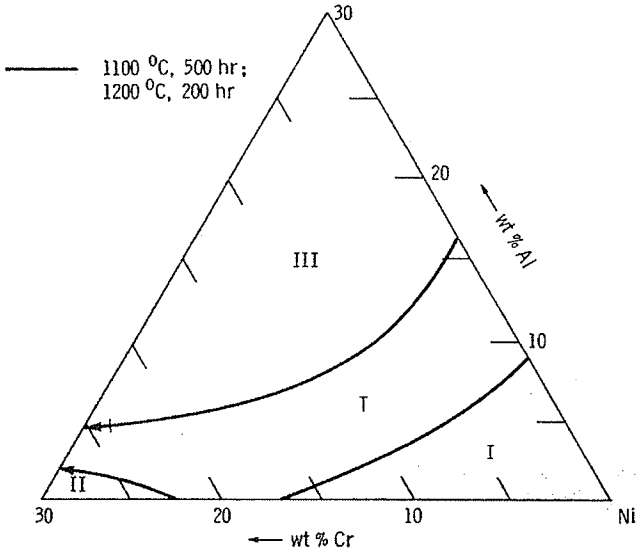

I Mostly NiO
II Mostly Cr_2O_3
III $Al_2O_3(+NiAl_2O_4)$
T NiO, $NiCr_2O_4$, $NiAl_2O_4$, Al_2O_3 Transition

(b) **Cyclic map.**

Figure 36: Effect of composition on the oxidation behaviour of ternary Ni-Cr-Al alloys [27]

As shown in ref. [26], the formation of oxide species can be explained by the second law of thermodynamics which is written in terms of the Gibbs free energy (G') as:

$$G' = H' - T\,S'$$

where H' is the enthalpy and S' is the entropy of the system.

The second law states that under these conditions:

$\Delta G' < 0$ reaction is spontaneous

$\Delta G' = 0$ equilibrium

$\Delta G' > 0$ no reaction occurs

For a chemical reaction such as oxidation of a metal, it is shown in that $\Delta G'$ is expressed as:

$$\Delta G' = \Delta G^{\theta} + R\,T \ln \left(\frac{a^{c}_{C}\ a^{d}_{D}}{a^{a}_{A}\ a^{b}_{B}} \right)$$

where ΔG^{θ} is the free energy change when all species are present in their standard states and a^{i}_{I} is the thermodynamic activity. The thermodynamic activity is a description of the deviation from the standard state of a species and is expressed as:

$$a_i = p_i / p_i^{\theta}$$

where p_i is the vapour pressure over a condensed species or the partial pressure of a gaseous species and p_i^{θ} is same corresponding to the standard state.

At equilibrium ($\Delta G' = 0$), the expression reduces to:

$$\Delta G^{\theta} = - R\,T \ln \left(\frac{a^{c}_{C}\ a^{d}_{D}}{a^{a}_{A}\ a^{b}_{B}} \right)$$

For a metal in reaction with oxygen ($M + O_2 \rightarrow MO_2$), the equilibrium oxygen partial pressure at equilibrium (where metal and oxide exist) is given as:

$$p_{O2}^{eq} = \frac{a_{MO2}}{a_M}\ p_{O2}^{M/MO2}$$

where the activities of M and MO_2 are unity.

As shown in Figure 37, at 900°C the Gibbs free energy of formation of Al_2O_3, Cr_2O_3 and NiO are -860, -540 and -280 kJ/mol O_2, respectively. The lower the position of an oxide species on the plot, the more stable it will be. The equilibrium oxygen partial pressure is determined by plotting a line from the point of origin in the upper left corner through the desired temperature on the species' line and extending it to the lower scale. Therefore at 900°C, the equilibrium partial pressure for Al_2O_3, Cr_2O_3 and NiO are 10^{-38}, 10^{-24} and 10^{-12} atm O_2, respectively. A shift in oxygen partial pressure greater than the equilibrium pressure will form oxides and a reduction in oxygen partial pressure below equilibrium will decompose the oxide. Refer to Table 14 for a summary of properties for selected oxides taken from ref. [20].

Table 14: Properties of selected oxides [20]

Oxide	Structure	Melting Point (°C)	Boiling or Decomposition Point (°C)	Molar Volume (cm^3)	Volume Ratio
α-Al_2O_3	D5 (corundum)	2015	2980	25.7	1.28
γ-Al_2O_3	(defect- spinel)	$\gamma \rightarrow \alpha$	-	26.1	1.31
Cr_2O_3	D5 (α-Al_2O_3)	2435	4415	29.2	2.02
NiO	B1 (NaCl)	1990	-	11.2	1.70
TiO_2	C4 (rutile)	1830	~2700	18.8	1.76
Nb_2O_5	Monoclinic	1460	2660	59.5	2.74
MoO_3	Orthohombic	795	1463	30.7	3.27

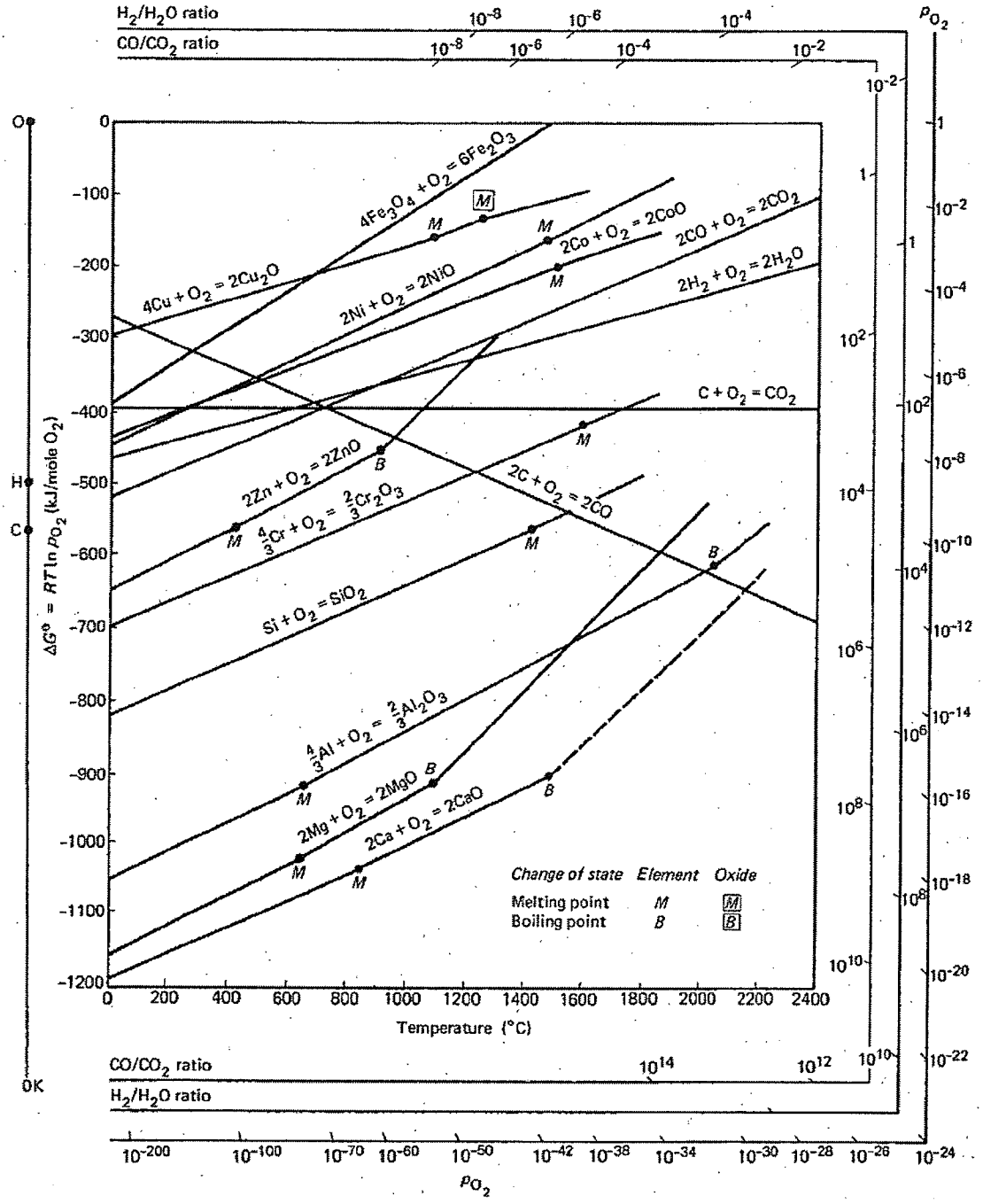

Figure 37: Standard free energy of formation for selected oxides as a function of temperature [26]

The presence of titanium in Inconel 738, Inconel 722 and Nimonic 105 was sufficient to form TiO_2 in the protective scale. Titanium tends to promote the formation of Cr_2O_3 but does not affect the growth rate and is not likely to have an effect on the formation of Al_2O_3 [27]. Refractory elements such as molybdenum, tungsten, tantalum and niobium can have different effects on the formation of Al_2O_3 and Cr_2O_3 protective scales. A beneficial effect is that they can act as getters and promote the formation of Al_2O_3 and Cr_2O_3 protective scales but they can also have deleterious effects. One such negative effect is decreasing the diffusion rates of aluminum and chromium in the base metal and works against the formation of Al_2O_3 and Cr_2O_3 protective scales. For the formation of scales, aluminum and chromium must diffuse from the base metal to the scale-base metal interface. Additionally, refractory elements form non-protective scales with low melting points and high vapour pressures. Although Nimonic 105 contains 5 wt.% molybdenum, its superior oxidation resistance can be attributed to the high aluminum (4.7 wt.%) and chromium (14.8 wt.%) concentrations. The higher concentration of chromium in Inconel 718 (19.0 wt.%) appears be to sufficient to offset the relatively low concentration of aluminum (0.5 wt.%) and high concentration of niobium + tantalum (5 wt.%).

DIFFUSION EFFECTS

The formation of diffusion controlled oxide scales is affected by the relative diffusion coefficients of alloying elements in the γ matrix. Assuming that the γ matrix is mainly nickel, the diffusion results for solute impurities in nickel listed by Burachynsky et al in ref. [17] can be used to explain the composition of protective scales.

From Leclaire's theory on impurity diffusion in metals [18], the difference in activation energy between solute and solvent self diffusion (ΔQ) is given by:

$$\Delta Q = \Delta H_2 + \Delta E = - \frac{\alpha Z_2 e^2 V_o e^{-(11qa/16)}}{11a/16}$$

where α is a parameter (~1 in value) dependent on Z

Z_2 is the excess charge of the solute impurity

e is the charge of an electron

V_o is the valence of the solvent

q is a calculated parameter related to the screening potential around the impurity atom

a is the jump distance between a solute or solvent atom and a vacancy

Niobium, with the lowest negative change in activation energy for solute impurity diffusion (ΔQ), formed a scale in the Inconel 718 coated specimen. The relatively high diffusivity of niobium combined with a high concentration in Inconel 718 support the results. Titanium, aluminum and chromium also have significantly large negative ΔQ values and were found to be present in the protective scales for all alloys with the exception of Inconel 718 where only Al_2O_3, Cr_2O_3 and Nb_2O_5 were present. Inconel 718 does not contain a sufficient amount of titanium to form a protective TiO_2 scale.

With positive ΔQ values, molybdenum, tantalum and tungsten are relatively slow diffusers in nickel and were not present in the oxide scales. Refer to Figure 38 for a plot of relative differences in activation energy for diffusion of solute impurities in nickel compiled by Burachynsky et al in ref. [17].

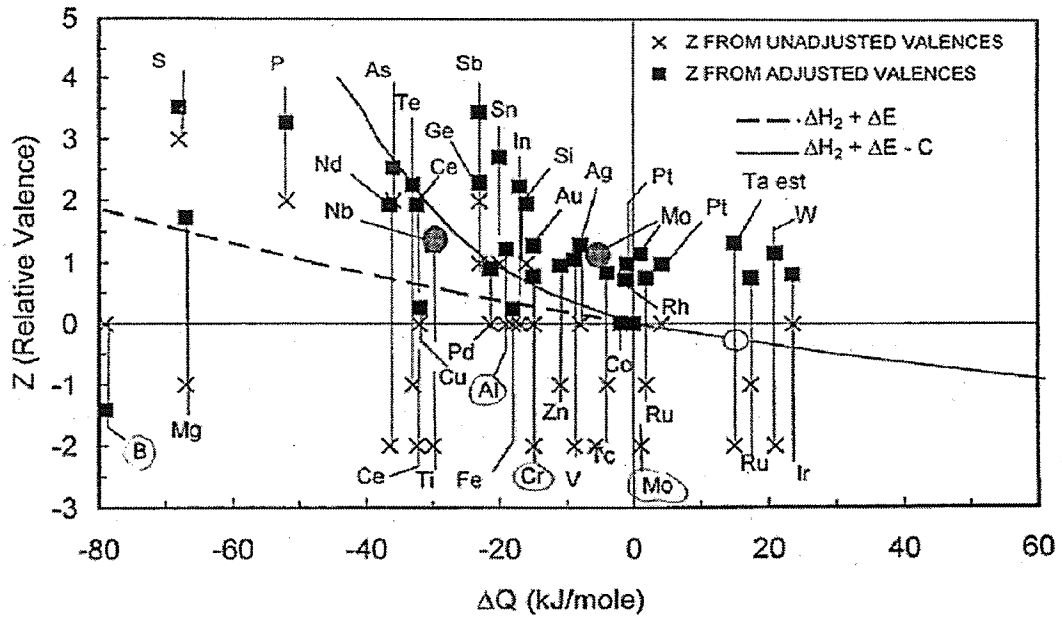

Figure 38: Activation energies for solute impurity diffusion in nickel [17]

OXIDE PRECIPITATES

Using EDS, it was shown that Al_2O_3 was the only oxide species to precipitate in the base material. The internal Al_2O_3 precipitates were found to extend from the oxide scale into the base material. With aluminum being in relatively low concentrations, the flux of aluminum cations to the scale is overtaken by the rapid growth of Cr_2O_3 during the initial stages of oxidation and accounts for the structures described in Table 13. Since oxygen diffusion in Al_2O_3 is greater along grain boundaries than in the lattice, the rate of oxide precipitate penetration in the base material will increase [26]. In Figure 33, fine dark lines appear along many of the grain boundaries in the Inconel 718 micro-weld coating. The lines are seen to extend from the coarse Al_2O_3 precipitates and suggest that the penetration of oxygen is increased deeper in the coating along the micro-weld grain structure. With a fine grain

structure of approximately 3 to 5 μm aligned perpendicular to the micro-welded coating's surface, the total grain boundary surface area has been largely increased by micro-welding. The increase in grain boundary area tends to indicate that additional diffusion paths have been created to further support internal oxidation. Therefore, the increase in spallation resistance of micro-welded coatings reported by Zhengwei et al [13] may come at the expense of increased penetration of oxidation precipitates in the material. The increase in internal precipitates extending from the scale supports the proposed pegging action of oxide scales which would reduce spallation.

5.4 RESIDUAL STRESS

5.4.1 RESULTS

Visual examination of the specimen after dissolution of the low alloy steel substrate confirms the presence of residual stresses in the coating. The specimen is predominantly curved along its shorter width in a concave fashion away from the mild steel base. This indicates that tensile stress is present in the coating. This result falls within expectations since in gas tungsten arc welding, the filler material and heat affected zone base material contract during solidification and cooling to generate internal tensile stresses. Therefore, a force of equal magnitude and opposite in direction is exerted by the substrate to maintain a balance of forces. The measured deflections at the specimen ends and the center are listed in Table 15.

Table 15: Measured deflections for residual stress analysis

Net Deflection (Y)		
End 1	**Center**	**End 2**
0.502 mm	1.06 mm	0.477 mm
Specimen width: 12.25 mm Specimen length: 29.50 mm Specimen thickness: 0.152 to 0.190 mm, Average = 0.171 mm		

Refer to Figure 10 for a photograph of the residual stress specimen after dissolution of the low alloy steel backing material.

Using equations described in Section 4.6.4, the calculated residual stresses are:

End 1: 510 MPa

Center: 1210 MPa

End 2: 600 MPa

Therefore, using the measurements listed in Table 15 and equations (1) through (5), the range of residual tensile stresses can exceed the ultimate tensile strength of Inconel 625 (840 to 1030 MPa).

Further testing using the X-ray diffraction technique described in [2] following the DOE described in this study should be carried out to further study the effect of processing parameters on the resulting residual stresses in micro-welded coatings. It is anticipated that as the pulse arc energy (voltage and current) is increased, the residual stresses in the coatings will increase. This hypothesis is based on R.N. Johnson's article [1] where he mentions that

as the pulse power is increased significantly, the process begins essentially becomes arc welding due to a high heat input which suppresses the rapid solidification.

5.4.2 DISCUSSION ON RESIDUAL STRESS RESULTS

Residual stresses were determined to be tensile in nature. Upon cooling in the liquid state, followed by solidification and cooling in the solid phase, the deposit contracts as dictated by its thermal coefficient of expansion and transformation from its liquid to solid phase. The approximate calculated internal stress value at the center of the specimen exceeded the ultimate tensile strength of Inconel 625. Based on this approximation, it can be concluded that the stresses present in the coating must be relatively high as compared to the material's ultimate tensile strength. The relatively high tensile stresses would account for the micro-cracking found in nearly all micro-weld coatings examined in this study.

As suggested by Zhengwei et al in [13], internal tensile stresses present in micro-weld coatings would be more desirable in thermal cyclic conditions for resistance to oxide scale spallation. As oxide scales grow, they generate internal compressive stresses, which would relieve the pre-existing internal tensile stresses in the coating.

6. CONCLUSIONS

Micro-welding with alloys Inconel 625, Inconel 718, Inconel 722, Inconel 738, Rene 41 and Nimonic 105 was used to evaluate the effect of process parameters on deposition rate, void content and crack density. The effect of process parameter on the micro-weld deposit hardness was also evaluated for Inconel 738 deposited onto itself.

Comparative oxidation tests were conducted to evaluate the oxidation behaviour of micro-welded Inconel 718, Inconel 722, Inconel 738 and Nimonic 105 coatings.

Using a beam deflection under uniform loading equation, an approximation of residual stresses in micro-weld deposits was obtained.

Conclusions are as follows:

- Voltage and current have significant effects on the deposition rate, void content and crack density of micro-welded deposits. The greatest deposition rates were obtained with high values for voltage and current (200 Volts, 5 Amperes). The void content and crack density can be reduced by using low values for voltage and current (100 Volts, 3 Amperes). The capacitance did not have a significant effect on the void content and crack density in the deposits.

- Capacitance, voltage and current were found to have a significant effect on the deposit's hardness. Increasing each of the parameters caused a decrease in the deposit's hardness. High cooling rates during the micro-welding process are responsible for the increased coating hardness.

- Process models were generated for the effects of capacitance, voltage and current on deposition rate, void content, crack density and deposit hardness. With a threshold p-value of 0.1, process models could not be generated for all results. Curvature in the results was found to be significant and prohibited the generation of process models. The frequent occurrence of excessive curvature in the results indicated that the selected range of process parameters for this design of experiments covered too broad of a range for the micro-welding process.

- Micro-welding is a suitable process for the application of alloys rich in aluminum and titanium. For all micro-weld filler alloys tested in this study, the cast Inconel 738 base material remained free of heat affected zone micro-cracks.

- The oxidation rate of micro-welded Inconel 738 was practically identical to that of uncoated Inconel 738. The parabolic oxidation rates of alloys tested in this study were found to vary linearly with the aluminum + chromium concentrations. All alloys tested formed external Al_2O_3 and Cr_2O_3 oxide scales, internal Al_2O_3 precipitates and a chromium depleted zone.

- Residual stresses in micro-weld deposits are tensile in nature. The approximate magnitude of residual stresses has been determined to be relatively high with respect to the material's ultimate tensile strength. Subsequent stress relieving after the application of micro-weld coatings may be required if the coating is to be subjected to tensile loads in service.

7. FUTURE WORK

Recommended future work in this field is as follows:

- Conduct a sub-set of design of experiments over the range of parameters used in this study. The initial DOE should be divided into eight DOE's with a narrower range of parameters such that the effects of curvature are reduced and statistically significant process models can be established. Since there were no significant trends in deposition rates, void content and crack density between the filler alloys used in this study, a future project could be carried out on self-welded Inconel 738.

- Conduct a comparative study of simulated repairs using micro-welding, GTAW, EBW, LBW and diffusion brazing to assess the relative performance of micro-welded deposits for the repair of gas turbine blades and vanes. In such a study, one should attempt to conduct repairs to a γ' superalloy such as Inconel 738 by matching the filler alloy. The relative performance of repair processes is to be assessed in terms of thermal-mechanical fatigue and corrosion resistance under turbine operating conditions.

- Based on the current author's attendance at a coating's seminar held by General Electric, Tribaloy 800 alloy is seeing increased applications in hot-end gas turbine components. With modifications to existing micro-welding power supplies, the pulse power could be increased in order to improve deposition rates. The goal of this study would be to establish the best balance between processing parameters in order to achieve maximum deposition rates while meeting typical high velocity oxy-fuel (HVOF) thermal sprayed Tribaloy 800 coatings to turbine components. A thermal-mechanical fatigue analysis

between high-power micro-welded and HVOF sprayed Tribaloy 800 should be conducted to compare coating performance under turbine operating conditions.

- Investigate the crystallographic structure of micro-welded nickel based γ' superalloys with orientation imaging microscopy, x-ray diffraction and transmission electron microscopy. At present time, a columnar structure appears under scanning electron microscope examination but the crystalline structure and relative orientation of fine grains remain to be assessed. As claims of amorphous or near-amorphous structures have been made in the past, further investigation is required in order to determine the exact cause for the observed increase in coating hardness with lower pulse powers.

- Conduct a comparative study on alternate stress relieving processes in order to reduce internal residual stresses in micro-weld deposits. Being tensile in nature and of significant magnitude, the reduction of residual stresses appears to be necessary in application where the deposit is to be loaded in tension during service. Since elevated temperature stress relief can have detrimental effects on close tolerance assemblies, non-heat or low-heat input processes are to be investigated. Shot peening is a process whereby compressive stresses are induced in the substrate's surface and could offset the tensile residual stresses. Laser surface treating can be a low heat input process capable of relaxing internal residual stresses by locally heating the material. X-ray diffraction should be used to accurately measure internal residual stresses before and after each treatment.

8. REFERENCES

1. R.N. Johnson, "Electro-Spark Deposition: Principles and Applications", *Society of Vacuum Coaters 45th Annual Technical Conference*, April 2002, pp 87-92, 2002

2. A.V. Paustovskii and Y.V. Gubin, "Stresses in Coatings Obtained by Electro-Spark Alloying And Laser Processing (Review)" *Materials Science*, vol. 33, no. 6, pp 770-776, 1997

3. F. Korobeinik, S.I. Rudyuk and S.V. Korobeini, "Characteristics of The Formation Of Microtopography, Microstructure and Substruture of The Surface Layer During Electro-Spark Alloying", *Elektronnaya Obrabotka Materialov*, no. 1, pp 16-19, 1989

4. G.L. Sheldon and R.N. Johnson, "Electro-Spark Deposition – A Technique For Producing Wear Resistant Coatings", *Wear of Materials: International Conference on Wear of Materials*, pp 388-396, 1985

5. G.L. Sheldon, R. Wang and R.A. Clark, "Characteristics of Ni-Ti Surface Alloys Formed By Electrospark Deposition", *Surface & Coatings Technology*, vol. 36, no. 1-2, , pp 445-454, 1988

6. Zhengwei Li, Wei Gao, Yedong He, "Protection Of A Ti_3Al-Nb Alloy By Electro-Spark Deposition Coating", *Scripta Materialia*, vol. 45, no. 9, pp 1099-1105, November 2001

7. E.A. Brown III, G.L. Sheldon and A.E. Bayoumi, "A Parametric Study On Improving Tool Life By Electrospark Deposition", *Wear of Materials: International Conference on Wear of Materials*, pp 547-555, 1989

8. K.C. Antony and G.W. Goward (Edited by S. Reichman, D.N. Duhl, G. Maurer, S. Antolovich and C. Lund), "Aircraft Gas Turbine Blade And Vane Repair", *Superalloys 1988*, pp 745-754, 1988

9. D.W. Gandy, G. Frederick, J.T. Stover and R. Viswanathan, "Overview of Hot Section Component Repair Methods", *paper presented at the ASM 2000 Conference*, St. Louis, Missouri, ASM October 2000

10. K. Banerjee, N.L.Richards and M.C. Chatervedi, "Effect of Filler Alloys on HAZ Cracking in Pre-Weld Heat Treated IN-738 LC GTA Welds", accepted for publication by Metallurgical and Materials Transaction, 2005

11. A. Thakur, N.L. Richards, M.C. Chaturvedi, "On Crack-Free Welding of Cast Inconel 738", *International Journal for the Joining of Materials*, vol. 15, no. 4, pp 21-25, December 2003

12. F.I. Wei and F.H. Stott, "The Influence of Aluminum on the Oxidation of a Cr_2O_3 Forming Nickel-Chromium Alloy", *Reactivity of Solids*, vol. 6, no. 2-3, pp 129-144, December 1988

13. Zhengwei Li, Wei Gao, Puiming Kwok, Sean Li, Yedong He, "Electro-Spark Deposition Coatings for High Temperature Oxidation Resistance", *High Temperature Materials and Processes*, vol. 19, no. 6, , pp 443-458, November 2000

14. G.A.Green, C.C.Finfrock, "Oxidation of Inconel 718 in Air at High Temperatures", *Oxidation of Metals*, vol. 55, no. 5-6, pp 505-521, June 2001

15. M.F.Berezhnitskaya, A.V. Paustovskii and S.N. Kirilenko, "Determination of Residual Stresses in Electro-Spark Deposited Coatings", *Strength of Materials (Ukraine)*, vol. 35, no. 6, 2003, pp 633-638, November-December 2003

16. N.L. Richards and M.C. Chaturvedi, "Weld Repair of Single Crystal and DS Cast Superalloys", *Final report for NRC Institute for Aerospace Research*, Ottawa, Canada, June 2001

17. V. Burachynsky and J.R. Cahoon, "A Theory for Solute Impurity Diffusion, Which Considers Engel-Brewer Valences, Balancing the Fermi Energy Levels of Solvent and Solute, and Differences in Zero Point Energy", *Metallurgical and Materials Transactions A: Physical Metallurgy and Materials Science*, v 28A, n 3, Mar. 1997, p 563-582

18. A.D. Le Claire, "On the Theory of Impurity Diffusion in Metals", *Philosophical Magazine*, vol. 7, no. 73, pp 141-167, January 1962

19. E.E. Underwood, "Quantitative Metallography", ASM Handbook, vol. 9, *Metallography and Microstructures,* ASM International, pp. 123-134, 1985

20. American Society for Metals Handbooks, Volume 13, "Corrosion"

21. ASTM G54-84(1996), "Standard Practice for Simple Static Oxidation Testing"

22. W. Kurz, D.J. Fisher, "Fundamentals of Solidification", Trans Tech Publications Ltd., 1986

23. R. Johnson, "Energy Dispersive X-Ray Microanalysis – An Introduction", Kevex Corporation, 1988

24. J. Friel, "X-Ray and Image Analysis in Electron Microscopy" Princeton Gamma-Tech Inc., Second Printing, 1998

25. M.G. Fontana, "Corrosion Engineering", Third Edition, McGraw Hill Series in Materials Science and Engineering, 1986

26. N.Birks, G.H.Meierr, "Introduction to High Temperature Oxidation of Metals", Edward Arnold (Publishers) Ltd, 1983

27. C. Sims, N.S.Stoloff, W.C.Hagel, "Superalloys II – High Temperature Materials for Aerospace and Industrial Power", John Wiley and Sons, 1987

28. F.P. Beer, E.R. Johnston Jr., "Mechanics of Materials", McGraw Hill Inc., 1992

APPENDIX A – CLEMEX IMAGE ANALYSIS ROUTINE FOR VOID CONTENT MEASUREMENTS

001 Grab
002 Delineation x1
003 Gray Threshold
  BPL1 range 0..110
  BPL3 range 111..255
004 Trap BPL1 -> BPL3 4x4
005 Trap BPL1 -> BPL3 7x7
006 Trap BPL1 -> BPL3 7x7
007 Object Measures (BPL1) -> OBJM1
  Area

APPENDIX B - CLEMEX IMAGE ANALYSIS ROUTINE FOR CRACK DENSITY MEASUREMENTS

001 Grab
002 Delineation x1
003 Gray Threshold
  BPL1 range 0..110
  BPL3 range 111..255
004 Trap BPL1 -> BPL3 4x4
005 Trap BPL1 -> BPL3 7x7
006 Trap BPL1 -> BPL3 7x7
007 Trap BPL1 -> None 2x2
008 Set Guard Frame to 4,106 756x347
009 Object Measures (BPL1) -> OBJM1

APPENDIX C – CUBE PLOTS

INCONEL 625

Centerpoint
Factorial Point

Cube Plot (data means) for DEP

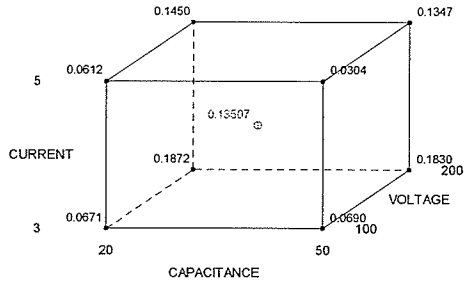

Centerpoint
Factorial Point

Cube Plot (data means) for VOID

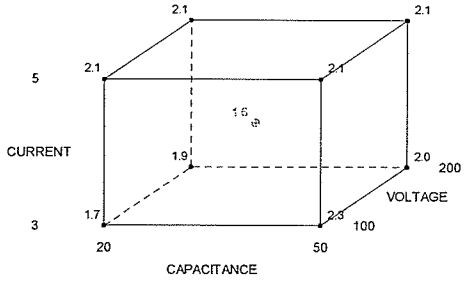

Centerpoint
Factorial Point

Cube Plot (data means) for CRACK

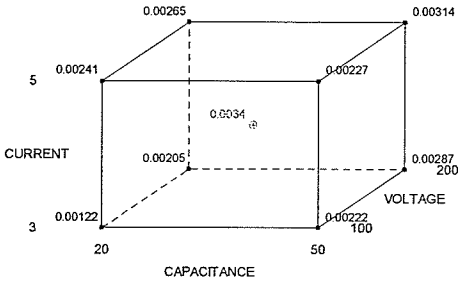

INCONEL 718

Centerpoint
Factorial Point

Cube Plot (data means) for DEP

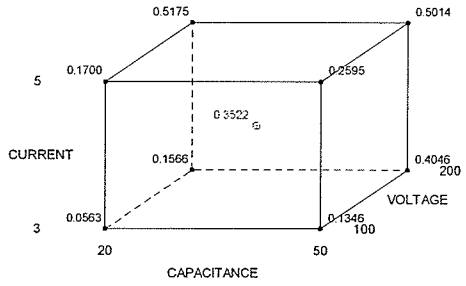

Centerpoint
Factorial Point

Cube Plot (data means) for VOID

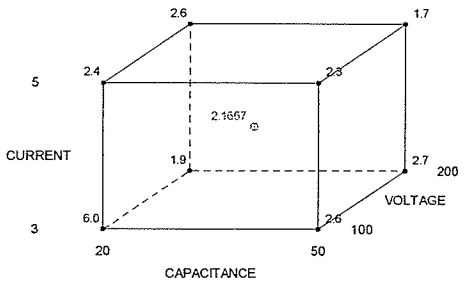

Centerpoint
Factorial Point

Cube Plot (data means) for CRACK

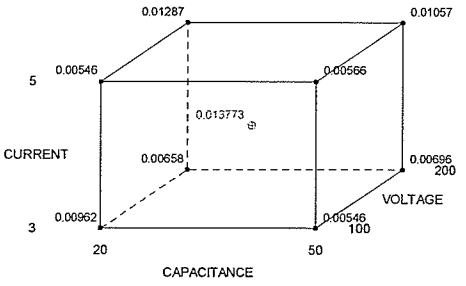

INCONEL 722

Centerpoint
Factorial Point

Cube Plot (data means) for DEPOSITION RATE

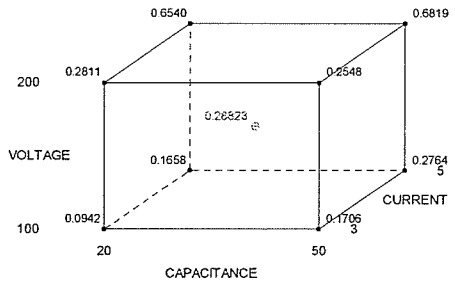

Centerpoint
Factorial Point

Cube Plot (data means) for VOID CONTENT

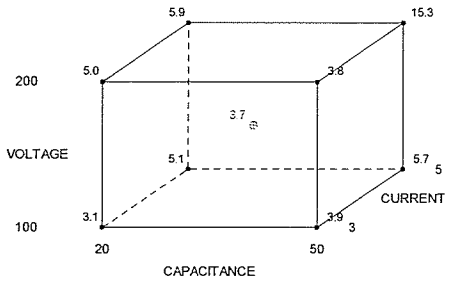

Centerpoint
Factorial Point

Cube Plot (data means) for CRACK DENSITY

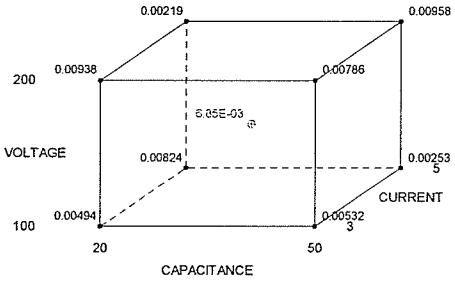

INCONEL 738

Centerpoint
Factorial Point

Cube Plot (data means) for DEP

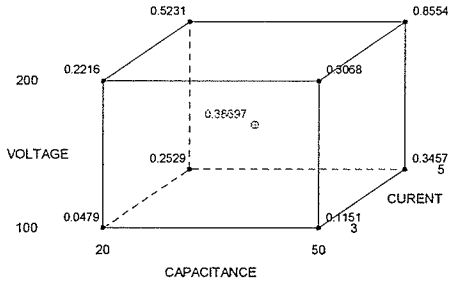

Centerpoint
Factorial Point

Cube Plot (data means) for VOID

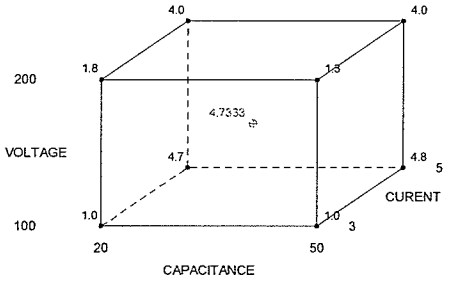

Centerpoint
Factorial Point

Cube Plot (data means) for CRACK

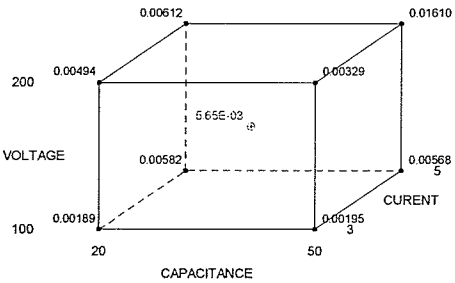

Centerpoint
Factorial Point

Cube Plot (data means) for DEP

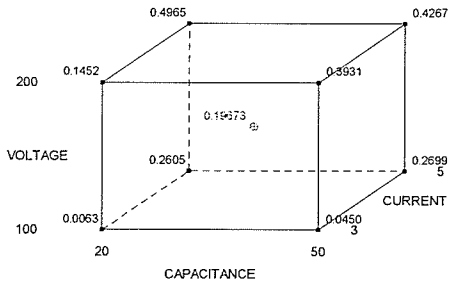

Centerpoint
Factorial Point

Cube Plot (data means) for VOID

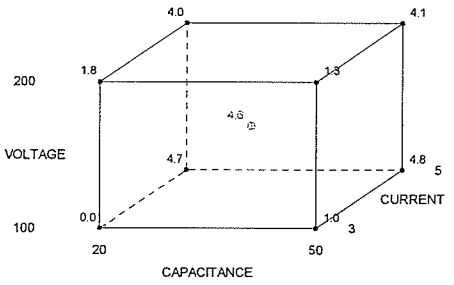

Centerpoint
Factorial Point

Cube Plot (data means) for CRACK

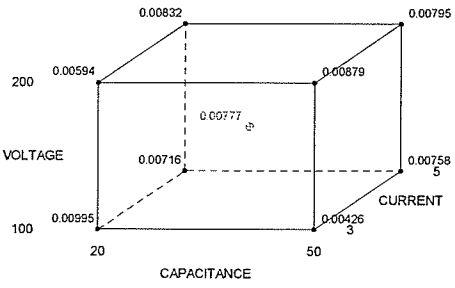

Centerpoint
Factorial Point

Cube Plot (data means) for DEPOSITION RATE

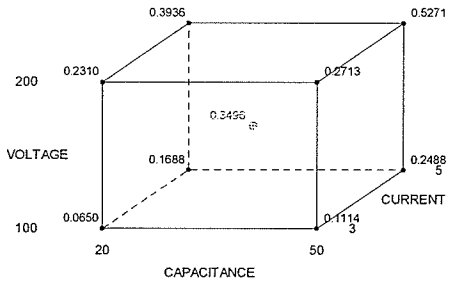

Centerpoint
Factorial Point

Cube Plot (data means) for VOID CONTENT

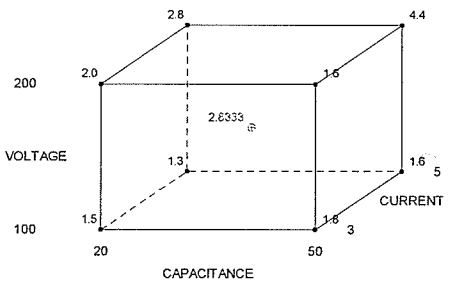

Centerpoint
Factorial Point

Cube Plot (data means) for CRACK DENSITY

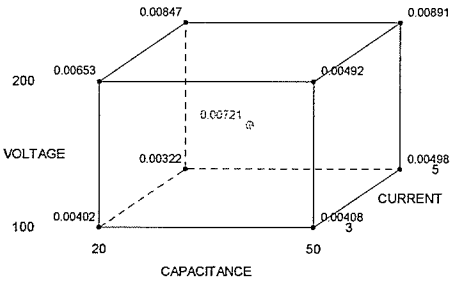

APPENDIX D – INTERACTIONS PLOTS

INCONEL 625

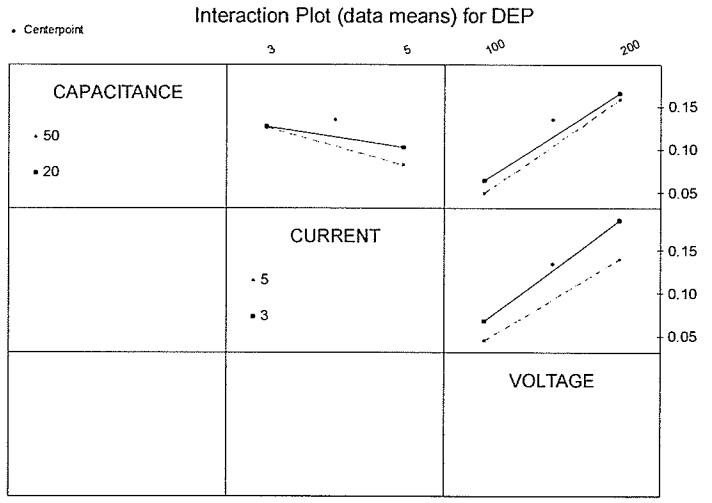

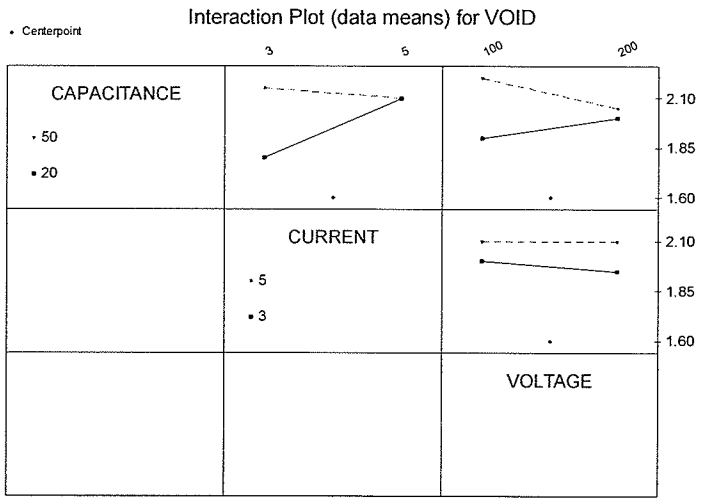

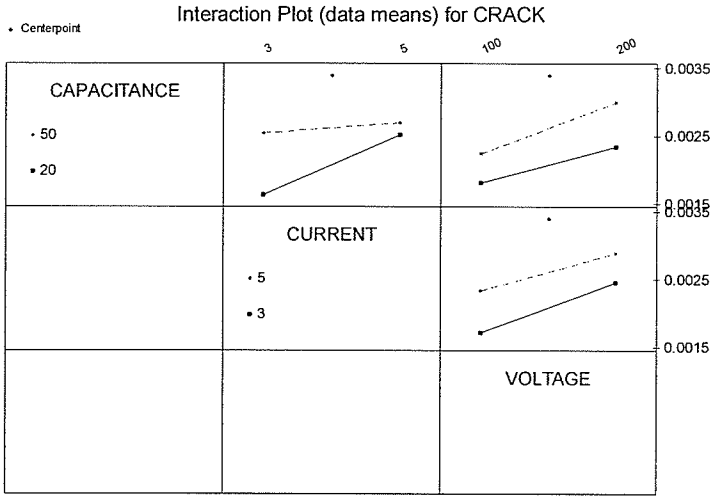

INCONEL 718

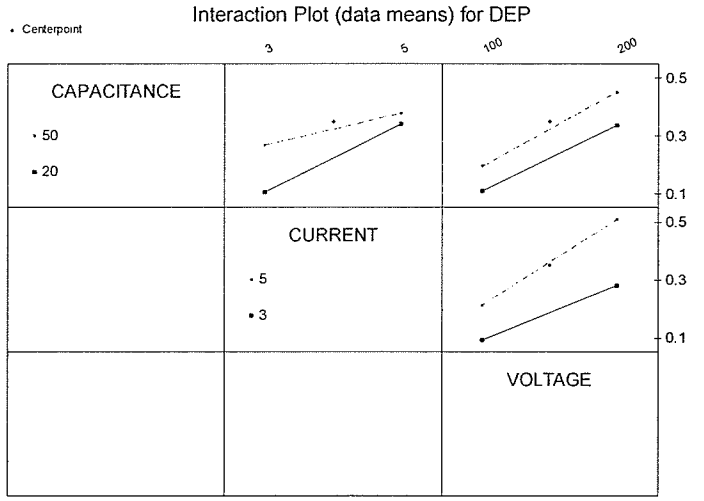
Interaction Plot (data means) for DEP
Centerpoint
3
5
100
200
CAPACITANCE
50
20
CURRENT
5
3
VOLTAGE
0.5
0.3
0.1

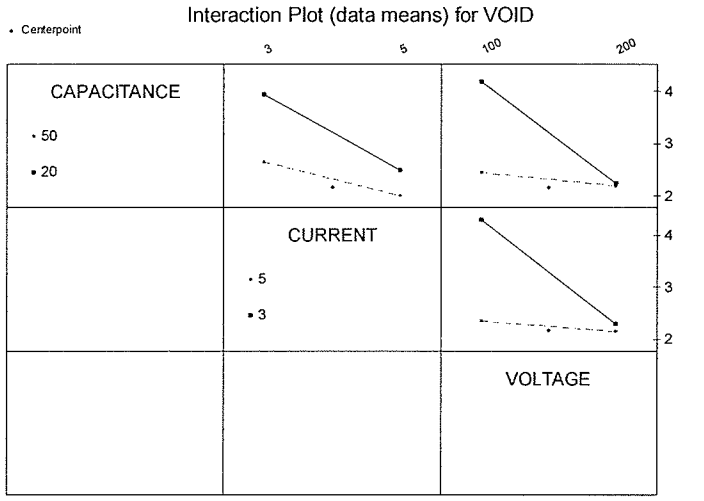
Interaction Plot (data means) for VOID
Centerpoint
3
5
100
200
CAPACITANCE
50
20
CURRENT
5
3
VOLTAGE
4
3
2

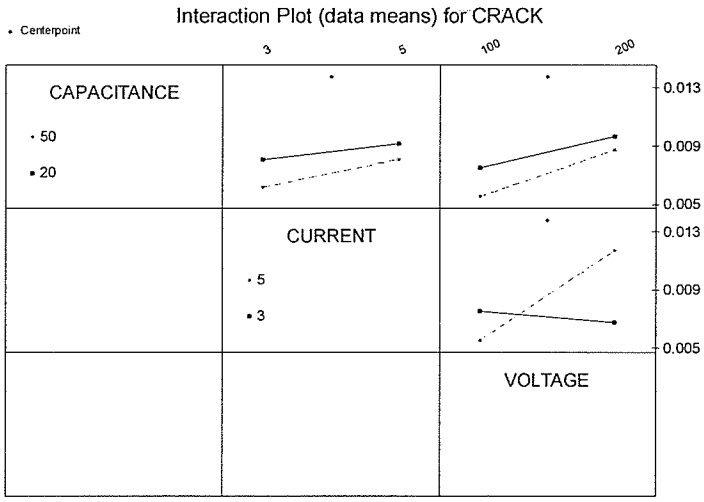
Interaction Plot (data means) for CRACK
Centerpoint
3
5
100
200
CAPACITANCE
50
20
CURRENT
5
3
VOLTAGE
0.013
0.009
0.005

INCONEL 722

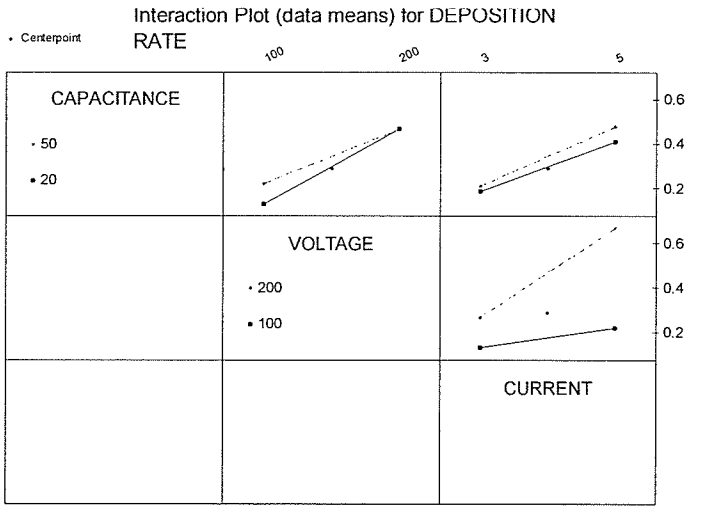
Interaction Plot (data means) for DEPOSITION RATE
Centerpoint
100
200
3
5
CAPACITANCE
50
20
VOLTAGE
200
100
CURRENT
0.6
0.4
0.2

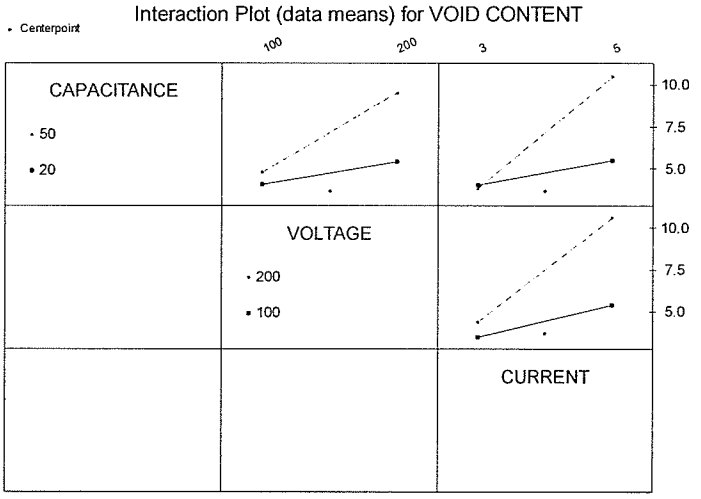
Interaction Plot (data means) for VOID CONTENT
Centerpoint
100
200
3
5
CAPACITANCE
50
20
VOLTAGE
200
100
CURRENT
10.0
7.5
5.0

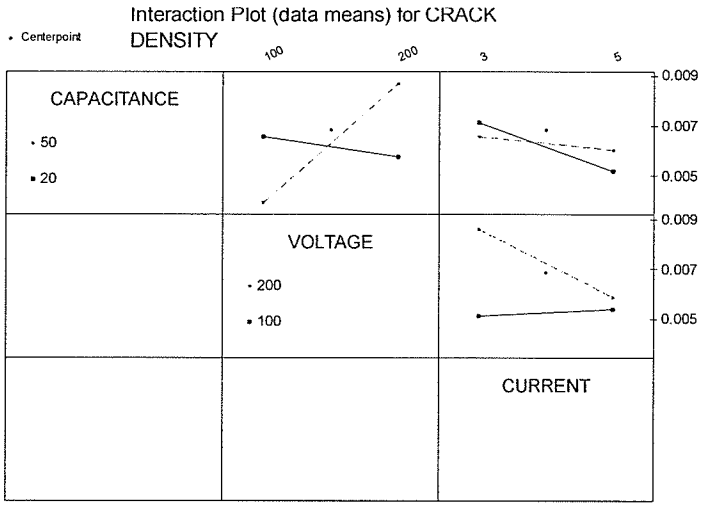
Interaction Plot (data means) for CRACK DENSITY
Centerpoint
100
200
3
5
CAPACITANCE
50
20
VOLTAGE
200
100
CURRENT
0.009
0.007
0.005

INCONEL 738

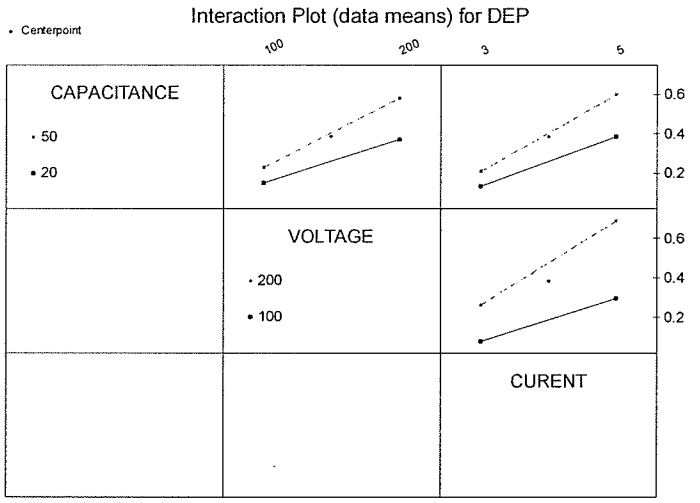
Interaction Plot (data means) for DEP
Centerpoint
100
200
3
5
CAPACITANCE
50
20
VOLTAGE
200
100
CURENT
0.6
0.4
0.2

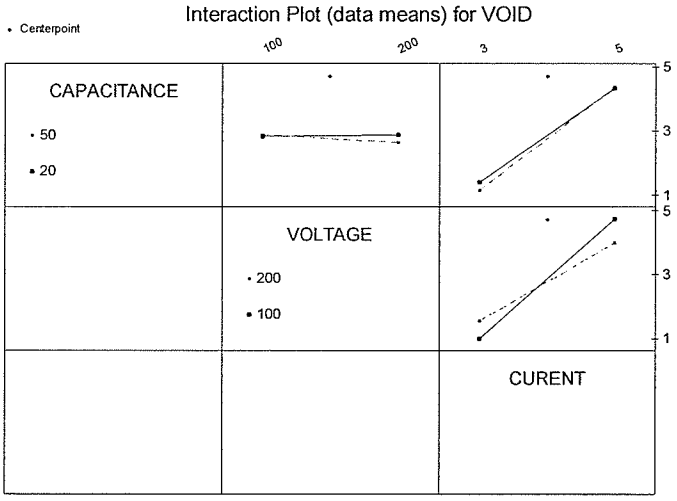
Interaction Plot (data means) for VOID
Centerpoint
100
200
3
5
CAPACITANCE
50
20
VOLTAGE
200
100
CURENT
5
3
1

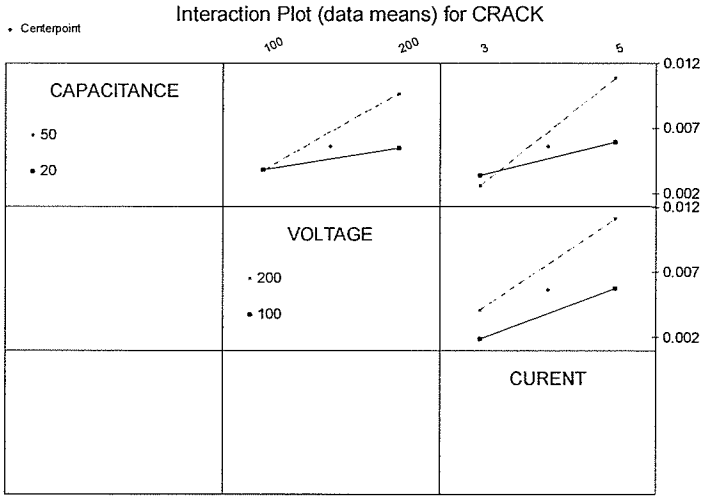
Interaction Plot (data means) for CRACK
Centerpoint
100
200
3
5
CAPACITANCE
50
20
VOLTAGE
200
100
CURENT
0.012
0.007
0.002

RENE 41

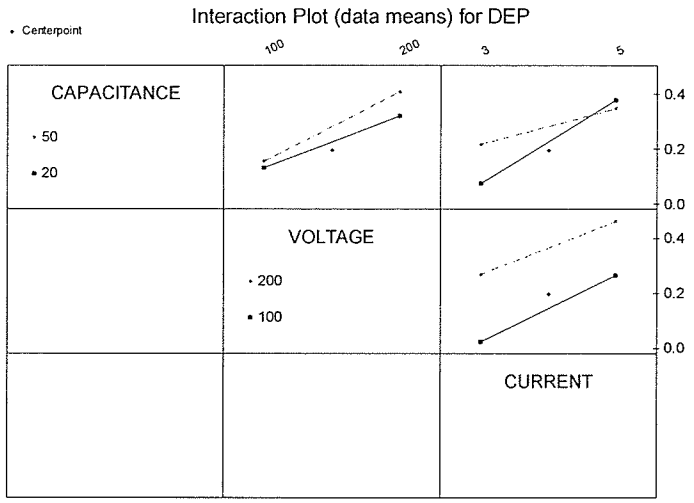
Interaction Plot (data means) for DEP
Centerpoint
100
200
3
5
CAPACITANCE
50
20
VOLTAGE
200
100
CURRENT
0.4
0.2
0.0

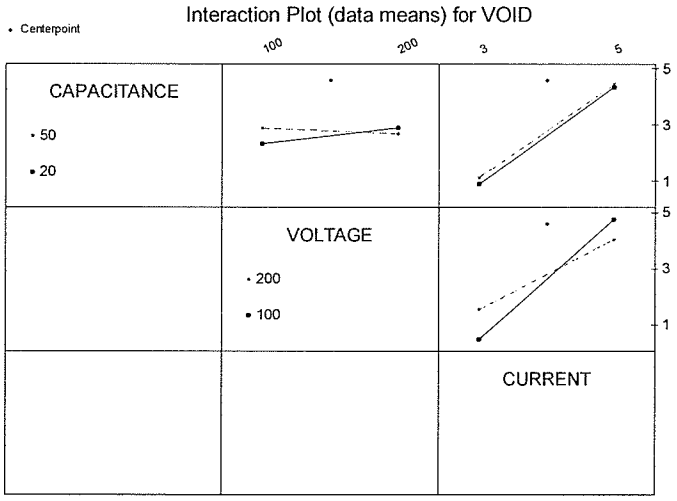
Interaction Plot (data means) for VOID
Centerpoint
100
200
3
5
CAPACITANCE
50
20
VOLTAGE
200
100
CURRENT
5
3
1

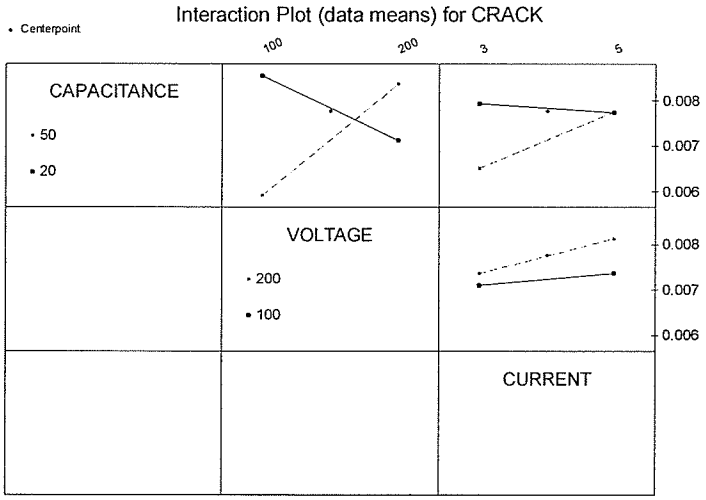
Interaction Plot (data means) for CRACK
Centerpoint
100
200
3
5
CAPACITANCE
50
20
VOLTAGE
200
100
CURRENT
0.008
0.007
0.006

NIMONIC 105

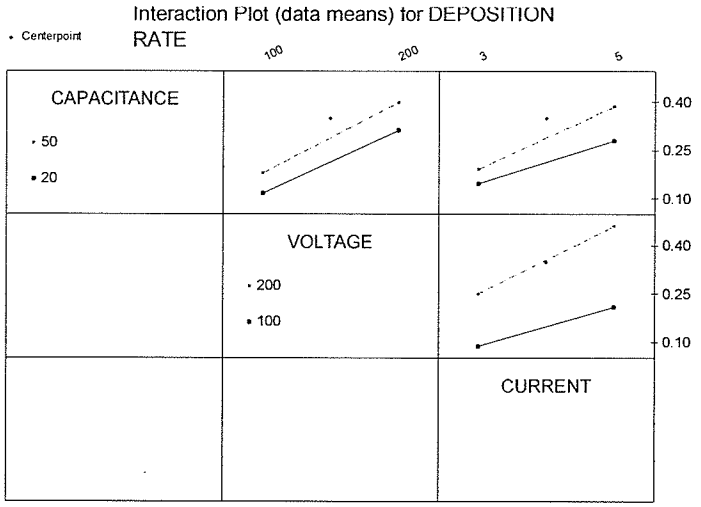
Interaction Plot (data means) for DEPOSITION RATE
Centerpoint
100
200
3
5
CAPACITANCE
50
20
VOLTAGE
200
100
CURRENT
0.40
0.25
0.10
0.40
0.25
0.10

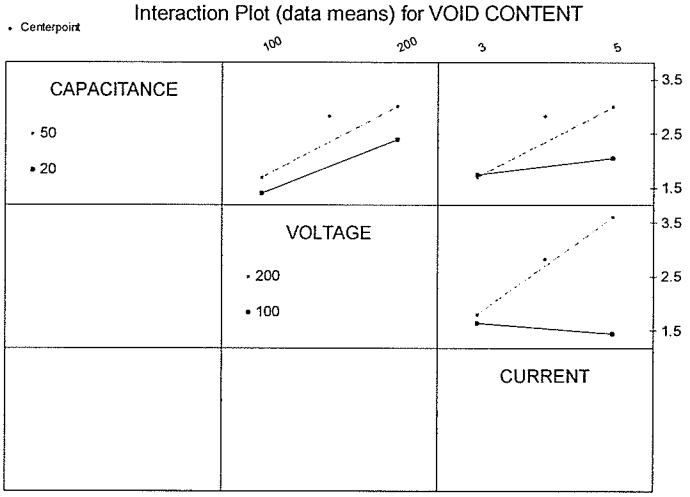
Interaction Plot (data means) for VOID CONTENT
Centerpoint
100
200
3
5
CAPACITANCE
50
20
VOLTAGE
200
100
CURRENT
3.5
2.5
1.5
3.5
2.5
1.5

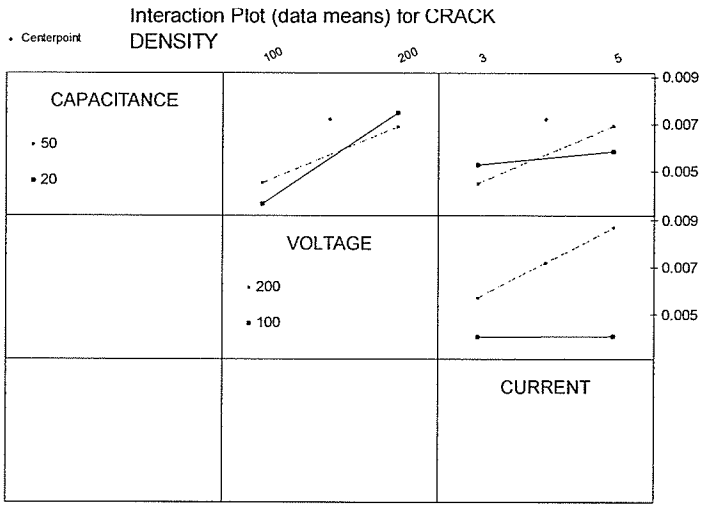
Interaction Plot (data means) for CRACK DENSITY
Centerpoint
100
200
3
5
CAPACITANCE
50
20
VOLTAGE
200
100
CURRENT
0.009
0.007
0.005
0.009
0.007
0.005

APPENDIX E – MAIN EFFECTS PLOTS

INCONEL 625

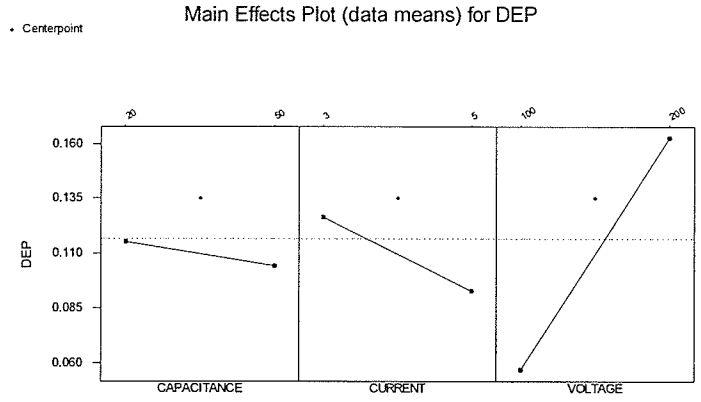

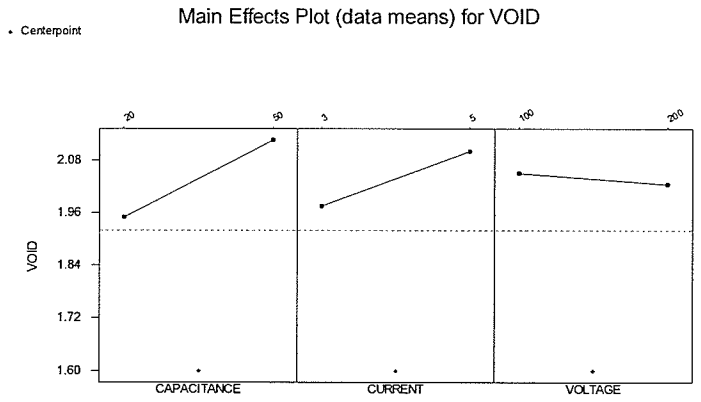

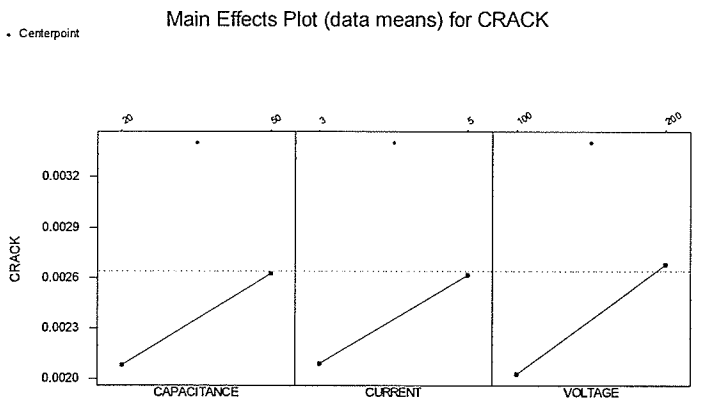

INCONEL 718

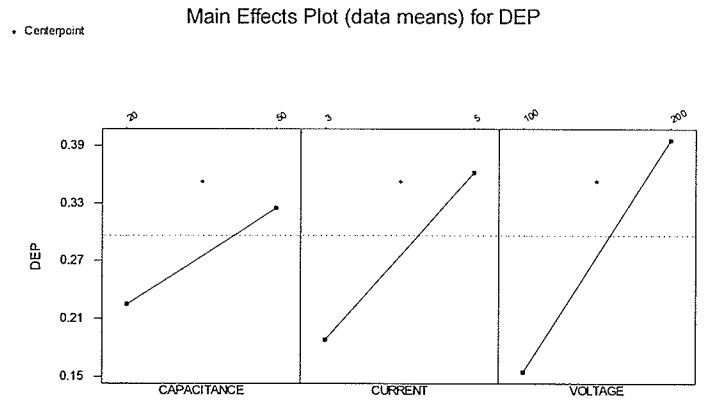
Main Effects Plot (data means) for DEP
Centerpoint
20
50
3
5
100
200
0.39
0.33
0.27
0.21
0.15
DEP
CAPACITANCE
CURRENT
VOLTAGE

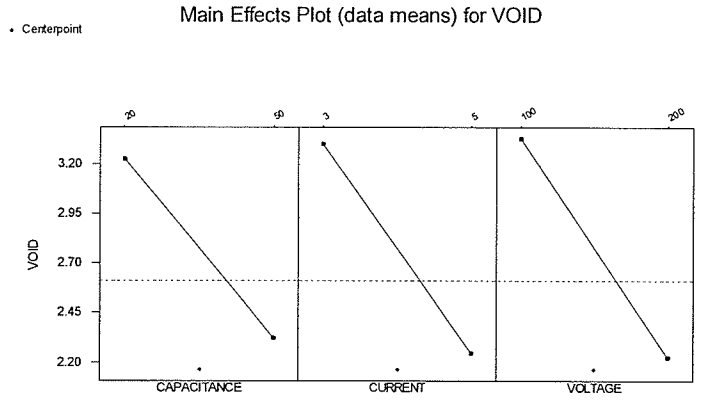
Main Effects Plot (data means) for VOID
Centerpoint
20
50
3
5
100
200
3.20
2.95
2.70
2.45
2.20
VOID
CAPACITANCE
CURRENT
VOLTAGE

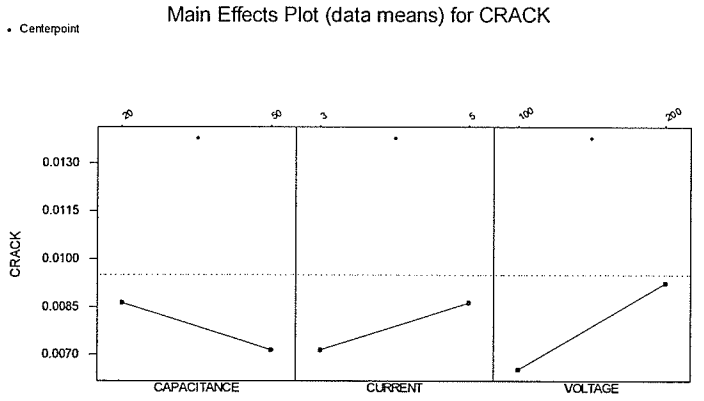
Main Effects Plot (data means) for CRACK
Centerpoint
20
50
3
5
100
200
0.0130
0.0115
0.0100
0.0085
0.0070
CRACK
CAPACITANCE
CURRENT
VOLTAGE

INCONEL 722

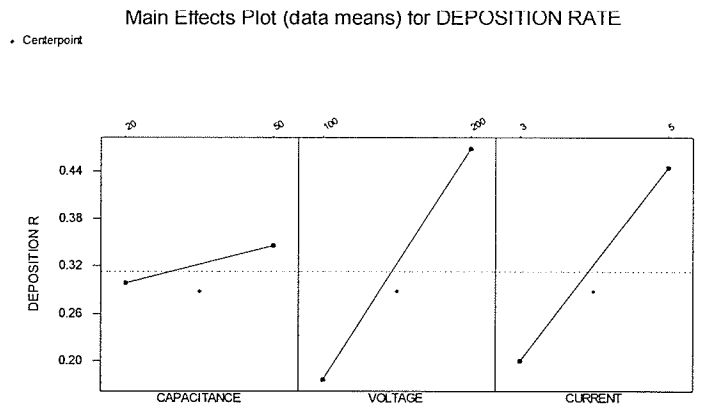
Main Effects Plot (data means) for DEPOSITION RATE
Centerpoint
20
50
100
200
3
5
0.44
0.38
0.32
0.26
0.20
DEPOSITION R
CAPACITANCE
VOLTAGE
CURRENT

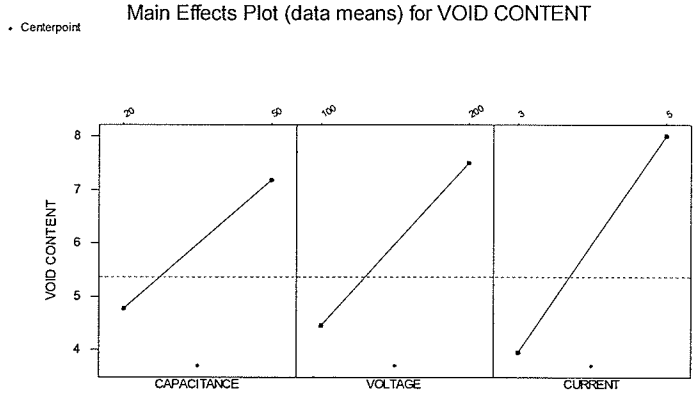
Main Effects Plot (data means) for VOID CONTENT
Centerpoint
20
50
100
200
3
5
8
7
6
5
4
VOID CONTENT
CAPACITANCE
VOLTAGE
CURRENT

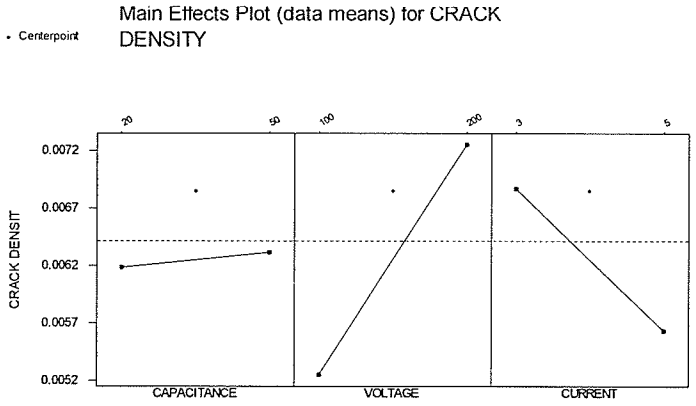
Main Effects Plot (data means) for CRACK DENSITY
Centerpoint
20
50
100
200
3
5
0.0072
0.0067
0.0062
0.0057
0.0052
CRACK DENSIT
CAPACITANCE
VOLTAGE
CURRENT

INCONEL 738

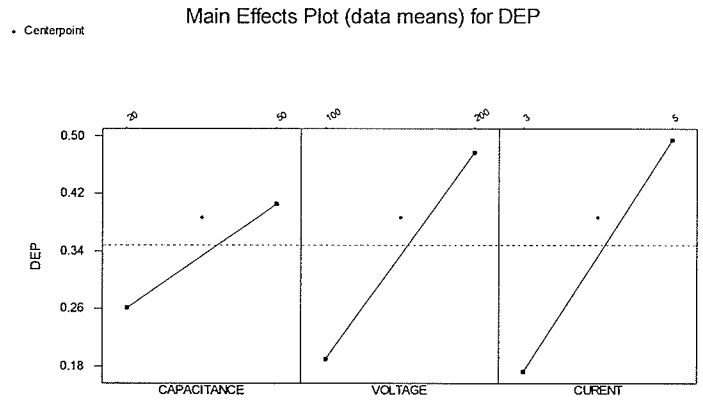
Main Effects Plot (data means) for DEP
Centerpoint
20
50
100
200
3
5
0.50
0.42
0.34
0.26
0.18
DEP
CAPACITANCE
VOLTAGE
CURENT

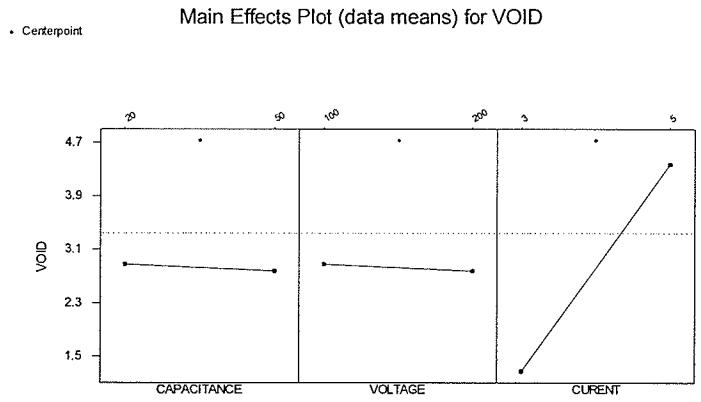
Main Effects Plot (data means) for VOID
Centerpoint
20
50
100
200
3
5
4.7
3.9
3.1
2.3
1.5
VOID
CAPACITANCE
VOLTAGE
CURENT

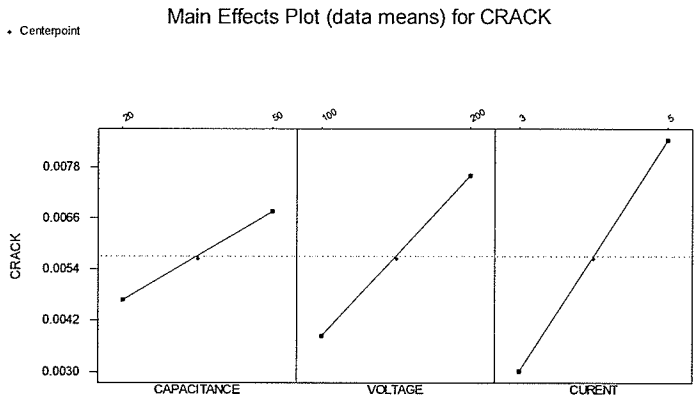
Main Effects Plot (data means) for CRACK
Centerpoint
20
50
100
200
3
5
0.0078
0.0066
0.0054
0.0042
0.0030
CRACK
CAPACITANCE
VOLTAGE
CURENT

RENE 41

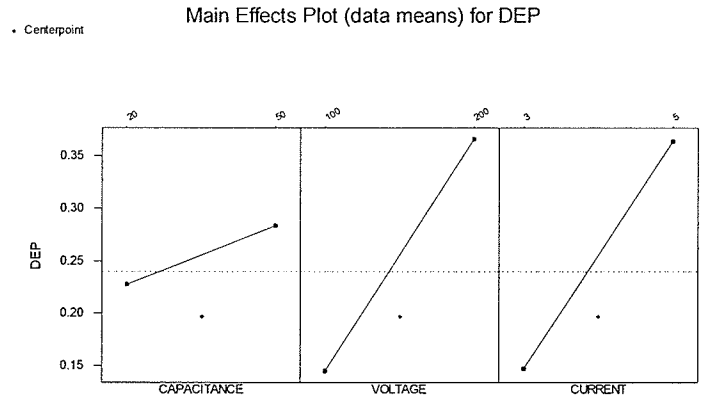
Main Effects Plot (data means) for DEP
Centerpoint
20
50
100
200
3
5
0.35
0.30
0.25
0.20
0.15
DEP
CAPACITANCE
VOLTAGE
CURRENT

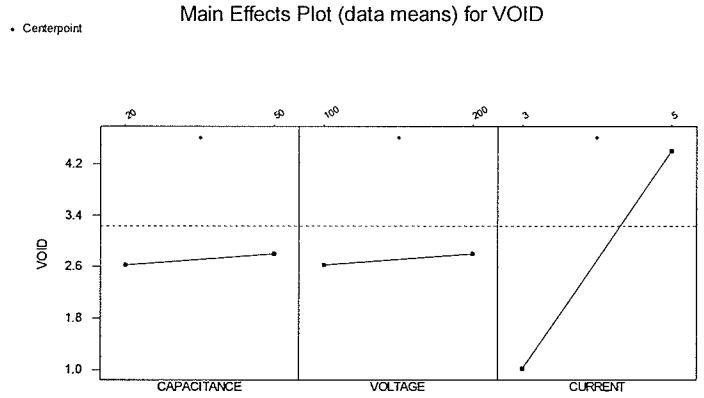
Main Effects Plot (data means) for VOID
Centerpoint
20
50
100
200
3
5
4.2
3.4
2.6
1.8
1.0
VOID
CAPACITANCE
VOLTAGE
CURRENT

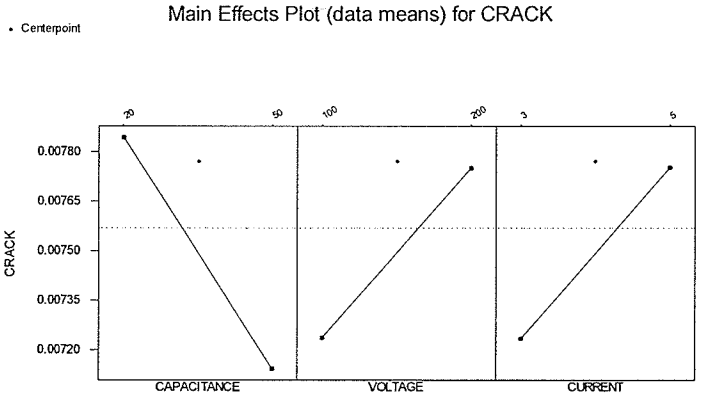
Main Effects Plot (data means) for CRACK
Centerpoint
20
50
100
200
3
5
0.00780
0.00765
0.00750
0.00735
0.00720
CRACK
CAPACITANCE
VOLTAGE
CURRENT

NIMONIC 105

Main Effects Plot (data means) for DEPOSITION RATE

• Centerpoint

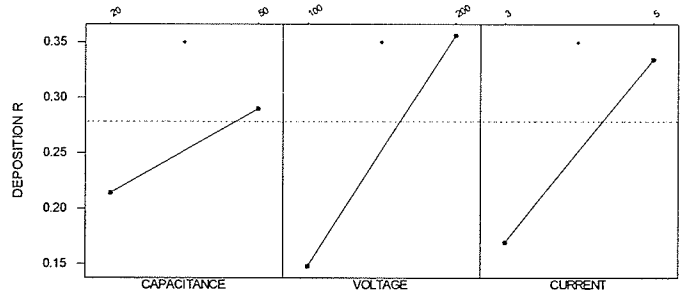

Main Effects Plot (data means) for VOID CONTENT

• Centerpoint

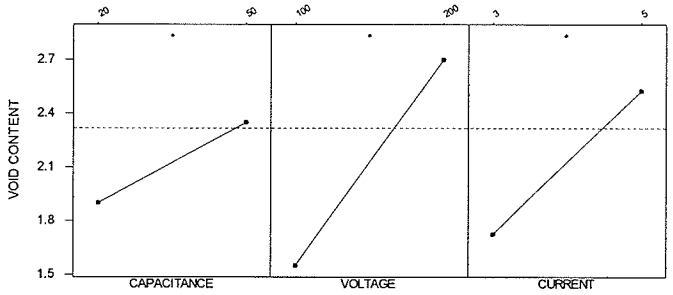

Main Effects Plot (data means) for CRACK DENSITY

• Centerpoint

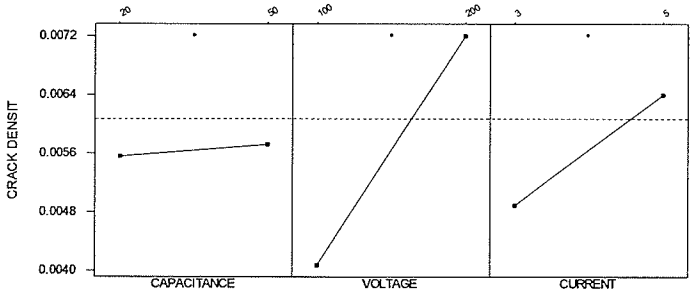

APPENDIX F – MINITAB REPORTS

INCONEL 625

Fractional Factorial Fit: DEPOSITION RATE, VOID CONTENT, CRACK DENSITY

Fractional Factorial Fit: DEPOSITION RATE versus CAPACITANCE, VOLTAGE, CURRENT

Estimated Effects and Coefficients for DEPOSITION RATE (coded units)

Term	Effect	Coef	SE Coef	T	P
Constant		0.10970	0.01453	7.55	0.017
CAPACITA	-0.01085	-0.00543	0.01453	-0.37	0.745
VOLTAGE	-0.03375	-0.01688	0.01453	-1.16	0.365
CURRENT	0.10555	0.05278	0.01453	3.63	0.068
CAPACITA*VOLTAGE	-0.00970	-0.00485	0.01453	-0.33	0.770
CAPACITA*CURRENT	0.00360	0.00180	0.01453	0.12	0.913
VOLTAGE*CURRENT	-0.01150	-0.00575	0.01453	-0.40	0.730
CAPACITA*VOLTAGE*CURRENT	0.00665	0.00332	0.01453	0.23	0.840
Ct Pt		0.02537	0.02781	0.91	0.458

Analysis of Variance for DEPOSITI (coded units)

Source	DF	Seq SS	Adj SS	Adj MS	F	P
Main Effects	3	0.0247952	0.0247952	0.00826506	4.90	0.174
2-Way Interactions	3	0.0004786	0.0004786	0.00015953	0.09	0.956
3-Way Interactions	1	0.0000884	0.0000884	0.00008844	0.05	0.840
Curvature	1	0.0014039	0.0014039	0.00140393	0.83	0.458
Residual Error	2	0.0033757	0.0033757	0.00168785		
Pure Error	2	0.0033757	0.0033757	0.00168785		
Total	10	0.0301419				

Observations for DEPOSITI

Obs	DEPOSITI	Fit	SE Fit	Residual	St Resid
1	0.067100	0.067100	0.041083	0.000000	* X
2	0.069000	0.069000	0.041083	0.000000	* X
3	0.061200	0.061200	0.041083	0.000000	* X
4	0.030400	0.030400	0.041083	0.000000	* X
5	0.187200	0.187200	0.041083	-0.000000	* X
6	0.183000	0.183000	0.041083	-0.000000	* X
7	0.145000	0.145000	0.041083	0.000000	* X
8	0.134700	0.134700	0.041083	-0.000000	* X
9	0.097600	0.135067	0.023720	-0.037467	-1.12
10	0.179000	0.135067	0.023720	0.043933	1.31
11	0.128600	0.135067	0.023720	-0.006467	-0.19

X denotes an observation whose X value gives it large influence.

Estimated Coefficients for DEPOSITI using data in uncoded units

Term	Coef
Constant	-0.217367
CAPACITA	0.0027883
VOLTAGE	0.00096950
CURRENT	0.089100
CAPACITA*VOLTAGE	-2.42000E-05
CAPACITA*CURRENT	-0.00054500

```
VOLTAGE*CURRENT           -0.000270167
CAPACITA*VOLTAGE*CURRENT 0.0000044333
Ct Pt                       0.0253667

Least Squares Means for DEPOSITI

                                  Mean   SE Mean
CAPACITA
20                             0.11513   0.02054
50                             0.10428   0.02054
VOLTAGE
100                            0.12658   0.02054
200                            0.09282   0.02054
CURRENT
3                              0.05692   0.02054
5                              0.16248   0.02054
CAPACITA*VOLTAGE
20       100                   0.12715   0.02905
50       100                   0.12600   0.02905
20       200                   0.10310   0.02905
50       200                   0.08255   0.02905
CAPACITA*CURRENT
20       3                     0.06415   0.02905
50       3                     0.04970   0.02905
20       5                     0.16610   0.02905
50       5                     0.15885   0.02905
VOLTAGE*CURRENT
100      3                     0.06805   0.02905
200      3                     0.04580   0.02905
100      5                     0.18510   0.02905
200      5                     0.13985   0.02905
CAPACITA*VOLTAGE*CURRENT
20       100      3            0.06710   0.04108
50       100      3            0.06900   0.04108
20       200      3            0.06120   0.04108
50       200      3            0.03040   0.04108
20       100      5            0.18720   0.04108
50       100      5            0.18300   0.04108
20       200      5            0.14500   0.04108
50       200      5            0.13470   0.04108

Mean for Center Point =   0.13507
```

Fractional Factorial Fit: VOID CONTENT versus CAPACITANCE, VOLTAGE, CURRENT

Estimated Effects and Coefficients for VOID (coded units)

Term	Effect	Coef	SE Coef	T	P
Constant		2.0375	0.03536	57.63	0.000
CAPACITA	0.1750	0.0875	0.03536	2.47	0.132
VOLTAGE	0.1250	0.0625	0.03536	1.77	0.219
CURRENT	-0.0250	-0.0125	0.03536	-0.35	0.757
CAPACITA*VOLTAGE	-0.1750	-0.0875	0.03536	-2.47	0.132
CAPACITA*CURRENT	-0.1250	-0.0625	0.03536	-1.77	0.219
VOLTAGE*CURRENT	0.0250	0.0125	0.03536	0.35	0.757
CAPACITA*VOLTAGE*CURRENT	0.1250	0.0625	0.03536	1.77	0.219
Ct Pt		-0.4375	0.06770	-6.46	0.023

Analysis of Variance for VOID (coded units)

Source	DF	Seq SS	Adj SS	Adj MS	F	P
Main Effects	3	0.093750	0.093750	0.03125	3.13	0.252
2-Way Interactions	3	0.093750	0.093750	0.03125	3.12	0.252
3-Way Interactions	1	0.031250	0.031250	0.03125	3.12	0.219
Curvature	1	0.417614	0.417614	0.41761	41.76	0.023
Residual Error	2	0.020000	0.020000	0.01000		
Pure Error	2	0.020000	0.020000	0.01000		
Total	10	0.656364				

Observations for VOID

Obs	VOID CON	Fit	SE Fit	Residual	St Resid	
1	1.70000	1.70000	0.10000	0.00000	*	X
2	2.30000	2.30000	0.10000	-0.00000	*	X
3	2.10000	2.10000	0.10000	0.00000	*	X
4	2.10000	2.10000	0.10000	-0.00000	*	X
5	1.90000	1.90000	0.10000	0.00000	*	X
6	2.00000	2.00000	0.10000	-0.00000	*	X
7	2.10000	2.10000	0.10000	0.00000	*	X
8	2.10000	2.10000	0.10000	-0.00000	*	X
9	1.50000	1.60000	0.05774	-0.10000	-1.22	
10	1.60000	1.60000	0.05774	0.00000	0.00	
11	1.70000	1.60000	0.05774	0.10000	1.22	

X denotes an observation whose X value gives it large influence.

Estimated Coefficients for VOID using data in uncoded units

Term	Coef
Constant	-1.10000
CAPACITA	0.0900000
VOLTAGE	0.0160000
CURRENT	0.533333
CAPACITA*VOLTAGE	-0.000450000
CAPACITA*CURRENT	-0.0166667
VOLTAGE*CURRENT	-0.00266667
CAPACITA*VOLTAGE*CURRENT	0.0000833333
Ct Pt	-0.437500

Least Squares Means for VOID CON

		Mean	SE Mean
CAPACITA			
20		1.950	0.05000
50		2.125	0.05000
VOLTAGE			
100		1.975	0.05000
200		2.100	0.05000
CURRENT			
3		2.050	0.05000
5		2.025	0.05000
CAPACITA*VOLTAGE			
20	100	1.800	0.07071
50	100	2.150	0.07071
20	200	2.100	0.07071
50	200	2.100	0.07071
CAPACITA*CURRENT			
20	3	1.900	0.07071
50	3	2.200	0.07071

20	5		2.000	0.07071
50	5		2.050	0.07071
VOLTAGE*CURRENT				
100	3		2.000	0.07071
200	3		2.100	0.07071
100	5		1.950	0.07071
200	5		2.100	0.07071
CAPACITA*VOLTAGE*CURRENT				
20	100	3	1.700	0.10000
50	100	3	2.300	0.10000
20	200	3	2.100	0.10000
50	200	3	2.100	0.10000
20	100	5	1.900	0.10000
50	100	5	2.000	0.10000
20	200	5	2.100	0.10000
50	200	5	2.100	0.10000

Mean for Center Point = 1.600

Fractional Factorial Fit: CRACK DENSITY versus CAPACITANCE, VOLTAGE, CURRENT

Estimated Effects and Coefficients for CRACK (coded units)

Term	Effect	Coef	SE Coef	T	P
Constant		0.002354	0.000089	26.57	0.001
CAPACITA	0.000542	0.000271	0.000089	3.06	0.092
VOLTAGE	0.000527	0.000264	0.000089	2.98	0.097
CURRENT	0.000648	0.000324	0.000089	3.65	0.067
CAPACITA*VOLTAGE	-0.000367	-0.000184	0.000089	-2.07	0.174
CAPACITA*CURRENT	0.000112	0.000056	0.000089	0.63	0.590
VOLTAGE*CURRENT	-0.000092	-0.000046	0.000089	-0.52	0.654
CAPACITA*VOLTAGE*CURRENT	0.000203	0.000101	0.000089	1.14	0.371
Ct Pt		0.001046	0.000170	6.17	0.025

Analysis of Variance for CRACK (coded units)

Source	DF	Seq SS	Adj SS	Adj MS	F	P
Main Effects	3	0.00000198	0.00000198	0.00000066	10.53	0.088
2-Way Interactions	3	0.00000031	0.00000031	0.00000010	1.66	0.398
3-Way Interactions	1	0.00000008	0.00000008	0.00000008	1.31	0.371
Curvature	1	0.00000239	0.00000239	0.00000239	38.03	0.025
Residual Error	2	0.00000013	0.00000013	0.00000006		
Pure Error	2	0.00000013	0.00000013	0.00000006		
Total	10	0.00000489				

Observations for CRACK DE

Obs	CRACK DE	Fit	SE Fit	Residual	St Resid	
1	0.001220	0.001220	0.000251	0.000000	*	X
2	0.002220	0.002220	0.000251	0.000000	*	X
3	0.002410	0.002410	0.000251	0.000000	*	X
4	0.002270	0.002270	0.000251	-0.000000	*	X
5	0.002050	0.002050	0.000251	0.000000	*	X
6	0.002870	0.002870	0.000251	-0.000000	*	X
7	0.002650	0.002650	0.000251	0.000000	*	X
8	0.003140	0.003140	0.000251	-0.000000	*	X
9	0.003420	0.003400	0.000145	0.000020	0.10	
10	0.003140	0.003400	0.000145	-0.000260	-1.27	
11	0.003640	0.003400	0.000145	0.000240	1.17	

X denotes an observation whose X value gives it large influence.

Estimated Coefficients for CRACK using data in uncoded units

Term	Coef
Constant	-0.00451667
CAPACITA	0.000120833
VOLTAGE	0.0000364500
CURRENT	0.00104000
CAPACITA*VOLTAGE	-7.85000E-07
CAPACITA*CURRENT	-1.65000E-05
VOLTAGE*CURRENT	-5.65000E-06
CAPACITA*VOLTAGE*CURRENT	1.350000E-07
Ct Pt	0.00104625

Least Squares Means for CRACK DE

			Mean	SE Mean
CAPACITA				
20			0.002083	0.000125
50			0.002625	0.000125
VOLTAGE				
100			0.002090	0.000125
200			0.002617	0.000125
CURRENT				
3			0.002030	0.000125
5			0.002678	0.000125
CAPACITA*VOLTAGE				
20	100		0.001635	0.000177
50	100		0.002545	0.000177
20	200		0.002530	0.000177
50	200		0.002705	0.000177
CAPACITA*CURRENT				
20	3		0.001815	0.000177
50	3		0.002245	0.000177
20	5		0.002350	0.000177
50	5		0.003005	0.000177
VOLTAGE*CURRENT				
100	3		0.001720	0.000177
200	3		0.002340	0.000177
100	5		0.002460	0.000177
200	5		0.002895	0.000177
CAPACITA*VOLTAGE*CURRENT				
20	100	3	0.001220	0.000251
50	100	3	0.002220	0.000251
20	200	3	0.002410	0.000251
50	200	3	0.002270	0.000251
20	100	5	0.002050	0.000251
50	100	5	0.002870	0.000251
20	200	5	0.002650	0.000251
50	200	5	0.003140	0.000251

Mean for Center Point = 0.003400

Alias Structure

I
CAPACITA
VOLTAGE
CURRENT

CAPACITA*VOLTAGE
CAPACITA*CURRENT
VOLTAGE*CURRENT
CAPACITA*VOLTAGE*CURRENT

REDUCED MODELS

Fractional Factorial Fit: DEPOSITION RATE versus CURRENT

Estimated Effects and Coefficients for DEPOSITI (coded units)

Term	Effect	Coef	SE Coef	T	P
Constant		0.11662	0.008910	13.09	0.000
CURRENT	0.10555	0.05277	0.010448	5.05	0.001

Analysis of Variance for DEPOSITI (coded units)

Source	DF	Seq SS	Adj SS	Adj MS	F	P
Main Effects	1	0.022282	0.022282	0.0222816	25.51	0.001
Residual Error	9	0.007860	0.007860	0.0008734		
Curvature	1	0.001404	0.001404	0.0014039	1.74	0.224
Pure Error	8	0.006456	0.006456	0.0008070		
Total	10	0.030142				

Observations for DEPOSITI

Obs	DEPOSITI	Fit	SE Fit	Residual	St Resid
1	0.067100	0.063843	0.013732	0.003257	0.12
2	0.069000	0.063843	0.013732	0.005157	0.20
3	0.061200	0.063843	0.013732	-0.002643	-0.10
4	0.030400	0.063843	0.013732	-0.033443	-1.28
5	0.187200	0.169393	0.013732	0.017807	0.68
6	0.183000	0.169393	0.013732	0.013607	0.52
7	0.145000	0.169393	0.013732	-0.024393	-0.93
8	0.134700	0.169393	0.013732	-0.034693	-1.33
9	0.097600	0.116618	0.008910	-0.019018	-0.67
10	0.179000	0.116618	0.008910	0.062382	2.21R
11	0.128600	0.116618	0.008910	0.011982	0.43

R denotes an observation with a large standardized residual

Estimated Coefficients for DEPOSITI using data in uncoded units

Term	Coef
Constant	-0.0944818
CURRENT	0.0527750

Least Squares Means for DEPOSITI

	Mean	SE Mean
CURRENT		
3	0.06384	0.01373
5	0.16939	0.01373

Mean for Center Point = 0.13507

Alias Structure

I
CURRENT

INCONEL 718

Fractional Factorial Fit: DEPOSITION RATE, VOID CONTENT, CRACK DENSITY

Fractional Factorial Fit: DEPOSITION RATE versus CAPACITANCE, VOLTAGE, CURRENT

Estimated Effects and Coefficients for DEPOSITI (coded units)

Term	Effect	Coef	SE Coef	T	P
Constant		0.29610	0.02013	14.71	0.001
CAPACITA	0.09992	0.04996	0.02360	2.12	0.125
VOLTAGE	0.17407	0.08704	0.02360	3.69	0.035
CURRENT	0.23993	0.11996	0.02360	5.08	0.015
CAPACITA*VOLTAGE	-0.06322	-0.03161	0.02360	-1.34	0.273
CAPACITA*CURRENT	0.01603	0.00801	0.02360	0.34	0.757
VOLTAGE*CURRENT	0.05477	0.02739	0.02360	1.16	0.330
CAPACITA*VOLTAGE*CURRENT	-0.06882	-0.03441	0.02360	-1.46	0.241

Analysis of Variance for DEPOSITI (coded units)

Source	DF	Seq SS	Adj SS	Adj MS	F	P
Main Effects	3	0.195702	0.195702	0.0652341	14.64	0.027
2-Way Interactions	3	0.014509	0.014509	0.0048363	1.09	0.474
3-Way Interactions	1	0.009474	0.009474	0.0094738	2.13	0.241
Residual Error	3	0.013368	0.013368	0.0044560		
Curvature	1	0.012982	0.012982	0.0129822	67.31	0.015
Pure Error	2	0.000386	0.000386	0.0001929		
Total	10	0.233053				

Observations for DEPOSITI

Obs	DEPOSITI	Fit	SE Fit	Residual	St Resid
1	0.056300	0.077337	0.065606	-0.021037	-1.71
2	0.134600	0.155637	0.065606	-0.021037	-1.71
3	0.170000	0.191038	0.065606	-0.021038	-1.71
4	0.259500	0.280537	0.065606	-0.021037	-1.71
5	0.156600	0.177637	0.065606	-0.021037	-1.71
6	0.404600	0.425637	0.065606	-0.021037	-1.71
7	0.517500	0.538537	0.065606	-0.021037	-1.71
8	0.501400	0.522437	0.065606	-0.021037	-1.71
9	0.366900	0.296100	0.020127	0.070800	1.11
10	0.350400	0.296100	0.020127	0.054300	0.85
11	0.339300	0.296100	0.020127	0.043200	0.68

Estimated Coefficients for DEPOSITI using data in uncoded units

Term	Coef
Constant	0.584254
CAPACITA	-0.0200133
VOLTAGE	-0.00539867
CURRENT	-0.221783
CAPACITA*VOLTAGE	0.000141383
CAPACITA*CURRENT	0.00741667
VOLTAGE*CURRENT	0.00215367
CAPACITA*VOLTAGE*CURRENT	-4.58833E-05

Least Squares Means for DEPOSITI

			Mean	SE Mean
CAPACITA				
20			0.24614	0.03102
50			0.34606	0.03102
VOLTAGE				
100			0.20906	0.03102
200			0.38314	0.03102
CURRENT				
3			0.17614	0.03102
5			0.41606	0.03102
CAPACITA*VOLTAGE				
20	100		0.12749	0.04556
50	100		0.29064	0.04556
20	200		0.36479	0.04556
50	200		0.40149	0.04556
CAPACITA*CURRENT				
20	3		0.13419	0.04556
50	3		0.21809	0.04556
20	5		0.35809	0.04556
50	5		0.47404	0.04556
VOLTAGE*CURRENT				
100	3		0.11649	0.04556
200	3		0.23579	0.04556
100	5		0.30164	0.04556
200	5		0.53049	0.04556
CAPACITA*VOLTAGE*CURRENT				
20	100	3	0.07734	0.06561
50	100	3	0.15564	0.06561
20	200	3	0.19104	0.06561
50	200	3	0.28054	0.06561
20	100	5	0.17764	0.06561
50	100	5	0.42564	0.06561
20	200	5	0.53854	0.06561
50	200	5	0.52244	0.06561

Mean for Center Point = 0.35220

Fractional Factorial Fit: VOID CONTENT versus CAPACITANCE, VOLTAGE, CURRENT

Estimated Effects and Coefficients for VOID (coded units)

Term	Effect	Coef	SE Coef	T	P
Constant		2.6091	0.2292	11.38	0.001
CAPACITA	-0.9000	-0.4500	0.2688	-1.67	0.193
VOLTAGE	-1.0500	-0.5250	0.2688	-1.95	0.146
CURRENT	-1.1000	-0.5500	0.2688	-2.05	0.133
CAPACITA*VOLTAGE	0.4000	0.2000	0.2688	0.74	0.511
CAPACITA*CURRENT	0.8500	0.4250	0.2688	1.58	0.212
VOLTAGE*CURRENT	0.9000	0.4500	0.2688	1.67	0.193
CAPACITA*VOLTAGE*CURRENT	-1.2500	-0.6250	0.2688	-2.33	0.103

Analysis of Variance for VOID (coded units)

Source	DF	Seq SS	Adj SS	Adj MS	F	P
Main Effects	3	6.2450	6.24500	2.0817	3.60	0.160
2-Way Interactions	3	3.3850	3.38500	1.1283	1.95	0.298
3-Way Interactions	1	3.1250	3.12500	3.1250	5.41	0.103

Residual Error	3	1.7341	1.73409	0.5780		
Curvature	1	0.8074	0.80742	0.8074	1.74	0.318
Pure Error	2	0.9267	0.92667	0.4633		
Total	10	14.4891				

Observations for VOID CON

Obs	VOID CON	Fit	SE Fit	Residual	St Resid
1	6.00000	5.83409	0.74721	0.16591	1.18
2	2.60000	2.43409	0.74721	0.16591	1.18
3	2.40000	2.23409	0.74721	0.16591	1.18
4	2.30000	2.13409	0.74721	0.16591	1.18
5	1.90000	1.73409	0.74721	0.16591	1.18
6	2.70000	2.53409	0.74721	0.16591	1.18
7	2.60000	2.43409	0.74721	0.16591	1.18
8	1.70000	1.53409	0.74721	0.16591	1.18
9	2.40000	2.60909	0.22923	-0.20909	-0.29
10	1.40000	2.60909	0.22923	-1.20909	-1.67
11	2.70000	2.60909	0.22923	0.09091	0.13

Estimated Coefficients for VOID using data in uncoded units

Term	Coef
Constant	35.7008
CAPACITA	-0.683333
VOLTAGE	-0.172500
CURRENT	-7.26667
CAPACITA*VOLTAGE	0.00360000
CAPACITA*CURRENT	0.153333
VOLTAGE*CURRENT	0.0381667
CAPACITA*VOLTAGE*CURRENT	-0.000833333

Least Squares Means for VOID CON

			Mean	SE Mean
CAPACITA				
20			3.059	0.3533
50			2.159	0.3533
VOLTAGE				
100			3.134	0.3533
200			2.084	0.3533
CURRENT				
3			3.159	0.3533
5			2.059	0.3533
CAPACITA*VOLTAGE				
20	100		3.784	0.5190
50	100		2.484	0.5190
20	200		2.334	0.5190
50	200		1.834	0.5190
CAPACITA*CURRENT				
20	3		4.034	0.5190
50	3		2.284	0.5190
20	5		2.084	0.5190
50	5		2.034	0.5190
VOLTAGE*CURRENT				
100	3		4.134	0.5190
200	3		2.184	0.5190
100	5		2.134	0.5190
200	5		1.984	0.5190
CAPACITA*VOLTAGE*CURRENT				
20	100	3	5.834	0.7472

50	100	3	2.434	0.7472
20	200	3	2.234	0.7472
50	200	3	2.134	0.7472
20	100	5	1.734	0.7472
50	100	5	2.534	0.7472
20	200	5	2.434	0.7472
50	200	5	1.534	0.7472

Mean for Center Point = 2.167

Fractional Factorial Fit: CRACK DENSITY versus CAPACITANCE, VOLTAGE, CURRENT

Estimated Effects and Coefficients for CRACK (coded units)

Term	Effect	Coef	SE Coef	T	P
Constant		0.009500	0.001519	6.26	0.008
CAPACITA	-0.001470	-0.000735	0.001781	-0.41	0.708
VOLTAGE	0.001485	0.000742	0.001781	0.42	0.705
CURRENT	0.002695	0.001348	0.001781	0.76	0.504
CAPACITA*VOLTAGE	0.000420	0.000210	0.001781	0.12	0.914
CAPACITA*CURRENT	0.000510	0.000255	0.001781	0.14	0.895
VOLTAGE*CURRENT	0.003465	0.001732	0.001781	0.97	0.402
CAPACITA*VOLTAGE*CURRENT	-0.001760	-0.000880	0.001781	-0.49	0.655

Analysis of Variance for CRACK (coded units)

Source	DF	Seq SS	Adj SS	Adj MS	F	P
Main Effects	3	0.00002326	0.00002326	0.00000775	0.31	0.822
2-Way Interactions	3	0.00002489	0.00002489	0.00000830	0.33	0.808
3-Way Interactions	1	0.00000620	0.00000620	0.00000620	0.24	0.655
Residual Error	3	0.00007612	0.00007612	0.00002537		
Curvature	1	0.00007533	0.00007533	0.00007533	190.50	0.005
Pure Error	2	0.00000079	0.00000079	0.00000040		
Total	10	0.00013046				

Observations for CRACK DE

Obs	CRACK DE	Fit	SE Fit	Residual	St Resid
1	0.009620	0.011223	0.004951	-0.001603	-1.72
2	0.005460	0.007063	0.004951	-0.001603	-1.72
3	0.005460	0.007063	0.004951	-0.001603	-1.72
4	0.005660	0.007262	0.004951	-0.001602	-1.72
5	0.006580	0.008183	0.004951	-0.001603	-1.72
6	0.006960	0.008562	0.004951	-0.001602	-1.72
7	0.012870	0.014473	0.004951	-0.001603	-1.72
8	0.010570	0.012172	0.004951	-0.001602	-1.72
9	0.014080	0.009500	0.001519	0.004580	0.95
10	0.014190	0.009500	0.001519	0.004690	0.98
11	0.013050	0.009500	0.001519	0.003550	0.74

Estimated Coefficients for CRACK using data in uncoded units

Term	Coef
Constant	0.0528775
CAPACITA	-0.00086300
VOLTAGE	-0.000297817
CURRENT	-0.0106050
CAPACITA*VOLTAGE	4.973333E-06

```
CAPACITA*CURRENT           0.000193000
VOLTAGE*CURRENT          0.0000757167
CAPACITA*VOLTAGE*CURRENT -1.17333E-06

Least Squares Means for CRACK DE

                                  Mean   SE Mean
CAPACITA
20                            0.010235  0.002341
50                            0.008765  0.002341
VOLTAGE
100                           0.008758  0.002341
200                           0.010243  0.002341
CURRENT
3                             0.008153  0.002341
5                             0.010848  0.002341
CAPACITA*VOLTAGE
20       100                  0.009703  0.003438
50       100                  0.007813  0.003438
20       200                  0.010768  0.003438
50       200                  0.009718  0.003438
CAPACITA*CURRENT
20       3                    0.009143  0.003438
50       3                    0.007163  0.003438
20       5                    0.011327  0.003438
50       5                    0.010368  0.003438
VOLTAGE*CURRENT
100      3                    0.009143  0.003438
200      3                    0.007163  0.003438
100      5                    0.008373  0.003438
200      5                    0.013323  0.003438
CAPACITA*VOLTAGE*CURRENT
20       100      3           0.011223  0.004951
50       100      3           0.007063  0.004951
20       200      3           0.007063  0.004951
50       200      3           0.007263  0.004951
20       100      5           0.008182  0.004951
50       100      5           0.008563  0.004951
20       200      5           0.014473  0.004951
50       200      5           0.012173  0.004951

Mean for Center Point =  0.013773

Alias Structure

I
CAPACITA
VOLTAGE
CURRENT
CAPACITA*VOLTAGE
CAPACITA*CURRENT
VOLTAGE*CURRENT
CAPACITA*VOLTAGE*CURRENT
```

INCONEL 722

Fractional Factorial Fit: DEPOSITION RATE versus CAPACITANCE, VOLTAGE, CURRENT

Estimated Effects and Coefficients for DEPOSITION (coded units)

Term	Effect	Coef	SE Coef	T	P
Constant		0.32235	0.01179	27.35	0.001
CAPACITA	0.04715	0.02357	0.01179	2.00	0.183
VOLTAGE	0.29120	0.14560	0.01179	12.35	0.006
CURRENT	0.24435	0.12218	0.01179	10.37	0.009
CAPACITA*VOLTAGE	-0.04635	-0.02317	0.01179	-1.97	0.188
CAPACITA*CURRENT	0.02210	0.01105	0.01179	0.94	0.447
VOLTAGE*CURRENT	0.15565	0.07782	0.01179	6.60	0.022
CAPACITA*VOLTAGE*CURRENT	0.00500	0.00250	0.01179	0.21	0.852
Ct Pt		-0.03412	0.02257	-1.51	0.270

Analysis of Variance for DEPOSITION (coded units)

Source	DF	Seq SS	Adj SS	Adj MS	F	P
Main Effects	3	0.293455	0.293455	0.0978183	88.01	0.011
2-Way Interactions	3	0.053727	0.053727	0.0179091	16.11	0.059
3-Way Interactions	1	0.000050	0.000050	0.0000500	0.04	0.852
Curvature	1	0.002540	0.002540	0.0025395	2.28	0.270
Residual Error	2	0.002223	0.002223	0.0011114		
Pure Error	2	0.002223	0.002223	0.0011114		
Total	10	0.351995				

Unusual Observations for DEPOSITION

Obs	DEP	Fit	SE Fit	Residual	St Resid
1	0.094200	0.094200	0.033338	0.000000	* X
2	0.170600	0.170600	0.033338	-0.000000	* X
3	0.281100	0.281100	0.033338	0.000000	* X
4	0.254800	0.254800	0.033338	-0.000000	* X
5	0.165800	0.165800	0.033338	0.000000	* X
6	0.276400	0.276400	0.033338	-0.000000	* X
7	0.654000	0.654000	0.033338	0.000000	* X
8	0.681900	0.681900	0.033338	0.000000	* X

X denotes an observation whose X value gives it large influence.

Estimated Coefficients for DEPOSITION using data in uncoded units

Term	Coef
Constant	0.146650
CAPACITA	0.0052600
VOLTAGE	-0.00176583
CURRENT	-0.119583
CAPACITA*VOLTAGE	-4.42333E-05
CAPACITA*CURRENT	0.00023667
VOLTAGE*CURRENT	0.00143983
CAPACITA*VOLTAGE*CURRENT	0.0000033333
Ct Pt	-0.0341167

Least Squares Means for DEP

	Mean	SE Mean
CAPACITA		

20			0.29877	0.01667
50			0.34593	0.01667
VOLTAGE				
100			0.17675	0.01667
200			0.46795	0.01667
CURRENT				
3			0.20017	0.01667
5			0.44452	0.01667
CAPACITA*VOLTAGE				
20	100		0.13000	0.02357
50	100		0.22350	0.02357
20	200		0.46755	0.02357
50	200		0.46835	0.02357
CAPACITA*CURRENT				
20	3		0.18765	0.02357
50	3		0.21270	0.02357
20	5		0.40990	0.02357
50	5		0.47915	0.02357
VOLTAGE*CURRENT				
100	3		0.13240	0.02357
200	3		0.26795	0.02357
100	5		0.22110	0.02357
200	5		0.66795	0.02357
CAPACITA*VOLTAGE*CURRENT				
20	100	3	0.09420	0.03334
50	100	3	0.17060	0.03334
20	200	3	0.28110	0.03334
50	200	3	0.25480	0.03334
20	100	5	0.16580	0.03334
50	100	5	0.27640	0.03334
20	200	5	0.65400	0.03334
50	200	5	0.68190	0.03334

Mean for Center Point = 0.28823

Fractional Factorial Fit: VOID CONTENT versus CAPACITANCE, VOLTAGE, CURRENT

Estimated Effects and Coefficients for VOID CONTENT (coded units)

Term	Effect	Coef	SE Coef	T	P
Constant		5.975	0.2151	27.78	0.001
CAPACITA	2.400	1.200	0.2151	5.58	0.031
VOLTAGE	3.050	1.525	0.2151	7.09	0.019
CURRENT	4.050	2.025	0.2151	9.42	0.011
CAPACITA*VOLTAGE	1.700	0.850	0.2151	3.95	0.058
CAPACITA*CURRENT	2.600	1.300	0.2151	6.04	0.026
VOLTAGE*CURRENT	2.150	1.075	0.2151	5.00	0.038
CAPACITA*VOLTAGE*CURRENT	2.700	1.350	0.2151	6.28	0.024
Ct Pt		-2.275	0.4118	-5.52	0.031

Analysis of Variance for VOID (coded units)

Source	DF	Seq SS	Adj SS	Adj MS	F	P
Main Effects	3	62.930	62.9300	20.9767	56.69	0.017
2-Way Interactions	3	28.545	28.5450	9.5150	25.72	0.038
3-Way Interactions	1	14.580	14.5800	14.5800	39.41	0.024
Curvature	1	11.292	11.2923	11.2923	30.52	0.031
Residual Error	2	0.740	0.7400	0.3700		
Pure Error	2	0.740	0.7400	0.3700		

Total	10	118.087	

Unusual Observations for VOID

Obs	VOID	Fit	SE Fit	Residual	St Resid
1	3.1000	3.1000	0.6083	0.0000	* X
2	3.9000	3.9000	0.6083	-0.0000	* X
3	5.0000	5.0000	0.6083	0.0000	* X
4	3.8000	3.8000	0.6083	-0.0000	* X
5	5.1000	5.1000	0.6083	0.0000	* X
6	5.7000	5.7000	0.6083	-0.0000	* X
7	5.9000	5.9000	0.6083	0.0000	* X
8	15.3000	15.3000	0.6083	0.0000	* X

X denotes an observation whose X value gives it large influence.

Estimated Coefficients for VOID using data in uncoded units

Term	Coef
Constant	-16.3167
CAPACITA	0.643333
VOLTAGE	0.156833
CURRENT	5.21667
CAPACITA*VOLTAGE	-0.00606667
CAPACITA*CURRENT	-0.183333
VOLTAGE*CURRENT	-0.0415000
CAPACITA*VOLTAGE*CURRENT	0.00180000
Ct Pt	-2.27500

Least Squares Means for VOID

			Mean	SE Mean
CAPACITA				
20			4.775	0.3041
50			7.175	0.3041
VOLTAGE				
100			4.450	0.3041
200			7.500	0.3041
CURRENT				
3			3.950	0.3041
5			8.000	0.3041
CAPACITA*VOLTAGE				
20	100		4.100	0.4301
50	100		4.800	0.4301
20	200		5.450	0.4301
50	200		9.550	0.4301
CAPACITA*CURRENT				
20	3		4.050	0.4301
50	3		3.850	0.4301
20	5		5.500	0.4301
50	5		10.500	0.4301
VOLTAGE*CURRENT				
100	3		3.500	0.4301
200	3		4.400	0.4301
100	5		5.400	0.4301
200	5		10.600	0.4301
CAPACITA*VOLTAGE*CURRENT				
20	100	3	3.100	0.6083
50	100	3	3.900	0.6083
20	200	3	5.000	0.6083
50	200	3	3.800	0.6083

20	100	5	5.100	0.6083
50	100	5	5.700	0.6083
20	200	5	5.900	0.6083
50	200	5	15.300	0.6083

Mean for Center Point = 3.700

Fractional Factorial Fit: CRACK DENSITY versus CAPACITANCE, VOLTAGE, CURRENT

Estimated Effects and Coefficients for CRACK DENSITY (coded units)

Term	Effect	Coef	SE Coef	T	P
Constant		0.006255	0.000540	11.58	0.007
CAPACITA	0.000135	0.000068	0.000540	0.12	0.912
VOLTAGE	0.001995	0.000997	0.000540	1.85	0.206
CURRENT	-0.001240	-0.000620	0.000540	-1.15	0.370
CAPACITA*VOLTAGE	0.002800	0.001400	0.000540	2.59	0.122
CAPACITA*CURRENT	0.000705	0.000353	0.000540	0.65	0.581
VOLTAGE*CURRENT	-0.001495	-0.000747	0.000540	-1.38	0.301
CAPACITA*VOLTAGE*CURRENT	0.003750	0.001875	0.000540	3.47	0.074
Ct Pt		0.000598	0.001034	0.58	0.621

Analysis of Variance for CRACK (coded units)

Source	DF	Seq SS	Adj SS	Adj MS	F	P
Main Effects	3	0.00001107	0.00001107	0.00000369	1.58	0.410
2-Way Interactions	3	0.00002114	0.00002114	0.00000705	3.02	0.259
3-Way Interactions	1	0.00002813	0.00002813	0.00002813	12.05	0.074
Curvature	1	0.00000078	0.00000078	0.00000078	0.33	0.621
Residual Error	2	0.00000467	0.00000467	0.00000233		
Pure Error	2	0.00000467	0.00000467	0.00000233		
Total	10	0.00006579				

Unusual Observations for CRACK

Obs	CRACK	Fit	SE Fit	Residual	St Resid
1	0.004940	0.004940	0.001528	0.000000	* X
2	0.005320	0.005320	0.001528	0.000000	* X
3	0.009380	0.009380	0.001528	0.000000	* X
4	0.007860	0.007860	0.001528	-0.000000	* X
5	0.008240	0.008240	0.001528	0.000000	* X
6	0.002530	0.002530	0.001528	-0.000000	* X
7	0.002190	0.002190	0.001528	0.000000	* X
8	0.009580	0.009580	0.001528	-0.000000	* X

X denotes an observation whose X value gives it large influence.

Estimated Coefficients for CRACK using data in uncoded units

Term	Coef
Constant	-0.0427950
CAPACITA	0.00113050
VOLTAGE	0.000364417
CURRENT	0.0139250
CAPACITA*VOLTAGE	-8.13333E-06
CAPACITA*CURRENT	-0.000351500
VOLTAGE*CURRENT	-0.000102450
CAPACITA*VOLTAGE*CURRENT	2.500000E-06
Ct Pt	0.00059833

Least Squares Means for CRACK

			Mean	SE Mean
CAPACITA				
20			0.006188	0.000764
50			0.006323	0.000764
VOLTAGE				
100			0.005258	0.000764
200			0.007253	0.000764
CURRENT				
3			0.006875	0.000764
5			0.005635	0.000764
CAPACITA*VOLTAGE				
20	100		0.006590	0.001080
50	100		0.003925	0.001080
20	200		0.005785	0.001080
50	200		0.008720	0.001080
CAPACITA*CURRENT				
20	3		0.007160	0.001080
50	3		0.006590	0.001080
20	5		0.005215	0.001080
50	5		0.006055	0.001080
VOLTAGE*CURRENT				
100	3		0.005130	0.001080
200	3		0.008620	0.001080
100	5		0.005385	0.001080
200	5		0.005885	0.001080
CAPACITA*VOLTAGE*CURRENT				
20	100	3	0.004940	0.001528
50	100	3	0.005320	0.001528
20	200	3	0.009380	0.001528
50	200	3	0.007860	0.001528
20	100	5	0.008240	0.001528
50	100	5	0.002530	0.001528
20	200	5	0.002190	0.001528
50	200	5	0.009580	0.001528

Mean for Center Point = 0.006853

Alias Structure

I
CAPACITA
VOLTAGE
CURRENT
CAPACITA*VOLTAGE
CAPACITA*CURRENT
VOLTAGE*CURRENT
CAPACITA*VOLTAGE*CURRENT

REDUCED MODEL

Fractional Factorial Fit: DEPOSITION RATE versus VOLTAGE, CURRENT

Estimated Effects and Coefficients for DEPOSITION RATE (coded units)

Term	Effect	Coef	SE Coef	T	P
Constant		0.31305	0.01374	22.79	0.000

VOLTAGE	0.29120	0.14560	0.01611	9.04	0.000
CURRENT	0.24435	0.12218	0.01611	7.58	0.000
VOLTAGE*CURRENT	0.15565	0.07782	0.01611	4.83	0.002

Analysis of Variance for DEP (coded units)

Source	DF	Seq SS	Adj SS	Adj MS	F	P
Main Effects	2	0.289009	0.289009	0.144504	69.61	0.000
2-Way Interactions	1	0.048454	0.048454	0.048454	23.34	0.002
Residual Error	7	0.014532	0.014532	0.002076		
Curvature	1	0.002540	0.002540	0.002540	1.27	0.303
Pure Error	6	0.011993	0.011993	0.001999		
Total	10	0.351995				

Estimated Coefficients for DEP using data in uncoded units

Term	Coef
Constant	0.321445
VOLTAGE	-0.00331400
CURRENT	-0.111300
VOLTAGE*CURRENT	0.00155650

Least Squares Means for DEP

	Mean	SE Mean
CURRENT		
3	0.1909	0.02117
5	0.4352	0.02117

Mean for Center Point = 0.2882

Alias Structure

I
VOLTAGE
CURRENT
VOLTAGE*CURRENT

INCONEL 738

Fractional Factorial Fit: DEPOSITION RATE, VOID CONTENT, CRACK DENSITY

Fractional Factorial Fit: DEPOSITION R versus CAPACITANCE, VOLTAGE, CURRENT

Estimated Effects and Coefficients for DEPOSITI (coded units)

Term	Effect	Coef	SE Coef	T	P
Constant		0.33356	0.02137	15.61	0.004
CAPACITA	0.14437	0.07219	0.02137	3.38	0.078
VOLTAGE	0.28632	0.14316	0.02137	6.70	0.022
CURRENT	0.32143	0.16071	0.02137	7.52	0.017
CAPACITA*VOLTAGE	0.06438	0.03219	0.02137	1.51	0.271
CAPACITA*CURRENT	0.06818	0.03409	0.02137	1.60	0.252
VOLTAGE*CURRENT	0.10362	0.05181	0.02137	2.42	0.136
CAPACITA*VOLTAGE*CURRENT	0.05538	0.02769	0.02137	1.30	0.324
Ct Pt		0.05340	0.04091	1.31	0.322

Analysis of Variance for DEPOSITI (coded units)

Source	DF	Seq SS	Adj SS	Adj MS	F	P
Main Effects	3	0.412280	0.412280	0.137427	37.63	0.026
2-Way Interactions	3	0.039060	0.039060	0.013020	3.56	0.227
3-Way Interactions	1	0.006133	0.006133	0.006133	1.68	0.324
Curvature	1	0.006223	0.006223	0.006223	1.70	0.322
Residual Error	2	0.007304	0.007304	0.003652		
Pure Error	2	0.007304	0.007304	0.003652		
Total	10	0.471000				

Observations for DEPOSITI

Obs	DEPOSITI	Fit	SE Fit	Residual	St Resid
1	0.047900	0.047900	0.060434	0.000000	* X
2	0.115100	0.115100	0.060434	0.000000	* X
3	0.221600	0.221600	0.060434	0.000000	* X
4	0.306800	0.306800	0.060434	0.000000	* X
5	0.252900	0.252900	0.060434	0.000000	* X
6	0.345700	0.345700	0.060434	0.000000	* X
7	0.523100	0.523100	0.060434	0.000000	* X
8	0.855400	0.855400	0.060434	0.000000	* X
9	0.446200	0.386967	0.034891	0.059233	1.20
10	0.325400	0.386967	0.034891	-0.061567	-1.25
11	0.389300	0.386967	0.034891	0.002333	0.05

X denotes an observation whose X value gives it large influence.

Estimated Coefficients for DEPOSITI using data in uncoded units

Term	Coef
Constant	-0.517250
CAPACITA	0.0114350
VOLTAGE	0.00238450
CURRENT	0.119550
CAPACITA*VOLTAGE	-0.000104750
CAPACITA*CURRENT	-0.00326500
VOLTAGE*CURRENT	-0.00025583
CAPACITA*VOLTAGE*CURRENT	0.0000369167

Ct Pt 0.0534042

Least Squares Means for DEPOSITI

			Mean	SE Mean
CAPACITA				
20			0.26138	0.03022
50			0.40575	0.03022
VOLTAGE				
100			0.19040	0.03022
200			0.47672	0.03022
CURRENT				
3			0.17285	0.03022
5			0.49428	0.03022
CAPACITA*VOLTAGE				
20	100		0.15040	0.04273
50	100		0.23040	0.04273
20	200		0.37235	0.04273
50	200		0.58110	0.04273
CAPACITA*CURRENT				
20	3		0.13475	0.04273
50	3		0.21095	0.04273
20	5		0.38800	0.04273
50	5		0.60055	0.04273
VOLTAGE*CURRENT				
100	3		0.08150	0.04273
200	3		0.26420	0.04273
100	5		0.29930	0.04273
200	5		0.68925	0.04273
CAPACITA*VOLTAGE*CURRENT				
20	100	3	0.04790	0.06043
50	100	3	0.11510	0.06043
20	200	3	0.22160	0.06043
50	200	3	0.30680	0.06043
20	100	5	0.25290	0.06043
50	100	5	0.34570	0.06043
20	200	5	0.52310	0.06043
50	200	5	0.85540	0.06043

Mean for Center Point = 0.38697

Fractional Factorial Fit: VOID CONTENT versus CAPACITANCE, VOLTAGE, CURRENT

Estimated Effects and Coefficients for VOID (coded units)

Term	Effect	Coef	SE Coef	T	P
Constant		2.8250	0.4021	7.03	0.020
CAPACITA	-0.1000	-0.0500	0.4021	-0.12	0.912
VOLTAGE	-0.1000	-0.0500	0.4021	-0.12	0.912
CURRENT	3.1000	1.5500	0.4021	3.85	0.061
CAPACITA*VOLTAGE	-0.1500	-0.0750	0.4021	-0.19	0.869
CAPACITA*CURRENT	0.1500	0.0750	0.4021	0.19	0.869
VOLTAGE*CURRENT	-0.6500	-0.3250	0.4021	-0.81	0.504
CAPACITA*VOLTAGE*CURRENT	0.1000	0.0500	0.4021	0.12	0.912
Ct Pt		1.9083	0.7699	2.48	0.131

Analysis of Variance for VOID (coded units)

Source	DF	Seq SS	Adj SS	Adj MS	F	P
Main Effects	3	19.2600	19.2600	6.42000	4.96	0.172
2-Way Interactions	3	0.9350	0.9350	0.31167	0.24	0.863
3-Way Interactions	1	0.0200	0.0200	0.02000	0.02	0.912
Curvature	1	7.9456	7.9456	7.94561	6.14	0.131
Residual Error	2	2.5867	2.5867	1.29333		
Pure Error	2	2.5867	2.5867	1.29333		
Total	10	30.7473				

Observations for VOID CON

Obs	VOID CON	Fit	SE Fit	Residual	St Resid
1	1.00000	1.00000	1.13725	0.00000	* X
2	1.00000	1.00000	1.13725	0.00000	* X
3	1.80000	1.80000	1.13725	-0.00000	* X
4	1.30000	1.30000	1.13725	-0.00000	* X
5	4.70000	4.70000	1.13725	0.00000	* X
6	4.80000	4.80000	1.13725	0.00000	* X
7	4.00000	4.00000	1.13725	0.00000	* X
8	4.00000	4.00000	1.13725	0.00000	* X
9	3.80000	4.73333	0.65659	-0.93333	-1.01
10	6.00000	4.73333	0.65659	1.26667	1.36
11	4.40000	4.73333	0.65659	-0.33333	-0.36

X denotes an observation whose X value gives it large influence.

Estimated Coefficients for VOID using data in uncoded units

Term	Coef
Constant	-8.2333
CAPACITA	0.031667
VOLTAGE	0.0378333
CURRENT	2.70000
CAPACITA*VOLTAGE	-0.00036667
CAPACITA*CURRENT	-0.0050000
VOLTAGE*CURRENT	-0.0088333
CAPACITA*VOLTAGE*CURRENT	0.000066667
Ct Pt	1.90833

Least Squares Means for VOID CON

		Mean	SE Mean
CAPACITA			
20		2.875	0.5686
50		2.775	0.5686
VOLTAGE			
100		2.875	0.5686
200		2.775	0.5686
CURRENT			
3		1.275	0.5686
5		4.375	0.5686
CAPACITA*VOLTAGE			
20	100	2.850	0.8042
50	100	2.900	0.8042
20	200	2.900	0.8042
50	200	2.650	0.8042
CAPACITA*CURRENT			
20	3	1.400	0.8042
50	3	1.150	0.8042
20	5	4.350	0.8042
50	5	4.400	0.8042

```
VOLTAGE*CURRENT
100      3                    1.000    0.8042
200      3                    1.550    0.8042
100      5                    4.750    0.8042
200      5                    4.000    0.8042
CAPACITA*VOLTAGE*CURRENT
20       100      3           1.000    1.1372
50       100      3           1.000    1.1372
20       200      3           1.800    1.1372
50       200      3           1.300    1.1372
20       100      5           4.700    1.1372
50       100      5           4.800    1.1372
20       200      5           4.000    1.1372
50       200      5           4.000    1.1372

Mean for Center Point =     4.733
```

Fractional Factorial Fit: CRACK DENSITY versus CAPACITANCE, VOLTAGE, CURRENT

Estimated Effects and Coefficients for CRACK (coded units)

Term	Effect	Coef	SE Coef	T	P
Constant		0.005724	0.000552	10.37	0.009
CAPACITA	0.002062	0.001031	0.000552	1.87	0.203
VOLTAGE	0.003777	0.001889	0.000552	3.42	0.076
CURRENT	0.005413	0.002706	0.000552	4.90	0.039
CAPACITA*VOLTAGE	0.002102	0.001051	0.000552	1.90	0.197
CAPACITA*CURRENT	0.002858	0.001429	0.000552	2.59	0.122
VOLTAGE*CURRENT	0.001582	0.000791	0.000552	1.43	0.288
CAPACITA*VOLTAGE*CURRENT	0.002958	0.001479	0.000552	2.68	0.116
Ct Pt		-0.000070	0.001057	-0.07	0.953

Analysis of Variance for CRACK (coded units)

Source	DF	Seq SS	Adj SS	Adj MS	F	P
Main Effects	3	0.00009564	0.00009564	0.00003188	13.08	0.072
2-Way Interactions	3	0.00003018	0.00003018	0.00001006	4.13	0.201
3-Way Interactions	1	0.00001749	0.00001749	0.00001749	7.18	0.116
Curvature	1	0.00000001	0.00000001	0.00000001	0.00	0.953
Residual Error	2	0.00000488	0.00000488	0.00000244		
Pure Error	2	0.00000488	0.00000488	0.00000244		
Total	10	0.00014820				

Observations for CRACK DE

Obs	CRACK DE	Fit	SE Fit	Residual	St Resid
1	0.001890	0.001890	0.001561	0.000000	* X
2	0.001950	0.001950	0.001561	0.000000	* X
3	0.004940	0.004940	0.001561	0.000000	* X
4	0.003290	0.003290	0.001561	0.000000	* X
5	0.005820	0.005820	0.001561	0.000000	* X
6	0.005680	0.005680	0.001561	-0.000000	* X
7	0.006120	0.006120	0.001561	0.000000	* X
8	0.016100	0.016100	0.001561	-0.000000	* X
9	0.006710	0.005653	0.000901	0.001057	0.83
10	0.003860	0.005653	0.000901	-0.001793	-1.41
11	0.006390	0.005653	0.000901	0.000737	0.58

X denotes an observation whose X value gives it large influence.

Estimated Coefficients for CRACK using data in uncoded units

Term	Coef
Constant	-0.0243900
CAPACITA	0.000660500
VOLTAGE	0.000201450
CURRENT	0.00735000
CAPACITA*VOLTAGE	-6.48500E-06
CAPACITA*CURRENT	-0.000200500
VOLTAGE*CURRENT	-5.31833E-05
CAPACITA*VOLTAGE*CURRENT	1.971667E-06
Ct Pt	-0.00007042

Least Squares Means for CRACK DE

			Mean	SE Mean
CAPACITA				
20			0.004693	0.000781
50			0.006755	0.000781
VOLTAGE				
100			0.003835	0.000781
200			0.007612	0.000781
CURRENT				
3			0.003018	0.000781
5			0.008430	0.000781
CAPACITA*VOLTAGE				
20	100		0.003855	0.001104
50	100		0.003815	0.001104
20	200		0.005530	0.001104
50	200		0.009695	0.001104
CAPACITA*CURRENT				
20	3		0.003415	0.001104
50	3		0.002620	0.001104
20	5		0.005970	0.001104
50	5		0.010890	0.001104
VOLTAGE*CURRENT				
100	3		0.001920	0.001104
200	3		0.004115	0.001104
100	5		0.005750	0.001104
200	5		0.011110	0.001104
CAPACITA*VOLTAGE*CURRENT				
20	100	3	0.001890	0.001561
50	100	3	0.001950	0.001561
20	200	3	0.004940	0.001561
50	200	3	0.003290	0.001561
20	100	5	0.005820	0.001561
50	100	5	0.005680	0.001561
20	200	5	0.006120	0.001561
50	200	5	0.016100	0.001561

Mean for Center Point = 0.005653

Alias Structure

I
CAPACITA
VOLTAGE
CURRENT
CAPACITA*VOLTAGE

CAPACITA*CURRENT
VOLTAGE*CURRENT
CAPACITA*VOLTAGE*CURRENT

REDUCED MODELS

Fractional Factorial Fit: DEPOSITION RATE versus CAPACITANCE, VOLTAGE, CURRENT

Estimated Effects and Coefficients for DEPOSITI (coded units)

Term	Effect	Coef	SE Coef	T	P
Constant		0.33356	0.03307	10.09	0.000
CAPACITA	0.14437	0.07219	0.03307	2.18	0.072
VOLTAGE	0.28632	0.14316	0.03307	4.33	0.005
CURRENT	0.32143	0.16071	0.03307	4.86	0.003
Ct Pt		0.05340	0.06333	0.84	0.431

Analysis of Variance for DEPOSITI (coded units)

Source	DF	Seq SS	Adj SS	Adj MS	F	P
Main Effects	3	0.412280	0.412280	0.137427	15.71	0.003
Curvature	1	0.006223	0.006223	0.006223	0.71	0.431
Residual Error	6	0.052497	0.052497	0.008750		
Lack of Fit	4	0.045193	0.045193	0.011298	3.09	0.259
Pure Error	2	0.007304	0.007304	0.003652		
Total	10	0.471000				

Observations for DEPOSITI

Obs	DEPOSITI	Fit	SE Fit	Residual	St Resid
1	0.047900	-0.042500	0.066142	0.090400	1.37
2	0.115100	0.101875	0.066142	0.013225	0.20
3	0.221600	0.243825	0.066142	-0.022225	-0.34
4	0.306800	0.388200	0.066142	-0.081400	-1.23
5	0.252900	0.278925	0.066142	-0.026025	-0.39
6	0.345700	0.423300	0.066142	-0.077600	-1.17
7	0.523100	0.565250	0.066142	-0.042150	-0.64
8	0.855400	0.709625	0.066142	0.145775	2.20R
9	0.446200	0.386967	0.054005	0.059233	0.78
10	0.325400	0.386967	0.054005	-0.061567	-0.81
11	0.389300	0.386967	0.054005	0.002333	0.03

R denotes an observation with a large standardized residual

Estimated Coefficients for DEPOSITI using data in uncoded units

Term	Coef
Constant	-0.907213
CAPACITA	0.00481250
VOLTAGE	0.00286325
CURRENT	0.160712
Ct Pt	0.0534042

Least Squares Means for DEPOSITI

	Mean	SE Mean
CAPACITA		
20	0.2614	0.04677
50	0.4058	0.04677

```
VOLTAGE
100              0.1904    0.04677
200              0.4767    0.04677
CURRENT
3                0.1729    0.04677
5                0.4943    0.04677

Mean for Center Point =     0.3870


Alias Structure

I
CAPACITA
VOLTAGE
CURRENT
```

Fractional Factorial Fit: VOID CONTENT versus CURRENT

Estimated Effects and Coefficients for VOID (coded units)

Term	Effect	Coef	SE Coef	T	P
Constant		3.345	0.3412	9.80	0.000
CURRENT	3.100	1.550	0.4001	3.87	0.004

Analysis of Variance for VOID (coded units)

Source	DF	Seq SS	Adj SS	Adj MS	F	P
Main Effects	1	19.220	19.220	19.2200	15.01	0.004
Residual Error	9	11.527	11.527	1.2808		
Curvature	1	7.946	7.946	7.9456	17.75	0.003
Pure Error	8	3.582	3.582	0.4477		
Total	10	30.747				

Observations for VOID CON

Obs	VOID CON	Fit	SE Fit	Residual	St Resid
1	1.00000	1.79545	0.52587	-0.79545	-0.79
2	1.00000	1.79545	0.52587	-0.79545	-0.79
3	1.80000	1.79545	0.52587	0.00455	0.00
4	1.30000	1.79545	0.52587	-0.49545	-0.49
5	4.70000	4.89545	0.52587	-0.19545	-0.20
6	4.80000	4.89545	0.52587	-0.09545	-0.10
7	4.00000	4.89545	0.52587	-0.89545	-0.89
8	4.00000	4.89545	0.52587	-0.89545	-0.89
9	3.80000	3.34545	0.34123	0.45455	0.42
10	6.00000	3.34545	0.34123	2.65455	2.46R
11	4.40000	3.34545	0.34123	1.05455	0.98

R denotes an observation with a large standardized residual

Estimated Coefficients for VOID using data in uncoded units

Term	Coef
Constant	-2.85455
CURRENT	1.55000

Least Squares Means for VOID CON

	Mean	SE Mean
CURRENT		
3	1.795	0.5259
5	4.895	0.5259

Mean for Center Point = 4.733

Alias Structure

I
CURRENT

Fractional Factorial Fit: CRACK DENSITY versus VOLTAGE, CURRENT

Estimated Effects and Coefficients for CRACK (coded units)

Term	Effect	Coef	SE Coef	T	P
Constant		0.005705	0.000833	6.85	0.000
VOLTAGE	0.003777	0.001889	0.000977	1.93	0.089
CURRENT	0.005413	0.002706	0.000977	2.77	0.024

Analysis of Variance for CRACK (coded units)

Source	DF	Seq SS	Adj SS	Adj MS	F	P
Main Effects	2	0.00008713	0.00008713	0.00004356	5.71	0.029
Residual Error	8	0.00006107	0.00006107	0.00000763		
Curvature	1	0.00000001	0.00000001	0.00000001	0.00	0.973
Lack of Fit	1	0.00000501	0.00000501	0.00000501	0.54	0.492
Pure Error	6	0.00005605	0.00005605	0.00000934		
Total	10	0.00014820				

Observations for CRACK DE

Obs	CRACK DE	Fit	SE Fit	Residual	St Resid
1	0.001890	0.001110	0.001613	0.000780	0.35
2	0.001950	0.001110	0.001613	0.000840	0.37
3	0.004940	0.004887	0.001613	0.000053	0.02
4	0.003290	0.004887	0.001613	-0.001597	-0.71
5	0.005820	0.006522	0.001613	-0.000702	-0.31
6	0.005680	0.006522	0.001613	-0.000842	-0.38
7	0.006120	0.010300	0.001613	-0.004180	-1.86
8	0.016100	0.010300	0.001613	0.005800	2.59R
9	0.006710	0.005705	0.000833	0.001005	0.38
10	0.003860	0.005705	0.000833	-0.001845	-0.70
11	0.006390	0.005705	0.000833	0.000685	0.26

R denotes an observation with a large standardized residual

Estimated Coefficients for CRACK using data in uncoded units

Term	Coef
Constant	-0.0107867
VOLTAGE	0.0000377750
CURRENT	0.00270625

Least Squares Means for CRACK DE

	Mean	SE Mean
VOLTAGE		
100	0.003816	0.001284

```
200             0.007593  0.001284
CURRENT
3               0.002998  0.001284
5               0.008411  0.001284

Mean for Center Point =  0.005653

Alias Structure

I
VOLTAGE
CURRENT
```

KNOOP MICRO HARDNESS (INCONEL738)

Fractional Factorial Fit: KNOOP MICROHARDNESS (HK) versus CAPACITANCE, VOLTAGE, CURRENT

Estimated Effects and Coefficients for HK (coded units)

Term	Effect	Coef	SE Coef	T	P
Constant		425.55	0.5143	827.49	0.000
CAPACITA	-9.50	-4.75	0.6030	-7.88	0.004
VOLTAGE	-9.50	-4.75	0.6030	-7.88	0.004
CURRENT	-24.50	-12.25	0.6030	-20.31	0.000
CAPACITA*VOLTAGE	-11.00	-5.50	0.6030	-9.12	0.003
CAPACITA*CURRENT	3.00	1.50	0.6030	2.49	0.089
VOLTAGE*CURRENT	7.00	3.50	0.6030	5.80	0.010
CAPACITA*VOLTAGE*CURRENT	20.50	10.25	0.6030	17.00	0.000

Analysis of Variance for HK (coded units)

Source	DF	Seq SS	Adj SS	Adj MS	F	P
Main Effects	3	1561.50	1561.50	520.500	178.92	0.001
2-Way Interactions	3	358.00	358.00	119.333	41.02	0.006
3-Way Interactions	1	840.50	840.50	840.500	288.92	0.000
Residual Error	3	8.73	8.73	2.909		
Curvature	1	8.73	8.73	8.727		
Pure Error	2	0.00	0.00	0.000		
Total	10	2768.73				

Observations for HK

Obs	HK	Fit	SE Fit	Residual	St Resid
1	436.000	436.545	1.676	-0.545	-1.73
2	455.000	455.545	1.676	-0.545	-1.73
3	451.000	451.545	1.676	-0.545	-1.73
4	407.000	407.545	1.676	-0.545	-1.73
5	422.000	422.545	1.676	-0.545	-1.73
6	406.000	406.545	1.676	-0.545	-1.73
7	410.000	410.545	1.676	-0.545	-1.73
8	413.000	413.545	1.676	-0.545	-1.73
9	427.000	425.545	0.514	1.455	0.89
10	427.000	425.545	0.514	1.455	0.89
11	427.000	425.545	0.514	1.455	0.89

Estimated Coefficients for HK using data in uncoded units

Term	Coef
Constant	230.379
CAPACITA	8.58333
VOLTAGE	1.79500
CURRENT	45.5000
CAPACITA*VOLTAGE	-0.0620000
CAPACITA*CURRENT	-1.95000
VOLTAGE*CURRENT	-0.408333
CAPACITA*VOLTAGE*CURRENT	0.0136667

Least Squares Means for HK

	Mean	SE Mean
CAPACITA		
20	430.3	0.7925

```
50                                  420.8     0.7925
VOLTAGE
100                                 430.3     0.7925
200                                 420.8     0.7925
CURRENT
3                                   437.8     0.7925
5                                   413.3     0.7925
CAPACITA*VOLTAGE
20        100                       429.5     1.1642
50        100                       431.0     1.1642
20        200                       431.0     1.1642
50        200                       410.5     1.1642
CAPACITA*CURRENT
20        3                         444.0     1.1642
50        3                         431.5     1.1642
20        5                         416.5     1.1642
50        5                         410.0     1.1642
VOLTAGE*CURRENT
100       3                         446.0     1.1642
200       3                         429.5     1.1642
100       5                         414.5     1.1642
200       5                         412.0     1.1642
CAPACITA*VOLTAGE*CURRENT
20        100       3               436.5     1.6763
50        100       3               455.5     1.6763
20        200       3               451.5     1.6763
50        200       3               407.5     1.6763
20        100       5               422.5     1.6763
50        100       5               406.5     1.6763
20        200       5               410.5     1.6763
50        200       5               413.5     1.6763

Mean for Center Point =     427.0

Alias Structure

I
CAPACITA
VOLTAGE
CURRENT
CAPACITA*VOLTAGE
CAPACITA*CURRENT
VOLTAGE*CURRENT
CAPACITA*VOLTAGE*CURRENT
```

RENE 41

Fractional Factorial Fit: DEPOSITION RATE, VOID CONTENT, CRACK DENSITY

Fractional Factorial Fit: DEPOSITION R versus CAPACITANCE, VOLTAGE, CURRENT

Estimated Effects and Coefficients for DEPOSITI (coded units)

Term	Effect	Coef	SE Coef	T	P
Constant		0.25540	0.03634	7.03	0.020
CAPACITA	0.05655	0.02827	0.03634	0.78	0.518
VOLTAGE	0.21995	0.10997	0.03634	3.03	0.094
CURRENT	0.21600	0.10800	0.03634	2.97	0.097
CAPACITA*VOLTAGE	0.03250	0.01625	0.03634	0.45	0.698
CAPACITA*CURRENT	-0.08675	-0.04338	0.03634	-1.19	0.355
VOLTAGE*CURRENT	-0.02355	-0.01178	0.03634	-0.32	0.777
CAPACITA*VOLTAGE*CURRENT	-0.07210	-0.03605	0.03634	-0.99	0.426
Ct Pt		-0.05867	0.06958	-0.84	0.488

Analysis of Variance for DEPOSITI (coded units)

Source	DF	Seq SS	Adj SS	Adj MS	F	P
Main Effects	3	0.196464	0.196464	0.065488	6.20	0.142
2-Way Interactions	3	0.018273	0.018273	0.006091	0.58	0.684
3-Way Interactions	1	0.010397	0.010397	0.010397	0.98	0.426
Curvature	1	0.007509	0.007509	0.007509	0.71	0.488
Residual Error	2	0.021124	0.021124	0.010562		
Pure Error	2	0.021124	0.021124	0.010562		
Total	10	0.253767				

Observations for DEPOSITI

Obs	DEPOSITI	Fit	SE Fit	Residual	St Resid
1	0.006300	0.006300	0.102772	0.000000	* X
2	0.045000	0.045000	0.102772	0.000000	* X
3	0.145200	0.145200	0.102772	-0.000000	* X
4	0.393100	0.393100	0.102772	0.000000	* X
5	0.260500	0.260500	0.102772	0.000000	* X
6	0.269900	0.269900	0.102772	0.000000	* X
7	0.496500	0.496500	0.102772	0.000000	* X
8	0.426700	0.426700	0.102772	0.000000	* X
9	0.194300	0.196733	0.059335	-0.002433	-0.03
10	0.300700	0.196733	0.059335	0.103967	1.24
11	0.095200	0.196733	0.059335	-0.101533	-1.21

X denotes an observation whose X value gives it large influence.

Estimated Coefficients for DEPOSITI using data in uncoded units

Term	Coef
Constant	0.00452
CAPACITA	-0.0186383
VOLTAGE	-0.00434617
CURRENT	-0.007817
CAPACITA*VOLTAGE	0.000213933
CAPACITA*CURRENT	0.00431833
VOLTAGE*CURRENT	0.00144683
CAPACITA*VOLTAGE*CURRENT	-4.80667E-05

Ct Pt -0.0586667

Least Squares Means for DEPOSITI

			Mean	SE Mean
CAPACITA				
20			0.227125	0.05139
50			0.283675	0.05139
VOLTAGE				
100			0.145425	0.05139
200			0.365375	0.05139
CURRENT				
3			0.147400	0.05139
5			0.363400	0.05139
CAPACITA*VOLTAGE				
20	100		0.133400	0.07267
50	100		0.157450	0.07267
20	200		0.320850	0.07267
50	200		0.409900	0.07267
CAPACITA*CURRENT				
20	3		0.075750	0.07267
50	3		0.219050	0.07267
20	5		0.378500	0.07267
50	5		0.348300	0.07267
VOLTAGE*CURRENT				
100	3		0.025650	0.07267
200	3		0.269150	0.07267
100	5		0.265200	0.07267
200	5		0.461600	0.07267
CAPACITA*VOLTAGE*CURRENT				
20	100	3	0.006300	0.10277
50	100	3	0.045000	0.10277
20	200	3	0.145200	0.10277
50	200	3	0.393100	0.10277
20	100	5	0.260500	0.10277
50	100	5	0.269900	0.10277
20	200	5	0.496500	0.10277
50	200	5	0.426700	0.10277

Mean for Center Point = 0.196733

Fractional Factorial Fit: VOID CONTENT versus CAPACITANCE, VOLTAGE, CURRENT

Estimated Effects and Coefficients for VOID (coded units)

Term	Effect	Coef	SE Coef	T	P
Constant		2.7125	0.3240	8.37	0.014
CAPACITA	0.1750	0.0875	0.3240	0.27	0.812
VOLTAGE	0.1750	0.0875	0.3240	0.27	0.812
CURRENT	3.3750	1.6875	0.3240	5.21	0.035
CAPACITA*VOLTAGE	-0.3750	-0.1875	0.3240	-0.58	0.621
CAPACITA*CURRENT	-0.0750	-0.0375	0.3240	-0.12	0.918
VOLTAGE*CURRENT	-0.8750	-0.4375	0.3240	-1.35	0.309
CAPACITA*VOLTAGE*CURRENT	0.3750	0.1875	0.3240	0.58	0.621
Ct Pt		1.8875	0.6205	3.04	0.093

Analysis of Variance for VOID (coded units)

Source	DF	Seq SS	Adj SS	Adj MS	F	P

Main Effects	3	22.9038	22.9038	7.6346	9.09	0.101
2-Way Interactions	3	1.8238	1.8238	0.6079	0.72	0.624
3-Way Interactions	1	0.2813	0.2813	0.2813	0.33	0.621
Curvature	1	7.7731	7.7731	7.7731	9.25	0.093
Residual Error	2	1.6800	1.6800	0.8400		
Pure Error	2	1.6800	1.6800	0.8400		
Total	10	34.4618				

Observations for VOID CON

Obs	VOID CON	Fit	SE Fit	Residual	St Resid
1	0.00000	-0.00000	0.91652	0.00000	* X
2	1.00000	1.00000	0.91652	0.00000	* X
3	1.80000	1.80000	0.91652	0.00000	* X
4	1.30000	1.30000	0.91652	-0.00000	* X
5	4.70000	4.70000	0.91652	-0.00000	* X
6	4.80000	4.80000	0.91652	-0.00000	* X
7	4.00000	4.00000	0.91652	0.00000	* X
8	4.10000	4.10000	0.91652	-0.00000	* X
9	3.80000	4.60000	0.52915	-0.80000	-1.07
10	5.60000	4.60000	0.52915	1.00000	1.34
11	4.40000	4.60000	0.52915	-0.20000	-0.27

X denotes an observation whose X value gives it large influence.

Estimated Coefficients for VOID using data in uncoded units

Term	Coef
Constant	-16.6667
CAPACITA	0.203333
VOLTAGE	0.0805000
CURRENT	4.40000
CAPACITA*VOLTAGE	-0.00125000
CAPACITA*CURRENT	-0.0400000
VOLTAGE*CURRENT	-0.0175000
CAPACITA*VOLTAGE*CURRENT	0.000250000
Ct Pt	1.88750

Least Squares Means for VOID CON

		Mean	SE Mean
CAPACITA			
20		2.62500	0.4583
50		2.80000	0.4583
VOLTAGE			
100		2.62500	0.4583
200		2.80000	0.4583
CURRENT			
3		1.02500	0.4583
5		4.40000	0.4583
CAPACITA*VOLTAGE			
20	100	2.35000	0.6481
50	100	2.90000	0.6481
20	200	2.90000	0.6481
50	200	2.70000	0.6481
CAPACITA*CURRENT			
20	3	0.90000	0.6481
50	3	1.15000	0.6481
20	5	4.35000	0.6481
50	5	4.45000	0.6481
VOLTAGE*CURRENT			

100	3		0.50000	0.6481
200	3		1.55000	0.6481
100	5		4.75000	0.6481
200	5		4.05000	0.6481
CAPACITA*VOLTAGE*CURRENT				
20	100	3	-0.00000	0.9165
50	100	3	1.00000	0.9165
20	200	3	1.80000	0.9165
50	200	3	1.30000	0.9165
20	100	5	4.70000	0.9165
50	100	5	4.80000	0.9165
20	200	5	4.00000	0.9165
50	200	5	4.10000	0.9165

Mean for Center Point = 4.60000

Fractional Factorial Fit: CRACK DENSITY versus CAPACITANCE, VOLTAGE, CURRENT

Estimated Effects and Coefficients for CRACK (coded units)

Term	Effect	Coef	SE Coef	T	P
Constant		0.007494	0.000409	18.33	0.003
CAPACITA	-0.000697	-0.000349	0.000409	-0.85	0.484
VOLTAGE	0.000512	0.000256	0.000409	0.63	0.595
CURRENT	0.000517	0.000259	0.000409	0.63	0.592
CAPACITA*VOLTAGE	0.001937	0.000969	0.000409	2.37	0.141
CAPACITA*CURRENT	0.000723	0.000361	0.000409	0.88	0.470
VOLTAGE*CURRENT	0.000253	0.000126	0.000409	0.31	0.787
CAPACITA*VOLTAGE*CURRENT	-0.002332	-0.001166	0.000409	-2.85	0.104
Ct Pt		0.000276	0.000783	0.35	0.758

Analysis of Variance for CRACK (coded units)

Source	DF	Seq SS	Adj SS	Adj MS	F	P
Main Effects	3	0.00000203	0.00000203	0.00000068	0.51	0.716
2-Way Interactions	3	0.00000868	0.00000868	0.00000289	2.16	0.332
3-Way Interactions	1	0.00001088	0.00001088	0.00001088	8.13	0.104
Curvature	1	0.00000017	0.00000017	0.00000017	0.12	0.758
Residual Error	2	0.00000268	0.00000268	0.00000134		
Pure Error	2	0.00000268	0.00000268	0.00000134		
Total	10	0.00002444				

Observations for CRACK DE

Obs	CRACK DE	Fit	SE Fit	Residual	St Resid
1	0.009950	0.009950	0.001157	-0.000000	* X
2	0.004260	0.004260	0.001157	0.000000	* X
3	0.005940	0.005940	0.001157	-0.000000	* X
4	0.008790	0.008790	0.001157	0.000000	* X
5	0.007160	0.007160	0.001157	-0.000000	* X
6	0.007580	0.007580	0.001157	0.000000	* X
7	0.008320	0.008320	0.001157	-0.000000	* X
8	0.007950	0.007950	0.001157	-0.000000	* X
9	0.006650	0.007770	0.000668	-0.001120	-1.19
10	0.008960	0.007770	0.000668	0.001190	1.26
11	0.007700	0.007770	0.000668	-0.000070	-0.07

X denotes an observation whose X value gives it large influence.

Estimated Coefficients for CRACK using data in uncoded units

Term	Coef
Constant	0.0508267
CAPACITA	-0.00124633
VOLTAGE	-0.000267883
CURRENT	-0.00912667
CAPACITA*VOLTAGE	7.511667E-06
CAPACITA*CURRENT	0.000257333
VOLTAGE*CURRENT	0.0000569500
CAPACITA*VOLTAGE*CURRENT	-1.55500E-06
Ct Pt	0.000276250

Least Squares Means for CRACK DE

			Mean	SE Mean
CAPACITA				
20			0.007842	0.000578
50			0.007145	0.000578
VOLTAGE				
100			0.007238	0.000578
200			0.007750	0.000578
CURRENT				
3			0.007235	0.000578
5			0.007753	0.000578
CAPACITA*VOLTAGE				
20	100		0.008555	0.000818
50	100		0.005920	0.000818
20	200		0.007130	0.000818
50	200		0.008370	0.000818
CAPACITA*CURRENT				
20	3		0.007945	0.000818
50	3		0.006525	0.000818
20	5		0.007740	0.000818
50	5		0.007765	0.000818
VOLTAGE*CURRENT				
100	3		0.007105	0.000818
200	3		0.007365	0.000818
100	5		0.007370	0.000818
200	5		0.008135	0.000818
CAPACITA*VOLTAGE*CURRENT				
20	100	3	0.009950	0.001157
50	100	3	0.004260	0.001157
20	200	3	0.005940	0.001157
50	200	3	0.008790	0.001157
20	100	5	0.007160	0.001157
50	100	5	0.007580	0.001157
20	200	5	0.008320	0.001157
50	200	5	0.007950	0.001157

Mean for Center Point = 0.007770

Alias Structure

I
CAPACITA
VOLTAGE
CURRENT
CAPACITA*VOLTAGE
CAPACITA*CURRENT

VOLTAGE*CURRENT
CAPACITA*VOLTAGE*CURRENT

REDUCED MODEL

Fractional Factorial Fit: DEPOSITION RATE versus VOLTAGE, CURRENT

Estimated Effects and Coefficients for DEPOSITI (coded units)

Term	Effect	Coef	SE Coef	T	P
Constant		0.2394	0.02690	8.90	0.000
VOLTAGE	0.2199	0.1100	0.03155	3.49	0.008
CURRENT	0.2160	0.1080	0.03155	3.42	0.009

Analysis of Variance for DEPOSITI (coded units)

Source	DF	Seq SS	Adj SS	Adj MS	F	P
Main Effects	2	0.190068	0.190068	0.095034	11.94	0.004
Residual Error	8	0.063699	0.063699	0.007962		
Curvature	1	0.007509	0.007509	0.007509	0.94	0.366
Lack of Fit	1	0.001109	0.001109	0.001109	0.12	0.740
Pure Error	6	0.055080	0.055080	0.009180		
Total	10	0.253767				

Observations for DEPOSITI

Obs	DEPOSITI	Fit	SE Fit	Residual	St Resid
1	0.006300	0.021425	0.052100	-0.015125	-0.21
2	0.045000	0.021425	0.052100	0.023575	0.33
3	0.145200	0.241375	0.052100	-0.096175	-1.33
4	0.393100	0.241375	0.052100	0.151725	2.09R
5	0.260500	0.237425	0.052100	0.023075	0.32
6	0.269900	0.237425	0.052100	0.032475	0.45
7	0.496500	0.457375	0.052100	0.039125	0.54
8	0.426700	0.457375	0.052100	-0.030675	-0.42
9	0.194300	0.239400	0.026904	-0.045100	-0.53
10	0.300700	0.239400	0.026904	0.061300	0.72
11	0.095200	0.239400	0.026904	-0.144200	-1.69

R denotes an observation with a large standardized residual

Estimated Coefficients for DEPOSITI using data in uncoded units

Term	Coef
Constant	-0.522525
VOLTAGE	0.00219950
CURRENT	0.108000

Least Squares Means for DEPOSITI

	Mean	SE Mean
VOLTAGE		
100	0.1294	0.04146
200	0.3494	0.04146
CURRENT		
3	0.1314	0.04146
5	0.3474	0.04146

Mean for Center Point = 0.1967

Alias Structure

I
VOLTAGE
CURRENT

NIMONIC 105

Fractional Factorial Fit: DEPOSITION RATE, VOID CONTENT, CRACK DENSITY

Fractional Factorial Fit: DEPOSITION RATE versus CAPACITANCE, VOLTAGE, CURRENT

Estimated Effects and Coefficients for DEPOSITI (coded units)

Term	Effect	Coef	SE Coef	T	P
Constant		0.252125	0.03110	8.11	0.015
CAPACITA	0.075050	0.037525	0.03110	1.21	0.351
VOLTAGE	0.207250	0.103625	0.03110	3.33	0.079
CURRENT	0.164900	0.082450	0.03110	2.65	0.118
CAPACITA*VOLTAGE	0.011850	0.005925	0.03110	0.19	0.866
CAPACITA*CURRENT	0.031700	0.015850	0.03110	0.51	0.661
VOLTAGE*CURRENT	0.044300	0.022150	0.03110	0.71	0.550
CAPACITA*VOLTAGE*CURRENT	0.014900	0.007450	0.03110	0.24	0.833
Ct Pt		0.097475	0.05954	1.64	0.243

Analysis of Variance for DEPOSITI (coded units)

Source	DF	Seq SS	Adj SS	Adj MS	F	P
Main Effects	3	0.151554	0.151554	0.0505180	6.53	0.136
2-Way Interactions	3	0.006216	0.006216	0.0020719	0.27	0.847
3-Way Interactions	1	0.000444	0.000444	0.0004440	0.06	0.833
Curvature	1	0.020730	0.020730	0.0207303	2.68	0.243
Residual Error	2	0.015470	0.015470	0.0077352		
Pure Error	2	0.015470	0.015470	0.0077352		
Total	10	0.194414				

Observations for DEPOSITI

Obs	DEPOSITI	Fit	SE Fit	Residual	St Resid
1	0.065000	0.065000	0.087950	0.000000	* X
2	0.111400	0.111400	0.087950	0.000000	* X
3	0.231000	0.231000	0.087950	0.000000	* X
4	0.271300	0.271300	0.087950	0.000000	* X
5	0.168800	0.168800	0.087950	0.000000	* X
6	0.248800	0.248800	0.087950	-0.000000	* X
7	0.393600	0.393600	0.087950	0.000000	* X
8	0.527100	0.527100	0.087950	0.000000	* X
9	0.249100	0.349600	0.050778	-0.100500	-1.40
10	0.412500	0.349600	0.050778	0.062900	0.88
11	0.387200	0.349600	0.050778	0.037600	0.52

X denotes an observation whose X value gives it large influence.

Estimated Coefficients for DEPOSITI using data in uncoded units

Term	Coef
Constant	-0.22950
CAPACITA	0.0030500
VOLTAGE	0.00141467
CURRENT	0.031167
CAPACITA*VOLTAGE	-0.000031833
CAPACITA*CURRENT	-0.00043333
VOLTAGE*CURRENT	0.00009533
CAPACITA*VOLTAGE*CURRENT	0.0000099333

Ct Pt 0.0974750

Least Squares Means for DEPOSITI

			Mean	SE Mean
CAPACITA				
20			0.21460	0.04398
50			0.28965	0.04398
VOLTAGE				
100			0.14850	0.04398
200			0.35575	0.04398
CURRENT				
3			0.16967	0.04398
5			0.33458	0.04398
CAPACITA*VOLTAGE				
20	100		0.11690	0.06219
50	100		0.18010	0.06219
20	200		0.31230	0.06219
50	200		0.39920	0.06219
CAPACITA*CURRENT				
20	3		0.14800	0.06219
50	3		0.19135	0.06219
20	5		0.28120	0.06219
50	5		0.38795	0.06219
VOLTAGE*CURRENT				
100	3		0.08820	0.06219
200	3		0.25115	0.06219
100	5		0.20880	0.06219
200	5		0.46035	0.06219
CAPACITA*VOLTAGE*CURRENT				
20	100	3	0.06500	0.08795
50	100	3	0.11140	0.08795
20	200	3	0.23100	0.08795
50	200	3	0.27130	0.08795
20	100	5	0.16880	0.08795
50	100	5	0.24880	0.08795
20	200	5	0.39360	0.08795
50	200	5	0.52710	0.08795

Mean for Center Point = 0.34960

Fractional Factorial Fit: VOID CONTENT versus CAPACITANCE, VOLTAGE, CURRENT

Estimated Effects and Coefficients for VOID (coded units)

Term	Effect	Coef	SE Coef	T	P
Constant		2.12500	0.1472	14.44	0.005
CAPACITA	0.45000	0.22500	0.1472	1.53	0.266
VOLTAGE	1.15000	0.57500	0.1472	3.91	0.060
CURRENT	0.80000	0.40000	0.1472	2.72	0.113
CAPACITA*VOLTAGE	0.15000	0.07500	0.1472	0.51	0.661
CAPACITA*CURRENT	0.50000	0.25000	0.1472	1.70	0.232
VOLTAGE*CURRENT	1.00000	0.50000	0.1472	3.40	0.077
CAPACITA*VOLTAGE*CURRENT	0.50000	0.25000	0.1472	1.70	0.232
Ct Pt		0.70833	0.2819	2.51	0.129

Analysis of Variance for VOID (coded units)

Source	DF	Seq SS	Adj SS	Adj MS	F	P

Main Effects	3	4.33000	4.33000	1.4433	8.33	0.109
2-Way Interactions	3	2.54500	2.54500	0.8483	4.89	0.174
3-Way Interactions	1	0.50000	0.50000	0.5000	2.88	0.232
Curvature	1	1.09470	1.09470	1.0947	6.32	0.129
Residual Error	2	0.34667	0.34667	0.1733		
Pure Error	2	0.34667	0.34667	0.1733		
Total	10	8.81636				

Observations for VOID CON

Obs	VOID CON	Fit	SE Fit	Residual	St Resid
1	1.50000	1.50000	0.41633	0.00000	* X
2	1.80000	1.80000	0.41633	-0.00000	* X
3	2.00000	2.00000	0.41633	0.00000	* X
4	1.60000	1.60000	0.41633	0.00000	* X
5	1.30000	1.30000	0.41633	0.00000	* X
6	1.60000	1.60000	0.41633	-0.00000	* X
7	2.80000	2.80000	0.41633	0.00000	* X
8	4.40000	4.40000	0.41633	0.00000	* X
9	2.50000	2.83333	0.24037	-0.33333	-0.98
10	3.30000	2.83333	0.24037	0.46667	1.37
11	2.70000	2.83333	0.24037	-0.13333	-0.39

X denotes an observation whose X value gives it large influence.

Estimated Coefficients for VOID using data in uncoded units

Term	Coef
Constant	0.13333
CAPACITA	0.133333
VOLTAGE	0.0146667
CURRENT	0.06667
CAPACITA*VOLTAGE	-0.00123333
CAPACITA*CURRENT	-0.0333333
VOLTAGE*CURRENT	-0.00166667
CAPACITA*VOLTAGE*CURRENT	0.000333333
Ct Pt	0.708333

Least Squares Means for VOID CON

		Mean	SE Mean
CAPACITA			
20		1.900	0.2082
50		2.350	0.2082
VOLTAGE			
100		1.550	0.2082
200		2.700	0.2082
CURRENT			
3		1.725	0.2082
5		2.525	0.2082
CAPACITA*VOLTAGE			
20	100	1.400	0.2944
50	100	1.700	0.2944
20	200	2.400	0.2944
50	200	3.000	0.2944
CAPACITA*CURRENT			
20	3	1.750	0.2944
50	3	1.700	0.2944
20	5	2.050	0.2944
50	5	3.000	0.2944
VOLTAGE*CURRENT			

100	3		1.650	0.2944
200	3		1.800	0.2944
100	5		1.450	0.2944
200	5		3.600	0.2944

CAPACITA*VOLTAGE*CURRENT

20	100	3	1.500	0.4163
50	100	3	1.800	0.4163
20	200	3	2.000	0.4163
50	200	3	1.600	0.4163
20	100	5	1.300	0.4163
50	100	5	1.600	0.4163
20	200	5	2.800	0.4163
50	200	5	4.400	0.4163

Mean for Center Point = 2.833

Fractional Factorial Fit: CRACK DENSITY versus CAPACITANCE, VOLTAGE, CURRENT

Estimated Effects and Coefficients for CRACK (coded units)

Term	Effect	Coef	SE Coef	T	P
Constant		0.005641	0.000169	33.35	0.001
CAPACITA	0.000162	0.000081	0.000169	0.48	0.678
VOLTAGE	0.003132	0.001566	0.000169	9.26	0.011
CURRENT	0.001508	0.000754	0.000169	4.46	0.047
CAPACITA*VOLTAGE	-0.000747	-0.000374	0.000169	-2.21	0.158
CAPACITA*CURRENT	0.000938	0.000469	0.000169	2.77	0.109
VOLTAGE*CURRENT	0.001457	0.000729	0.000169	4.31	0.050
CAPACITA*VOLTAGE*CURRENT	0.000088	0.000044	0.000169	0.26	0.820
Ct Pt		0.001569	0.000324	4.84	0.040

Analysis of Variance for CRACK (coded units)

Source	DF	Seq SS	Adj SS	Adj MS	F	P
Main Effects	3	0.00002422	0.00002422	0.00000807	35.27	0.028
2-Way Interactions	3	0.00000712	0.00000712	0.00000237	10.37	0.089
3-Way Interactions	1	0.00000002	0.00000002	0.00000002	0.07	0.820
Curvature	1	0.00000537	0.00000537	0.00000537	23.46	0.040
Residual Error	2	0.00000046	0.00000046	0.00000023		
Pure Error	2	0.00000046	0.00000046	0.00000023		
Total	10	0.00003719				

Observations for CRACK DE

Obs	CRACK DE	Fit	SE Fit	Residual	St Resid	
1	0.004020	0.004020	0.000478	0.000000	*	X
2	0.004080	0.004080	0.000478	0.000000	*	X
3	0.006530	0.006530	0.000478	0.000000	*	X
4	0.004920	0.004920	0.000478	0.000000	*	X
5	0.003220	0.003220	0.000478	0.000000	*	X
6	0.004980	0.004980	0.000478	-0.000000	*	X
7	0.008470	0.008470	0.000478	0.000000	*	X
8	0.008910	0.008910	0.000478	0.000000	*	X
9	0.006680	0.007210	0.000276	-0.000530	-1.36	
10	0.007610	0.007210	0.000276	0.000400	1.02	
11	0.007340	0.007210	0.000276	0.000130	0.33	

X denotes an observation whose X value gives it large influence.

Estimated Coefficients for CRACK using data in uncoded units

Term	Coef
Constant	0.00701667
CAPACITA	-0.000009833
VOLTAGE	-1.36667E-06
CURRENT	-0.00222000
CAPACITA*VOLTAGE	-7.31667E-07
CAPACITA*CURRENT	0.0000225000
VOLTAGE*CURRENT	0.0000125333
CAPACITA*VOLTAGE*CURRENT	5.833333E-08
Ct Pt	0.00156875

Least Squares Means for CRACK DE

			Mean	SE Mean
CAPACITA				
20			0.005560	0.000239
50			0.005722	0.000239
VOLTAGE				
100			0.004075	0.000239
200			0.007207	0.000239
CURRENT				
3			0.004887	0.000239
5			0.006395	0.000239
CAPACITA*VOLTAGE				
20	100		0.003620	0.000338
50	100		0.004530	0.000338
20	200		0.007500	0.000338
50	200		0.006915	0.000338
CAPACITA*CURRENT				
20	3		0.005275	0.000338
50	3		0.004500	0.000338
20	5		0.005845	0.000338
50	5		0.006945	0.000338
VOLTAGE*CURRENT				
100	3		0.004050	0.000338
200	3		0.005725	0.000338
100	5		0.004100	0.000338
200	5		0.008690	0.000338
CAPACITA*VOLTAGE*CURRENT				
20	100	3	0.004020	0.000478
50	100	3	0.004080	0.000478
20	200	3	0.006530	0.000478
50	200	3	0.004920	0.000478
20	100	5	0.003220	0.000478
50	100	5	0.004980	0.000478
20	200	5	0.008470	0.000478
50	200	5	0.008910	0.000478

Mean for Center Point = 0.007210

Alias Structure

I
CAPACITA
VOLTAGE
CURRENT
CAPACITA*VOLTAGE
CAPACITA*CURRENT
VOLTAGE*CURRENT

CAPACITA*VOLTAGE*CURRENT

REDUCED MODELS

Fractional Factorial Fit: DEPOSITION RATE versus VOLTAGE

Estimated Effects and Coefficients for DEPOSITI (coded units)

Term	Effect	Coef	SE Coef	T	P
Constant		0.2787	0.03311	8.42	0.000
VOLTAGE	0.2072	0.1036	0.03882	2.67	0.026

Analysis of Variance for DEPOSITI (coded units)

Source	DF	Seq SS	Adj SS	Adj MS	F	P
Main Effects	1	0.085905	0.085905	0.08591	7.13	0.026
Residual Error	9	0.108509	0.108509	0.01206		
Curvature	1	0.020730	0.020730	0.02073	1.89	0.207
Pure Error	8	0.087779	0.087779	0.01097		
Total	10	0.194414				

Observations for DEPOSITI

Obs	DEPOSITI	Fit	SE Fit	Residual	St Resid
1	0.065000	0.175084	0.051021	-0.110084	-1.13
2	0.111400	0.175084	0.051021	-0.063684	-0.65
3	0.231000	0.382334	0.051021	-0.151334	-1.56
4	0.271300	0.382334	0.051021	-0.111034	-1.14
5	0.168800	0.175084	0.051021	-0.006284	-0.06
6	0.248800	0.175084	0.051021	0.073716	0.76
7	0.393600	0.382334	0.051021	0.011266	0.12
8	0.527100	0.382334	0.051021	0.144766	1.49
9	0.249100	0.278709	0.033107	-0.029609	-0.28
10	0.412500	0.278709	0.033107	0.133791	1.28
11	0.387200	0.278709	0.033107	0.108491	1.04

Estimated Coefficients for DEPOSITI using data in uncoded units

Term	Coef
Constant	-0.032166
VOLTAGE	0.00207250

Least Squares Means for DEPOSITI

	Mean	SE Mean
VOLTAGE		
100	0.1751	0.05102
200	0.3823	0.05102

Mean for Center Point = 0.3496

Alias Structure

I
VOLTAGE

Fractional Factorial Fit: VOID CONTENT versus VOLTAGE

Estimated Effects and Coefficients for VOID (coded units)

Term	Effect	Coef	SE Coef	T	P
Constant		2.3182	0.2497	9.28	0.000
VOLTAGE	1.1500	0.5750	0.2928	1.96	0.081

Analysis of Variance for VOID (coded units)

Source	DF	Seq SS	Adj SS	Adj MS	F	P
Main Effects	1	2.645	2.645	2.6450	3.86	0.081
Residual Error	9	6.171	6.171	0.6857		
Curvature	1	1.095	1.095	1.0947	1.73	0.225
Pure Error	8	5.077	5.077	0.6346		
Total	10	8.816				

Observations for VOID CON

Obs	VOID CON	Fit	SE Fit	Residual	St Resid
1	1.50000	1.74318	0.38477	-0.24318	-0.33
2	1.80000	1.74318	0.38477	0.05682	0.08
3	2.00000	2.89318	0.38477	-0.89318	-1.22
4	1.60000	2.89318	0.38477	-1.29318	-1.76
5	1.30000	1.74318	0.38477	-0.44318	-0.60
6	1.60000	1.74318	0.38477	-0.14318	-0.20
7	2.80000	2.89318	0.38477	-0.09318	-0.13
8	4.40000	2.89318	0.38477	1.50682	2.05R
9	2.50000	2.31818	0.24967	0.18182	0.23
10	3.30000	2.31818	0.24967	0.98182	1.24
11	2.70000	2.31818	0.24967	0.38182	0.48

R denotes an observation with a large standardized residual

Estimated Coefficients for VOID using data in uncoded units

Term	Coef
Constant	0.593182
VOLTAGE	0.0115000

Least Squares Means for VOID CON

	Mean	SE Mean
VOLTAGE		
100	1.743	0.3848
200	2.893	0.3848

Mean for Center Point = 2.833

Alias Structure

I
VOLTAGE

APPENDIX G – ELEMENTAL MAP AND LINE SCANS

INCONEL 738 - UNCOATED

1/29/05 9:11:55 AM

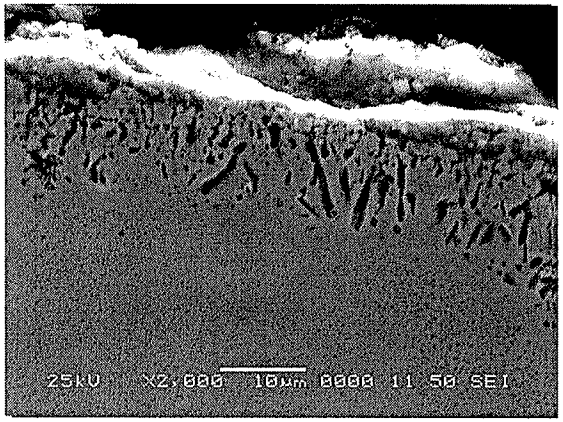

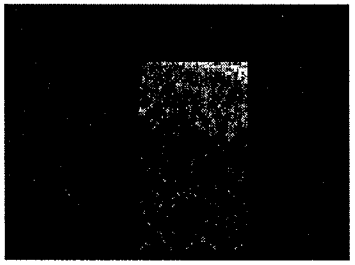
Oxygen Ka1_2


Aluminum Ka1

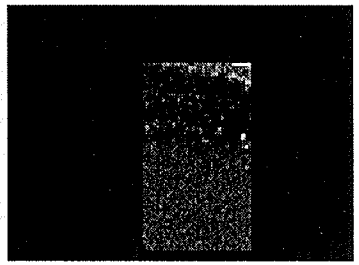
Titanium Ka1

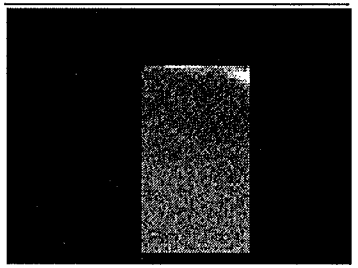
Chromium Ka1

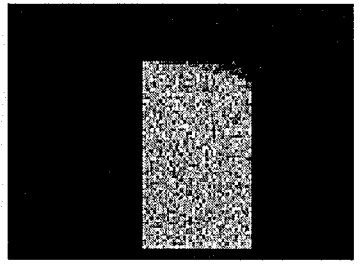
Cobalt Ka1

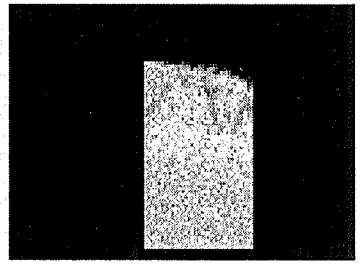
Nickel Ka1

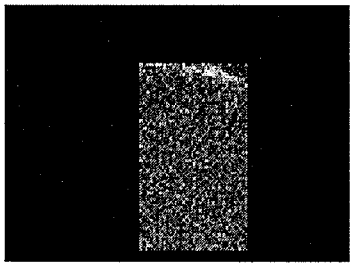
Tungsten Ma1

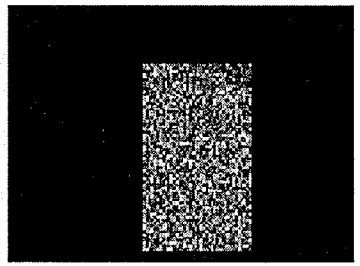
Iron Ka1

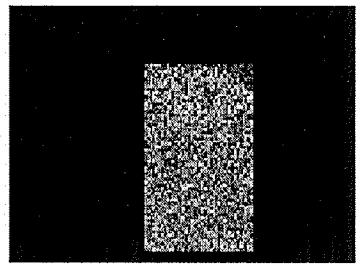
Molybdenum La1

NOTES:
IN738 BARE
2000X
120 SEC

INCONEL 738 MICRO-WELD COATING

2/23/05 10:23:17 PM

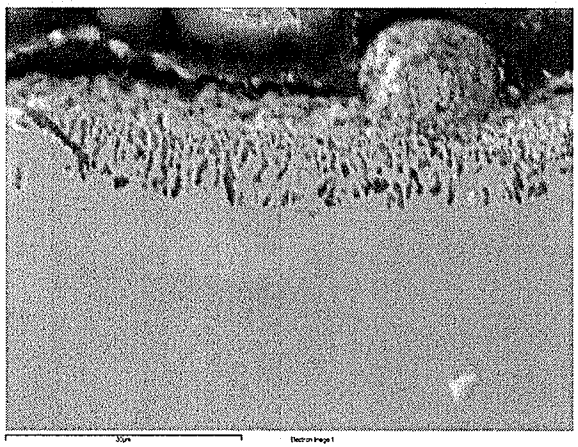

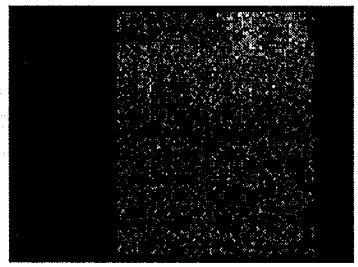

Oxygen Ka1_2

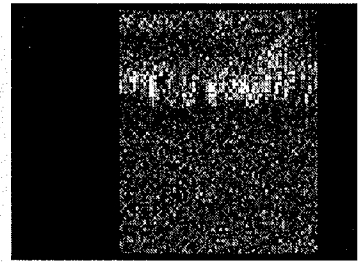

Aluminum Ka1

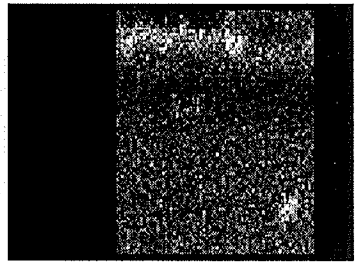

Titanium Ka1

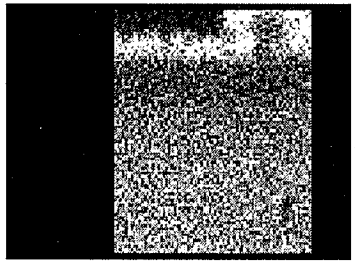

Chromium Ka1

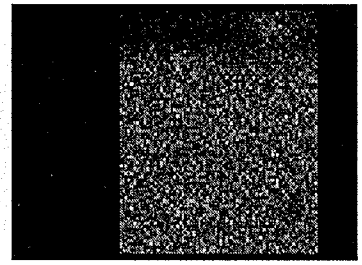

Cobalt Ka1

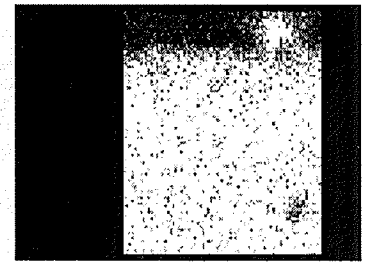

Nickel Ka1

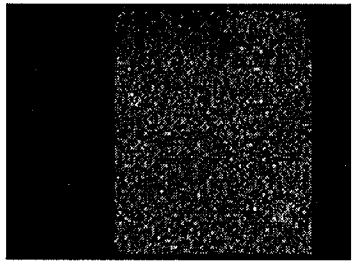

Molybdenum La1

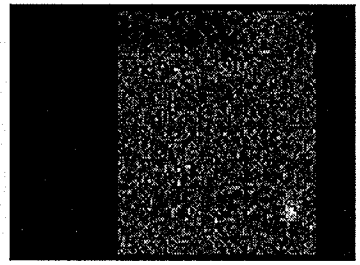

Tungsten Ma1

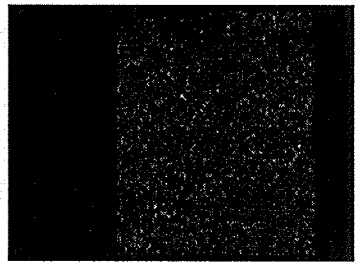

Iron Ka1

NOTES:
IN738
2000X
240 SEC

INCONEL 722 MICRO-WELD COATING

2/23/05 9:28:27 PM

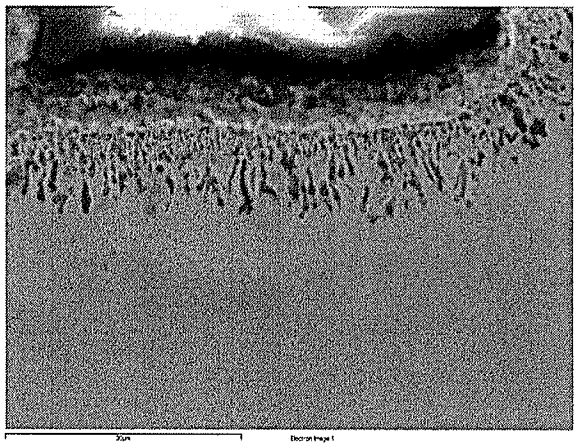

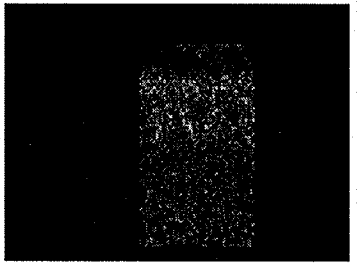

Oxygen Ka1_2

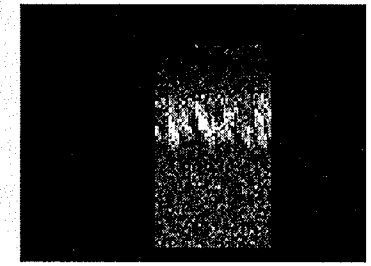

Aluminum Ka1

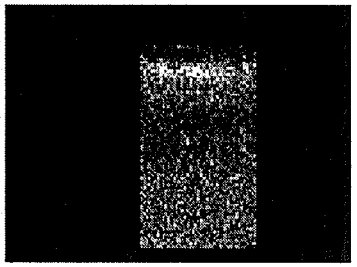

Titanium Ka1

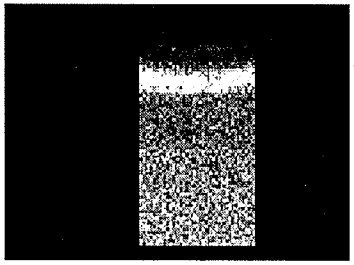

Chromium Ka1

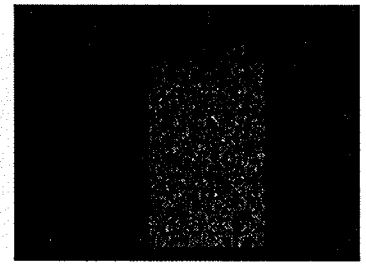

Iron Ka1

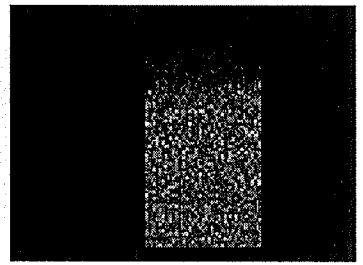

Cobalt Ka1

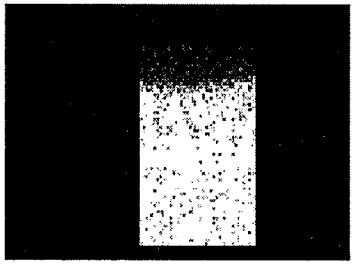

Nickel Ka1

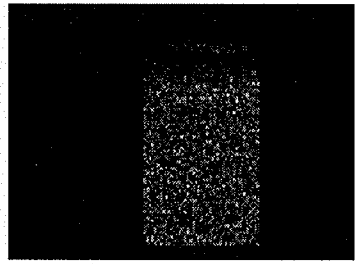

Tungsten Ma1

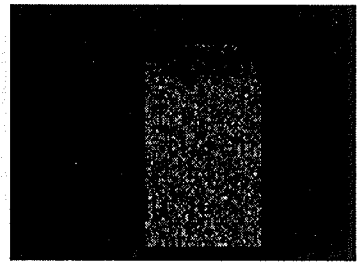

Molybdenum La1

NOTES:
IN722
2000X
120 SEC

INCONEL 718 MICRO-WELD COATING

2/23/05 7:42:10 PM

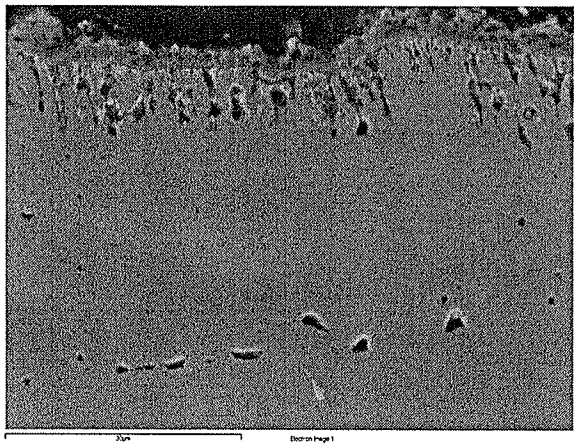

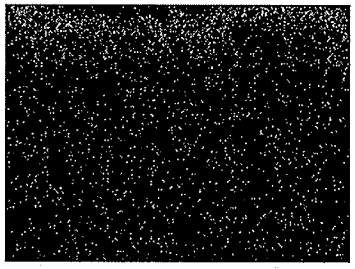

Oxygen Ka1_2

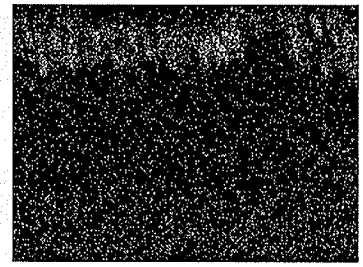

Aluminum Ka1

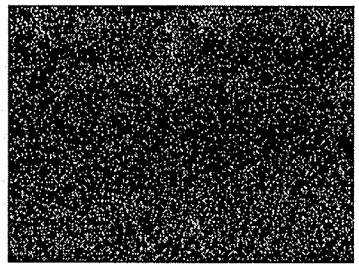

Titanium Ka1

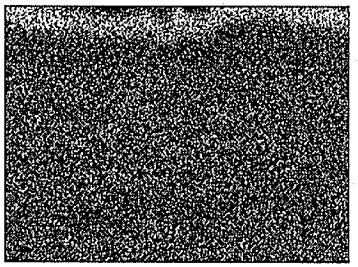

Chromium Ka1

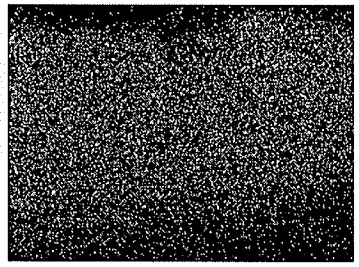

Iron Ka1

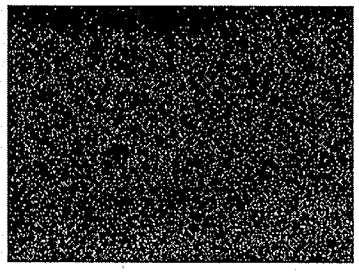

Cobalt Ka1

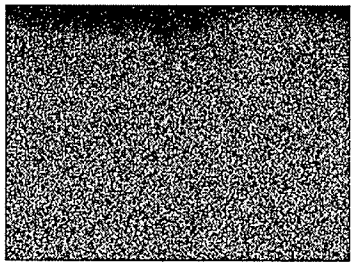

Nickel Ka1

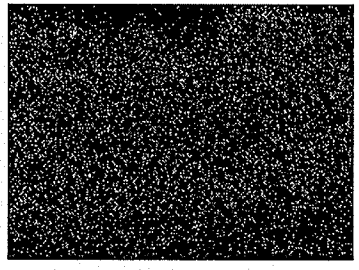

Niobium La1

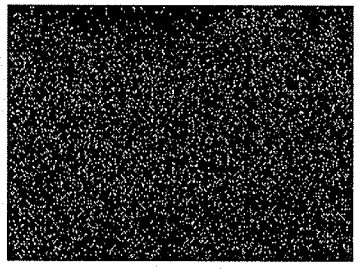

Molybdenum La1

NOTES:
IN718
2000X
120 SEC

NIMONIC 105 MICRO-WELD COATING

2/23/05 8:47:14 PM

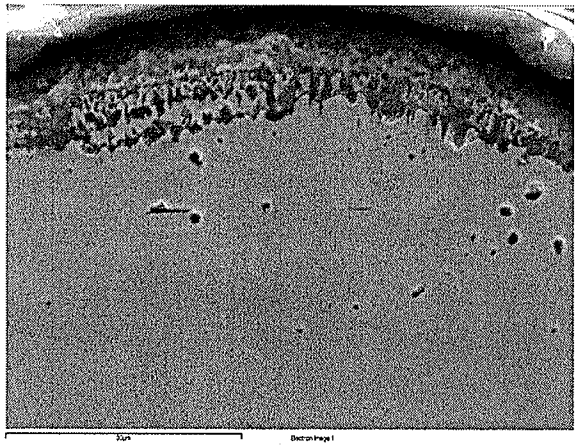

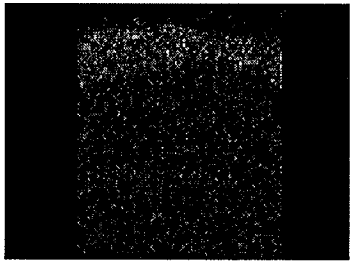

Oxygen Ka1_2

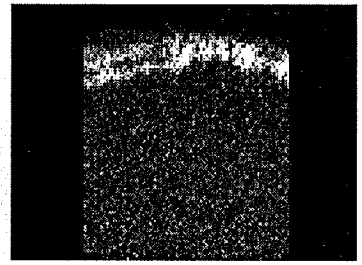

Aluminum Ka1

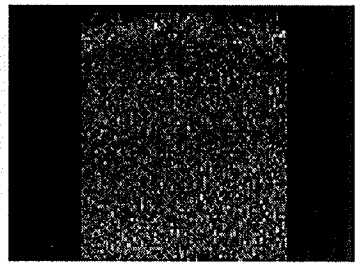

Titanium Ka1

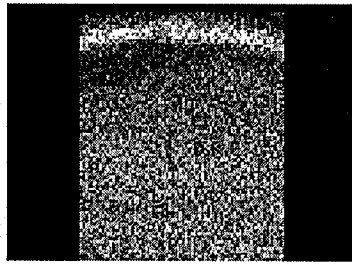

Chromium Ka1

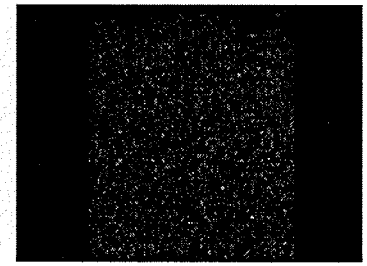

Iron Ka1

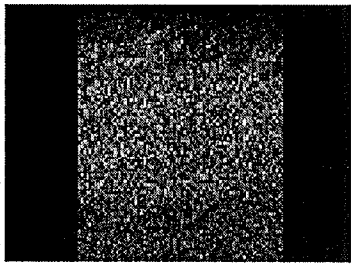

Cobalt Ka1

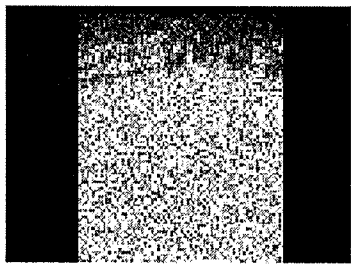

Nickel Ka1

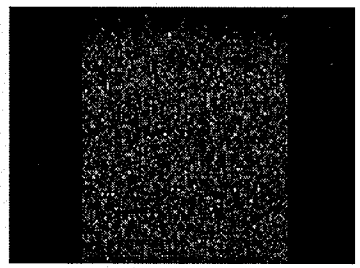

Molybdenum La1

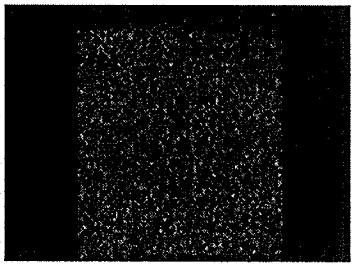

Tungsten Ma1

Comment:
N105
2000X
150 SEC

INCONEL 738 - UNCOATED

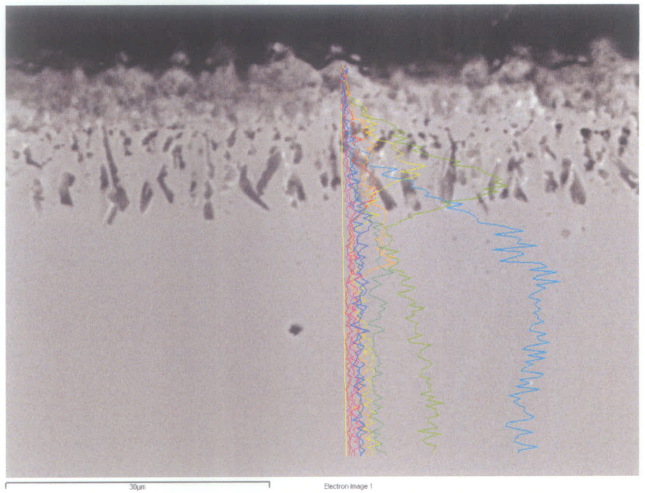

NOTES:
IN738BARE
2000X
180 SEC

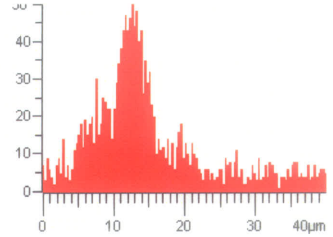

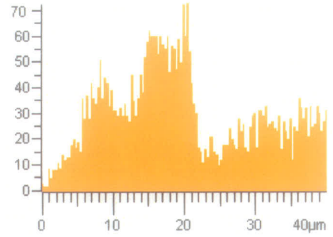

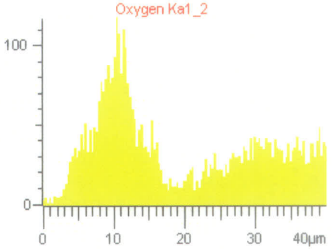

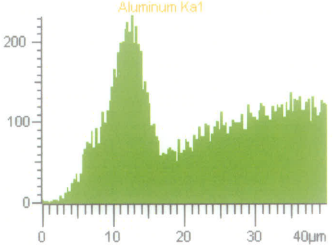

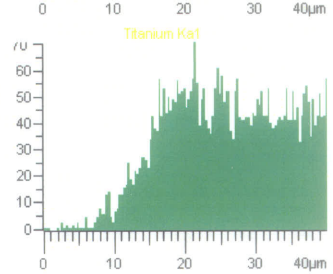

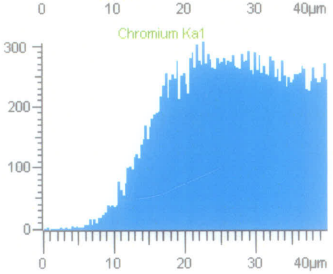

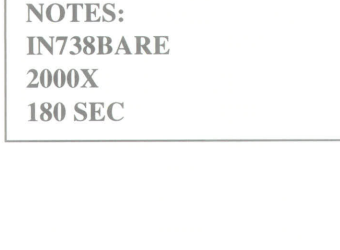

INCONEL 738 MICRO-WELD COATING

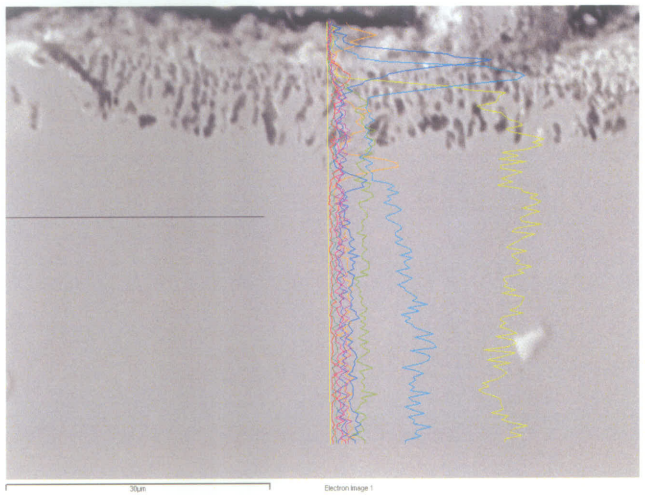

NOTES:
IN738
2000X
240 SEC

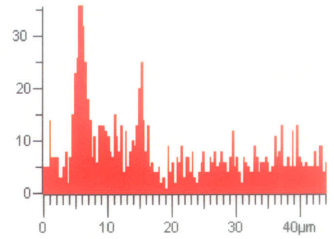

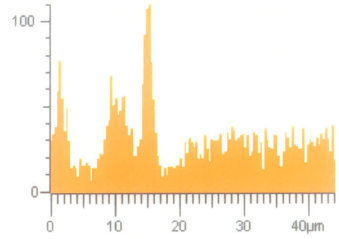

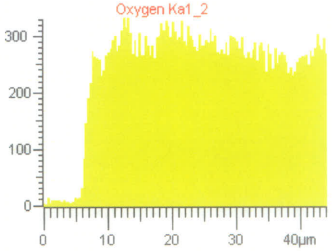

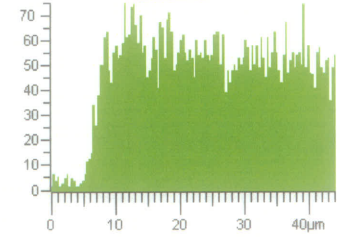

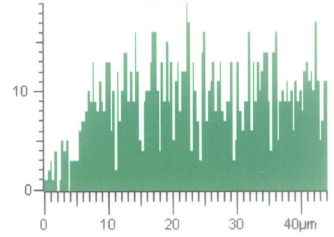

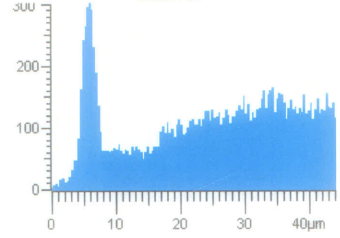

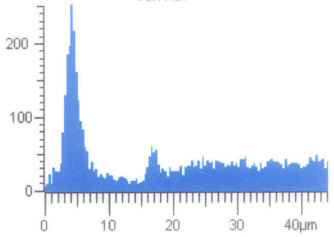

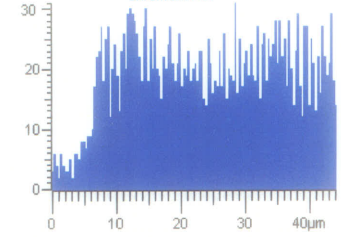

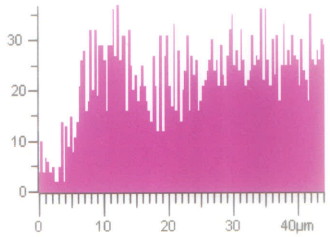

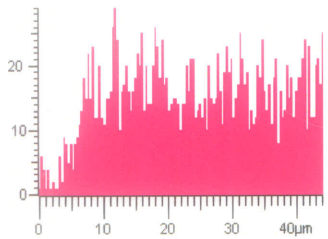

INCONEL 722 MICRO-WELD COATING

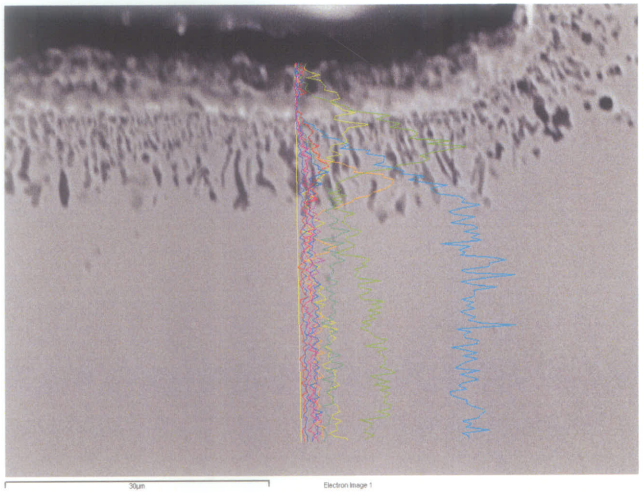

NOTES:
IN722
2000X
120 SEC

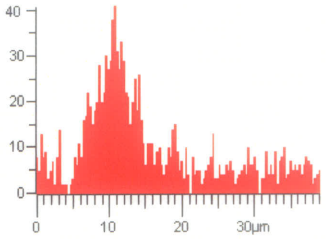

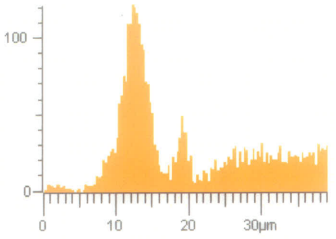

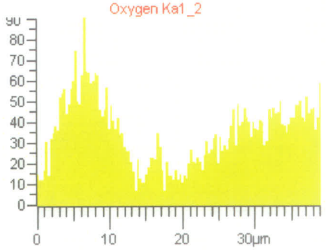

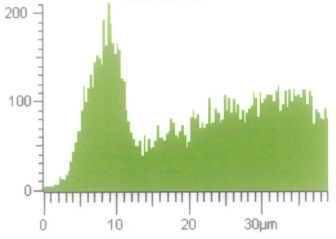

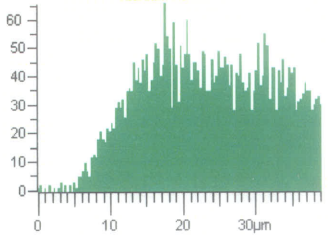

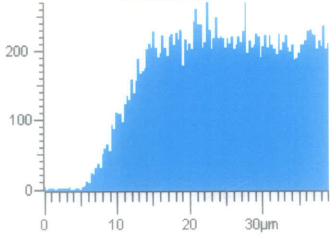

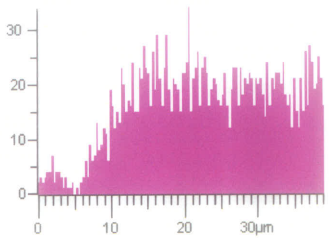

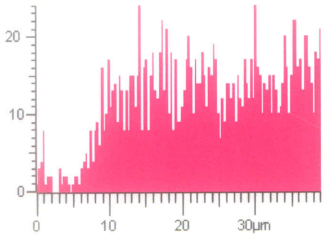

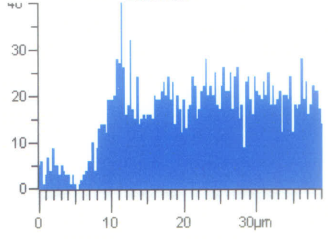

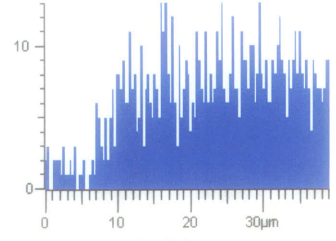

INCONEL 718 MICRO-WELD COATING

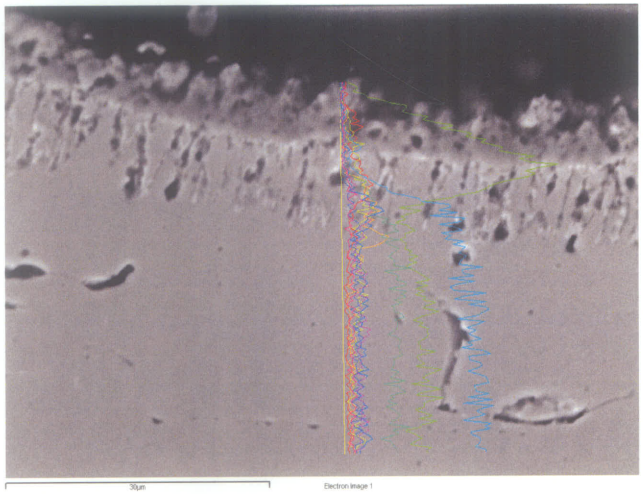

NOTES:
IN718
2000X
120 SEC

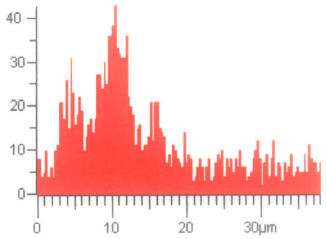

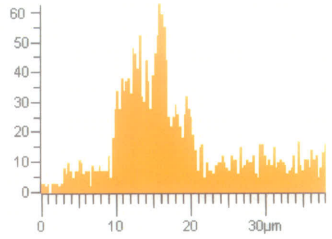

Oxygen Ka1_2

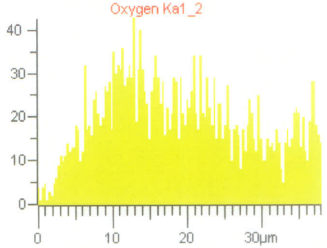

Aluminum Ka1

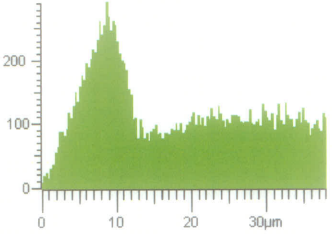

Titanium Ka1

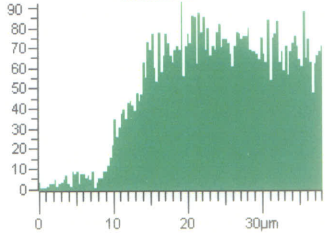

Chromium Ka1

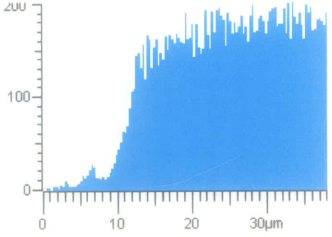

Iron Ka1

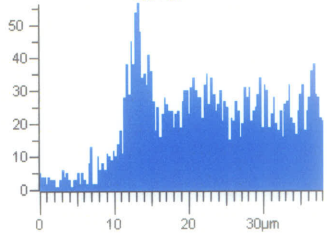

Nickel Ka1

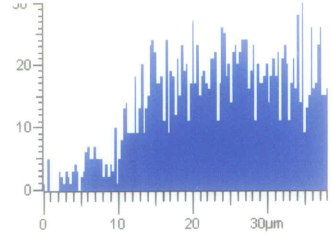

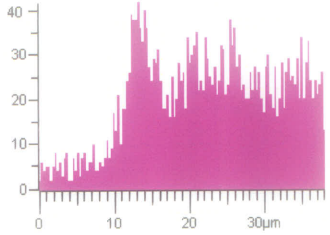

Molybdenum La1

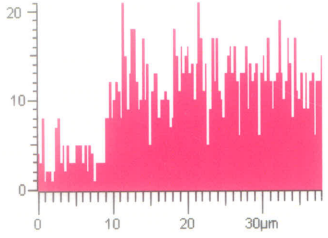

Tungsten Ma1

Niobium La1

Cobalt Ka1

NIMONIC 105 – MICRO-WELD COATING

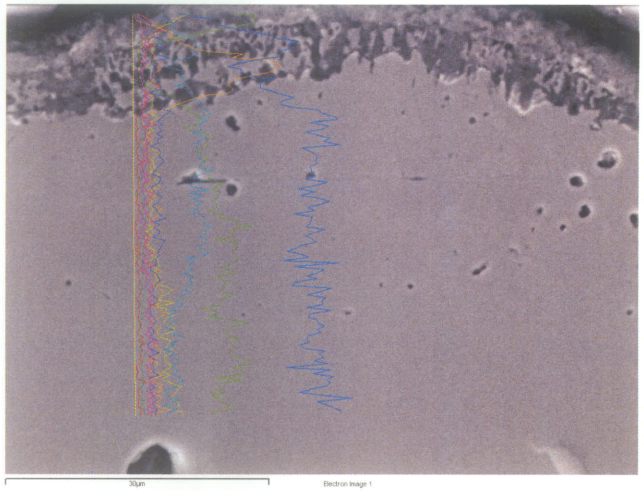

Comment:
N105
2000X
180 SEC